Spatial Model Reduction for Transport Phenomena in Environmental and Agricultural Engineering

Martijn Halbo Dirkse

Spatial Model Reduction for Transport Phenomena in Environmental and Agricultural Engineering

Martijn Halbo Dirkse

Abstract

The performance of many environmental and agricultural systems depends on heat and mass transfer that can be modelled in various ways. The model can subsequently be used for optimal system design and, therefore, it provides a powerful tool for system analysis. However, complexity of these models in distributed systems can be a bottleneck for application. In this thesis the focus was on simplification of modelling approaches. This was demonstrated in two case studies that originate from environmental and agricultural engineering.

Computational fluid dynamics (CFD) modelling was simplified based on 'a priori' physical analysis. The number of mesh cells could be strongly reduced resulting in a relatively efficient model. The model was verified on a natural convection driven heat exchanger, resulting in recommendations to improve the efficiency. With the CFD results as reference, a simple lumped engineering model could be developed for a given geometry that constituted only two algebraic equations.

To include the impact of the geometry in a relatively fast method, potential flow theory has been studied thoroughly. The method is based on transforming polygonal regions to infinite straight channels. The theory was applied successfully to predict the velocity field in a thin area between two membranes, providing design recommendations for reverse electrodialysis systems. Potential flow modelling was also used to approximate the residence time distribution as a tool to analyse spatially distributed chemical reactions.

Potential flow theory only applies to creeping flows. Therefore it was extended to general two-dimensional flows by modelling the main flow area by transformation to a straight channel, and a recirculation area by transformation to a disc. The model has geometric parameters that define the separation line between the main flow area and the recirculation wakes, and for known parameter values the velocity field can be calculated with an average error of 20% - 30% for a wide range of two-dimensional flows. Since the heat flux can be calculated for different geometries, the Extended Potential Flow Model is applicable for design purposes. In summary the extended potential flow theory provides a powerful analysis tool for the applied engineer that will assist him/her with the design and analysis of distributed systems.

Contents

Chapter 1

General Introduction

Notation

a	Prevertex
a_T	Turbulent thermal diffusivity, m^{2}s^{-1}
c	Heat capacity, J kg^{-1} K^{-1}
$\vec{f_g}$	Acceleration due to gravity, ms^{-2}
g	Function
i	Imaginary unit
k	Turbulent kinetic energy per unit mass, m^{2}s^{-2}
n	Number of corners
p	Pressure, Pa
t	Time, s
$\vec{u}$	Velocity vector, ms^{-1}
$\vec{x}$	Space vector, m
z	Complex coordinate on polygonal domain
K	Constant in Schwarz-Christoffel theorem
N	Number of algebraic equations
O	Landau order symbol
$\mathbf{S}$	Strain rate tensor, s^{-1}
T	Temperature, K

Greek symbols

α	Internal angle of corner, rad
δ	Boundary layer thickness, m
ϵ	Dissipation of turbulent kinetic energy, m^{2}s^{-3}
ζ	Complex coordinate on upper half plane
λ	Thermal conductivity, W m^{-1} K^{-1}
ν	Kinematic viscosity, m^{2}s^{-1}
ν_T	Kinetic eddy viscosity, m^{2}s^{-1}
ξ	Similarity variable
ρ	Density, kg m^{-3}
σ	Dimensionless closure parameter of k-ω turbulence model
ϕ	Potential function, m^{2}s^{-1}
ψ	Stream function, m^{2}s^{-1}
ω	Specific dissipation of turbulent kinetic energy, s^{-1}
Δt	Time step, s
$\mathbf{\Theta}$	Specific Reynolds stress tensor (m^{2}s^{-2})

1.1 Introduction

In many environmental and agricultural systems, processes of heat and mass transfer play an important role. These processes are influenced by spatial variation of temperature, species concentrations or pressure. These variations can be influenced through the design and control of the system. Therefore, careful system design and system control are required to optimize the system performance. The impact of possible system designs and control strategies can be predicted by the development of a mathematical model, which analyses spatial variations of the flow variables and the resulting heat and mass fluxes. Engineers can use the model to compare many possible design and control scenarios, allowing an optimal design and operation. The present thesis focusses on modelling methods for spatial variation, and on their application to the design and control of environmental and agricultural systems.

Typical examples of environmental and agricultural systems are drying facilities (Gigler, 2000; Hosseini, 2005; Quirijns, 2006), reverse electrodialysis systems for electricity production (Jagur-Grodzinski and Kramer, 1986) and greenhouses (Bot, 1983; de Graaf, 2006; Speetjens et al., 2004; van Ooteghem, 2007).

Drying is an important process in the supply chain of biomass, and Gigler (2000) investigated the use of willow trees as an example. For harvested willow stems, natural wind drying can be applied. Another possibility is to chop the wood during harvest, resulting in willow chips. These chips must be dried quickly to avoid microbial degradation, and hence natural wind drying is not sufficient in this case. To optimize the supply chain, drying willow stems can be modelled as follows. The water in the stems first diffuses from the inside of the stem to the surface, then evaporates, and then the water vapour is convected from the surface out of the stack. These phenomena have been studied extensively, resulting in lumped equations describing these processes. The model predicts the drying time and the resulting costs, which can be compared to the costs related to harvesting willow chips. There are similar choices for the other steps in the supply chain, which can be analysed using models of the related physical processes. This way, the optimal supply chain to use willow as a renewable source of energy, can be designed. The model can also be used for control purposes, because changes over time can be incorporated in the model.

The second example is reverse electrodialysis, an experimental method for sustainable electricity production. There is a chemical potential difference between salt water and fresh water, which provides a renewable source of energy. Reverse electrodialysis makes this potential difference available using semipermeable membranes (Jagur-Grodzinski and Kramer, 1986; Post et al., 2007). The system performance can be analysed by comparing the energy yield with the required pumping pressure. The energy yield can be modelled with a lumped electrical resistance network, where

the relevant resistances are the water volumes and the membranes. The resulting electric current constitutes transport of sodium ions and chloride ions, introducing a link with the salt concentration. The required pumping pressure can be modelled with a global momentum balance. This model shows a trade-off between the electric resistance and the hydraulic resistance of electrodialysis plants. When the total membrane surface is increased, the electric resistance decreases because the surface elements act as parallel resistances. On the other hand, the hydraulic resistance increases due to the increasing path length of the flow. The same trade-off applies for the distance between the membranes. However, leakage electric currents have been observed, which can be modelled by adding transmission lines parallel to the membranes (Rubinstein et al., 2001). This model explains why the open circuit voltage of reverse electrodialysis stacks does not increase linearly with the number of stacked membranes, but the underlying processes are not analysed. Leakage currents may be explained by spatial variation of the driving chemical potential difference, related to local concentration differences between concentrated streams and diluted streams (Post et al., 2007). To summarize, the lumped model can be used to design reverse electrodialysis systems, but further research on the impact of spatial distribution may result in more understanding of leakage electric currents.

In the third example, greenhouses, the efficiency and the quality of the crop depend on the outside weather (Doeswijk, 2007), and on the way the indoor climate is controlled (de Graaf, 2006; Speetjens et al., 2004; van Ooteghem, 2007). The behaviour of greenhouses can be predicted using heat and mass balances. Heat sources are radiation from the sun, and heating devices in the greenhouse. Heat losses occur by ventilation and by heat conduction to the walls. The plants produce water vapour, which can be removed by ventilation. All heat and mass flows are expressed in mathematical equations (Bot, 1983; Roy et al., 2002), so the balances result in a mathematical model for the greenhouse as a whole. This model can be combined with control systems theory to design optimal control strategies (de Graaf, 2006; Tap, 2000; van Henten, 1994; van Ooteghem, 2007). However, the geometry of a greenhouse has a significant impact on energy requirements for heating and ventilation (Bot, 1983; Campen and Bot, 2003), and this impact cannot be described by lumped heat and mass balances. The impact of geometry appears in parameters, which have to be calibrated for every new greenhouse design.

These examples show that lumped engineering models can be used to design and control environmental and agricultural systems. These models are developed by identifying subsystems that can be studied in isolation. Many archetypical subsystems (e.g. resistance networks, conducting flat walls and boundary layers) are known (Batchelor, 1967; Perry and Green, 1997; Schlichting, 2000; VDI, 1988), greatly reducing the effort required for model development. Lumped models are based

on simple mathematical equations, allowing fast numerical evaluation. However, this approach has two difficulties. First, new designs in environmental and agricultural engineering may not be covered by existing lumped equations. Second, lumped engineering models are based on strong geometric simplification, and hence they are not the appropriate tool to support the design of the system geometry. When lumped modelling is not sufficient, detailed analysis is required to model the impact of spatial variation and its impact on the system performance.

1.2   Local mass, heat and momentum conservation

To model spatial variability of environmental and agricultural systems, local balances of mass, momentum and heat are required. These local balances can be developed for a very general class of problems, but this thesis focusses on environmental and agricultural systems, characterized by Newtonian (Batchelor, 1967) fluids (air and water), moderate velocities (at most 25 ms^{-1}) and moderate temperature differences (at most 30 K). These restrictions allow for the assumptions that: (a) the viscosity does not depend on the velocity field; (b) the fluid is incompressible; and (c) the material properties are constant in this temperature range.

The local balances are expressed mathematically as partial differential equations. The local total mass balance results in the continuity equation (for incompressible fluids):

$$\frac{\partial u_1}{\partial x_1} + \frac{\partial u_2}{\partial x_2} + \frac{\partial u_3}{\partial x_3} \equiv \operatorname{div} \vec{u} = 0 \tag{1.1}$$

with $\vec{x}$ the spatial coordinate vector (m), $\vec{u}$ the local velocity vector (ms^{-1}) and "div" meaning the divergence of a vector field.

Conservation of the momentum vector $\rho\vec{u}$ means that all three components are conserved, and hence three equations are required to express the local momentum balance. The local momentum balance is expressed with the Navier-Stokes equations. When ρ is the constant density (kg m^{-3}), t is the time (s), ν is the constant kinematic viscosity (m^{2}s^{-1}) and p is the pressure (Pa), the Navier-Stokes equations can be written in vector notation as:

$$\frac{\partial \vec{u}}{\partial t} + (\vec{u} \cdot \operatorname{grad})\,\vec{u} = 2\,\nu \operatorname{div} \mathbf{S} - \frac{1}{\rho}\operatorname{grad} p + \vec{f_g} \tag{1.2}$$

with "grad" being the gradient operator and $\mathbf{S}$ being the strain-rate tensor, defined by:

$$\mathbf{S}_{ij} = \frac{1}{2}\left(\frac{\partial u_i}{\partial x_j} + \frac{\partial u_j}{\partial x_i}\right) \qquad i,j = 1 \dots 3 \tag{1.3}$$

The left-hand-side of *Eqn.* (1.2) is the unsteady plus the convective acceleration of a material volume of fluid along the streamline. The right-hand-side expresses the

causes of the total acceleration, which are respectively the viscous dissipation, the pressure field and the gravity.

The local energy balance is expressed with the energy equation. When ρc is the constant volumetric heat capacity (J m^{-3} K^{-1}), T is the temperature (K) and λ is the constant thermal conductivity (W m^{-1} K^{-1}), the energy equation is written as:

$$\rho c \frac{\partial T}{\partial t} + \rho c \, \vec{u} \cdot \operatorname{grad} T = \lambda \operatorname{div} \operatorname{grad} T \tag{1.4}$$

The left-hand-side of *Eqn.* (1.4) expresses the change of the energy storage (W m^{-3}) plus the net convective transport. The right-hand-side represents the net heat conduction.

Equations (1.1) – (1.4) are valid both for laminar and for turbulent flows, but solving these equations for turbulent flows is complicated because high-frequent oscillations have to be resolved. Most engineers analyse turbulent flows by simplifying *Eqns* (1.1) – (1.4), which is achieved by averaging the local balances *Eqns.* (1.1) – (1.4) over a long time interval compared to that of the turbulent fluctuations. The continuity equation remains unchanged, but the Navier-Stokes equations (*Eqn.* 1.2) is transformed to:

$$\frac{\partial \vec{u}}{\partial t} + (\vec{u} \cdot \operatorname{grad}) \, \vec{u} = 2\,\nu \operatorname{div} \mathbf{S} + \operatorname{div} \mathbf{\Theta} - \frac{1}{\rho} \operatorname{grad} p + \vec{f_g} \tag{1.5}$$

with $\vec{u}$ now being the time-averaged velocity and $\mathbf{\Theta}$ being the specific Reynolds stress tensor (m^{2}s^{-2}), expressing the extra transport of momentum due to turbulence. This term can be modelled by introducing the turbulent kinetic energy per unit mass k (m^{2}s^{-2}) and the specific dissipation of turbulence, ω (s^{-1}), as extra flow variables. This extension results in the k-ω turbulence model, which models the extra transport of momentum with an increment of the viscosity. This increment, the kinematic eddy viscosity ν_T (m^{2}s^{-1}), is defined to be $\nu_T = k/\omega$, and it is used to approximate the specific Reynolds stress tensor $\mathbf{\Theta}$ as:

$$\mathbf{\Theta}_{ij} = 2\nu_T \, \mathbf{S}_{ij} - \frac{2}{3} \, k \tag{1.6}$$

The transport equation for the turbulent kinetic energy per unit mass k reads:

$$\frac{\partial k}{\partial t} + (\vec{u} \cdot \operatorname{grad})k = \operatorname{div}\left[(\nu + \sigma_1 \, \nu_T) \operatorname{grad} k\right] + (\mathbf{\Theta} : \mathbf{S}) - \sigma_2 \, k\omega \tag{1.7}$$

with : meaning double inner product of two tensors (resulting in a scalar), and σ_1 and σ_2 being dimensionless closure parameters. The left-hand-side of *Eqn.* (1.7) models change of turbulent kinetic energy (TKE) plus the convective transport. The first term of the right-hand-side models conduction of TKE, caused both by molecular diffusion and turbulent diffusion. The second term is the TKE production caused by the mean velocity field, and the last term models the dissipation of TKE.

The transport equation for the specific dissipation of turbulence, ω, reads:

$$\frac{\partial \omega}{\partial t} + (\vec{u} \cdot \text{grad})\omega = \text{div}\left[(\nu + \sigma_3 \nu_T)\,\text{grad}\,\omega\right] + \sigma_4\,\frac{\omega}{k}\,(\boldsymbol{\Theta} : \mathbf{S}) - \sigma_5\,\omega^2 \qquad (1.8)$$

with σ_3, σ_4 and σ_5 being dimensionless closure parameters (note that some of the $\sigma_1 \ldots \sigma_5$ are actually themselves functions of the flow variables, see references (Fluent Inc., 2007; Wilcox, 1998) for more details). Turbulent flows are also modelled using a variant of the k-ω model that introduces the dissipation of turbulence ϵ (m^2s^{-3}) as a transport variable, resulting in the k-ϵ turbulence model (Wilcox, 1998). The k-ω model and the k-ϵ model can be extended to include the effect of turbulence on heat transfer by introducing the turbulent thermal diffusivity a_T (m^2s^{-1}). Turbulent heat conduction is modelled by assuming that the turbulent Prandtl number ν_T/a_T is constant (Schlichting, 2000).

The local balances (1.1) – (1.8) apply to a very general class of transport phenomena, and they are commonly used as the starting point for spatially distributed model development. However, the equations mentioned in this section are rather complex. The reduction and simplification needed to apply the equations are the subject of Section 1.3.

1.3   Evaluation and reduction of the local balances

Modelling unknown transport phenomena in environmental and agricultural engineering, and modelling the impact of the geometry design, require local mass, heat and momentum balances as developed in Section 1.2. Computational fluid dynamics (CFD) modelling (Patankar, 1980) is a numerical method to evaluate these balances. For transient flows, a time step Δt (in s) must be chosen that is small compared to the time scale of the modelled flow phenomena. Then, the spatial domain is divided in many mesh cells, which must be fine enough to resolve all spatial variations of the flow variables. Computational fluid dynamics models use the mesh to approximate the partial differential equations with a set of algebraic equations. The unknowns of these algebraic relations are the local state variables (velocity components, pressure, temperature, turbulent kinetic energy per unit mass, and specific dissipation of turbulence) in each mesh cell. The algebraic equations relate the local state variables at a time t to the local state variables at a time $t + \Delta t$. Therefore, the dynamics of the flow is calculated by solving the algebraic relations for each consecutive time step.

The algebraic relations are nonlinear, so for each time step they must be solved by iteratively solving linear matrix equations. Large linear systems can be solved using Gaussian elimination. This method requires $\text{O}(N^3)$ multiplications, with O the Landau order symbol and N the number of equations. However, large

linear systems can also be solved iteratively, requiring $O(N^2)$ multiplications per iteration. The number of iterations is generally smaller than N, and hence the total number of multiplications [number of iterations times $O(N^2)$] is smaller than $O(N^3)$. Therefore, iterative methods are more appropriate than Gaussian elimination for large linear systems. The number of iterations required to solve a large matrix equation depends on the eigenvalues of the matrix (Driscoll et al., 1998), which are indirectly determined by the chosen mesh. The size and the quality of the mesh also affect the accuracy of the calculation, and hence it must be verified (Oberkampf and Trucano, 2002; Stern et al., 2001; Wilson et al., 2001) that solution of the algebraic relations resembles the solution of the underlying partial differential equations (Section 1.2). These aspects demonstrate that a proper choice of the mesh is crucial to CFD modelling.

The numerical procedure has been implemented in commercial software packages, for example Fluent (Fluent Inc., 2007) and Comsol (the COMSOL Group, 2007). However, long calculation times are generally required, and much knowledge is required for successful CFD modelling. The following aspects determine the complexity of CFD calculations: (a) the calculation time increases with the number of mesh cells; (b) the calculation time increases with the number of time steps; (c) the solved equations are non-linear; and (d) the quality of the mesh influences the calculation time and the accuracy of the solution. These issues are addressed with three general classes of methods, being averaging of the local balances, application of symmetry, and boundary layer theory.

An example of averaging that was presented already, is the development of the k-ω turbulence model *Eqns.* (1.5) – (1.8). The idea of averaging can also be applied to model flows in porous media (de Lemos and Mesquita, 2003; Hsu and Cheng, 1990). Flows through porous media have a complicated three-dimensional pattern, but the details of this pattern are not relevant for the macroscopic behaviour of the system. Therefore, the conservation laws are averaged over a control volume. The spatially fluctuating variables are eliminated from the model, and the spatially-averaged variables do not depend on the geometric details of the pores. Therefore, the number of mesh cells is reduced considerably.

Symmetries of the modelled flow can be applied to eliminate space dimensions. If gradients in one space dimension can be neglected, the problem can be modelled with two space dimensions (Heron and Ridd, 2001). Also in axisymmetric systems one space dimension can be neglected. The local balances can be transformed to cylindrical coordinates, and for axisymmetric systems there are no gradients in the angular direction. The idea of symmetry is very powerful, because it can be combined with differential geometry and mathematical group theory (Golubitsky and Stewart, 2003; Olver, 1986). An important application of symmetry is the development of

similarity transformations, which are a mathematical tool in boundary layer theory.

Many flows are characterised by small areas with high gradients, boundary layers and mixing layers (Schlichting, 2000; Wilcox, 1998), and boundary layer theory is the science of modelling these areas (Schlichting, 2000). Boundary layers and mixing layers have a two-dimensional structure, the relevant dimensions being the parallel and the transversal coordinate. Boundary layers and mixing layers can be analysed by assuming their thickness to be finite. Averaging over the transversal direction results in an ordinary differential equation for this thickness (Schlichting, 2000). Alternatively, an ordinary differential equation can be obtained by a similarity transformation, which is an example of a coordinate transformation. The general idea is to scale the transversal coordinate x_2 with the thickness of the boundary layer δ (m), and to introduce a new coordinate ξ as $\xi = g(x_1, x_2/\delta)$ for some function g. If the right function g is chosen, the boundary layer is characterized by an ordinary differential equation in the similarity variable ξ.

Averaging of the local balances, application of symmetry, and boundary layer theory are powerful techniques to reduce the number of mesh cells in CFD calculations. When a coarse mesh is applied, the large gradients near a boundary can be handled by introducing modified conservation laws for the related mesh cells (wall functions) (Wilcox, 1998). This way, the need for a fine mesh that resolves the gradients is eliminated. Wall functions have been applied successfully in many cases (Bosch and Rodi, 1998; Campen and Bot, 2003; Lacasse et al., 2004), but wall functions are not always accurate (Awbi, 1998), and no analogous method has been implemented for mixing layers. Combination of boundary layer theory and a turbulence model dramatically reduces the need to resolve small-scale variations of the flow. Direct numerical simulation [directly solving *Eqns.* (1.1) – (1.4)] requires about 10^7 mesh cells (Vincent and Meneguzzi, 1991), but three-dimensional CFD models based on a turbulence model and wall functions require only 10^5 – 10^6 mesh cells (Campen and Bot, 2003). Two-dimensional models are also applied for some real-life agricultural and environmental problems (Conroy et al., 2000; Heron and Ridd, 2001), and the number of mesh cells is generally about 10^4 – 10^5 (Conroy et al., 2000). Laminar two-dimensional flows require 10^3 – 10^4 mesh cells (Cruchaga and Celentano, 2003).

Furthermore, boundary layer theory has been applied to obtain lumped engineering models, commonly expressed as dimensionless power-law relations (Ameel, 1997; Gaskell, 1992; Schlichting, 2000). Heat flux through boundary layers can be described by Nusselt – Reynolds relations for forced convection flows, and Nusselt – Rayleigh correlations for natural-convection flows. Dimensionless power-law relations are applied in many engineering models, because they are applicable for a wide range of problem dimensions. However, geometry-specific features are assumed irrelevant,

and hence the impact of geometry-specific features is not modelled. Dimensionless power-law relations are generally validated with log-log regression lines, and their error is in the order of tens of percents.

It can be concluded that the above methods either result in reduced CFD models, or in lumped engineering models that do not include geometric effects. Reduced CFD models still require the development of a mesh, and the calculations also remain complicated due to the non-linearity of the governing equations. Furthermore, calculation times remain considerable due to the magnitude of the mesh. These drawbacks may be addressed by potential flow theory, which is the subject of Section 1.4.

1.4 Potential flow

Some flows can be modelled by introducing a velocity potential function ϕ (m^{2}s^{-1}), defined by $\vec{u} = \operatorname{grad} \phi$ (Batchelor, 1967). Examples are creeping flows through porous media (governed by Darcy's law) (Gaskell, 1992), and inviscous and irrotational flows (Batchelor, 1967). The potential function can be solved from the continuity equation for incompressible fluids (*Eqn.* 1.1), which transforms to Laplace's equation:

$$\operatorname{div}\operatorname{grad} \phi = 0 \qquad (1.9)$$

The system geometry influences the velocity field through the boundary conditions for *Eqn.* (1.9), because the gradient field $\operatorname{grad} \phi$ (the velocity) must be parallel to each system boundary. For two-dimensional flows through a channel, a given area flow rate (two-dimensional flow rate) (m^{2}s^{-1}) and the boundary condition $\operatorname{grad} \phi = 0$ determine a unique solution for *Eqn.* (1.9). In this case, the entire velocity field (up to a scaling factor) is determined by the geometry of the boundary.

The velocity field in a straight channel is solved by making ϕ proportional to the streamwise coordinate, corresponding to parallel flow. However, the boundaries can also have corners, which can be treated with a coordinate transformation that reduces corners into straight line segments. To develop this transformation, the two-dimensional spatial coordinates x_1 and x_2 are combined in a complex number $z = x_1 + i\,x_2$ with i the imaginary unit. Furthermore, a function ψ (the stream function, m^{2}s^{-1}) is introduced that has its gradient perpendicular to $\operatorname{grad} \phi$. Using this notation, Laplace's equation (1.9) transforms to the requirement that the complex function $z \rightarrow \phi + i\,\psi$, is differentiable (satisfies the Cauchy-Riemann equations) (Keener, 1988). The boundary condition on $\operatorname{grad} \phi$ transforms to the requirement that the stream function ψ is constant on the boundaries. Therefore, corner shapes are reduced using differentiable complex functions.

A geometry with one corner can be reduced with the transformation

$$\zeta = z^{\pi/\alpha} \tag{1.10}$$

with α the angle (rad) between the two line segments and ζ the complex coordinate on the upper half-plane (*Fig.* 1.1). Equation (1.10) is differentiable, and it multiplies the angle with π/α. Therefore, the boundary of the corner shape is taken to the real axis (*Fig.* 1.1c). The velocity magnitude is determined by the derivative of *Eqn.* (1.10), which is:

$$\frac{\mathrm{d}\zeta}{\mathrm{d}z} = (\pi \,/\, \alpha)\, z^{(\pi - \alpha)/\alpha} \tag{1.11}$$

The exponent in *Eqn.* (1.11) is positive for convex corners ($\alpha < \pi$), and negative for concave corners $\alpha > \pi$. As a consequence, a convex corner is a stagnation point of the flow, and a concave corner yields a singularity of the velocity field.

To generalize *Eqn.* (1.11) to multiple corners, mathematical analysis of the inverse transformation $\zeta \to z$ is required. Furthermore, the image of a physical corner on the ζ-plane must be introduced as a parameter, a prevertex a (Driscoll, 1996). It has been demonstrated that the transformation of a two-dimensional domain (z-plane) to the upper half-plane (ζ-plane) satisfies:

$$\frac{\mathrm{d}\zeta}{\mathrm{d}z} = K \prod_{k=1}^{n-1} (\zeta - a_k)^{(\pi - \alpha_k)/\pi} \tag{1.12}$$

with K a constant and n the number of corners (Driscoll, 1996). A modification of *Eqn.* (1.12) has been developed that maps two-dimensional channels to the infinite strip, resulting in the complex potential $\phi + i\,\psi$ for two-dimensional channel flows (Driscoll, 1996; Trefethen and Driscoll, 1998). Equation (1.12) (and its modification), does not specify the relation between the prevertices and the
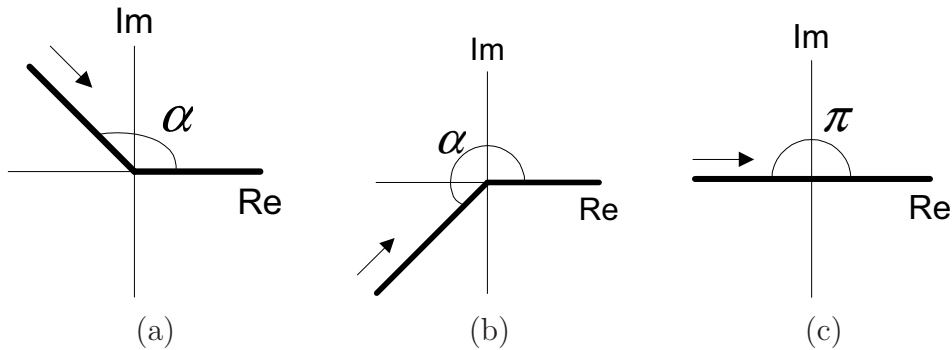

Figure 1.1: Transformation of a corner with angle α (rad) to a straight line; (a) convex corner ($\alpha < \pi$); (b) concave corner ($\alpha > \pi$); (c) straight line (angle is π)

corresponding coordinates of the physical corners. The problem of finding the prevertices that match given physical corners, is known as the parameter problem (Driscoll, 1996). The parameter problem constitutes less equations than two-dimensional CFD models, where each two-dimensional mesh cell yields five equations (u_1, u_2, p, k and ω).

To summarize, potential flow modelling has the following advantages over CFD modelling: (a) the theory directly relates the system geometry to the velocity field; (b) numerical evaluation of the velocity field does not require a mesh; (c) potential flow theory reduces the number of equations to be solved, and hence calculation times may be reduced. Most of the examples in Section 1.1 have subsystems with one inlet and one outlet, suggesting that these subsystems may be viewed as channels. However, the streamlines from the inlet to the outlet do not necessarily fill the entire channel geometry (Young and Lees, 1993; Young et al., 2000). As a consequence, the flow pattern divides the channel in a main flow area, and adjacent recirculation wakes. The recirculation wakes cannot be modelled with potential flow theory. Therefore, it is investigated whether potential flow theory can be extended to the more general flow problems with a main flow and recirculation wakes.

1.5   Problem definition

The models for designing and controlling environmental and agricultural systems are based on local heat, mass and momentum balances. Strong reduction of these balances has resulted in dimensionless power-law relations as an engineering tool, modelling idealized configurations (e.g. boundary layers, conducting flat walls, perfectly mixed vessels). The relations can be applied to model subsystems of a real-life environmental or agricultural system, resulting in a lumped engineering model. These lumped models are relatively easy to develop, and they allow fast evaluation. However, engineers can only develop lumped models if subsystems can be identified that have been examined already. New designs in environmental and agricultural engineering may not be covered by existing lumped equations. Furthermore, lumped models cannot describe the impact of geometry variations, because the impact of the geometry is subsumed in parameters that must be calibrated separately for every geometry variation.

The impact of geometry is addressed by computational fluid dynamics modelling, but CFD models generally require expert knowledge and they require long calculation times. The complexity of CFD is largely determined by the number of mesh cells, and the required number of mesh cells differs dramatically for different modelled systems. A promising method is potential flow modelling, which calculates the velocity field based on the geometry of the system boundary. This method had been

applied to channel flows without recirculation, but recirculation wakes are common in environmental and agricultural systems.

The research questions of this thesis are:

1. To which extent can lumped engineering models be applied to design spatially distributed environmental and agricultural systems?

2. How can computational fluid dynamics models be applied efficiently to design spatially distributed environmental and agricultural systems?

3. Can potential flow theory be adapted to analyse general flow problems including a main flow and recirculation wakes?

4. How can this method be utilized for environmental and agricultural engineering?

1.6 Thesis Outline

The four research questions are investigated by exploring two example problems: shell-and-tube heat exchangers driven by natural convection, and reverse electrodialysis stacks.

Chapters 2 – 3 address the research questions on lumped modelling and CFD. In Chapter 2, the heat exchanger example is examined, and a CFD model is pursued that can be evaluated with a minimal number of mesh cells. The model is validated with physical experiments, and it is applied to geometric variations of the experimental setup to investigate the usefulness for design purposes. Chapter 3 continues symmetry-based reduction, and searches for an analytic model for heat exchangers driven by natural convection. The analytic model is calibrated and validated using the CFD model of Chapter 2, which can produce reference data for geometric variations of the experimental setup. This way, the range of geometries is investigated for which the analytic model applies.

Chapter 4 to Chapter 6 examine potential flow modelling and its extension to include recirculation wakes. Chapter 4 turns to the reverse electrodialysis example. The energy conversion applies in the thin areas between the membranes, suggesting that averaging can be applied to arrive at a two-dimensional model. The small distance between the membranes causes the Reynolds number to be low. Using experimental data as reference, it is investigated whether the velocity field can be modelled with potential flow theory. The velocity field indirectly determines the performance, because the performance depends on the residence time distribution. The usefulness of the model is investigated by calculating the residence time distribution based on the velocity field.

Chapter 5 examines two-dimensional flow through a baffled channel, which is a simplification of the flow in shell-and-tube heat exchangers. Baffled two-dimensional channels are studied to examine whether potential flow modelling can be extended to flows including recirculation. Computational fluid dynamics calculations are used to produce reference data, because CFD modelling allows variation of the system geometry. The usefulness of extended potential flow modelling is examined by analysing heat transfer from the channel walls. Chapter 6 applies extended potential flow modelling to the reverse electrodialysis example. To this end, reference data is required that includes boundary layer separation, and reference data on multiple system geometries is needed. Therefore, CFD modelling results are used as the reference for extended potential flow modelling. The usefulness of the new method is examined by analysing the residence time distribution.

The calculations in Chapter 6 are based on standard algorithms of numerical analysis, but some specialized details must be described to allow for repetition of the calculations. These details are given in Appendix A. Finally, Chapter 7 will present conclusions and recommendations based on the results of Chapter 2 – Chapter 6.

Chapter 2

A Computational Fluid Dynamics Model for Designing Heat Exchangers Based on Natural Convection

Notation

A	total area of tubes, m^2
a	thermal diffusivity, m^2s^{-1}
c	heat capacity, $\text{Jkg}^{-1}\text{K}^{-1}$
D	total circumference of tubes, m
F_a	volumetric airflow, m^3s^{-1}
F_w	volumetric waterflow, m^3s^{-1}
f_g	buoyant volumetric force due to gravity, Nm^{-3}
g	acceleration of gravity, ms^{-2}
k	specific turbulent kinetic energy, m^2s^{-2}
L	characteristic length being distance between baffles, m
N	number of directions used to model radiation
Nu	Nusselt number
Q	total heat flux, W
Pe	Péclet number
Ra	Rayleigh number
T	local temperature, K
T_∞	ambient temperature for natural convection, K
T_a	local air temperature, K
T_{ai}	air inflow temperature, K
T_{ao}	air outflow temperature, K
T_{am}	mean air temperature, K
T_w	local water temperature, K
T_{wi}	water inflow temperature, K
T_{wo}	water outflow temperature, K
U	heat transfer coefficient, $\text{Wm}^{-2}\text{K}^{-1}$
V	characteristic velocity, ms^{-1}
v	local velocity, ms^{-1}
w_c	water cool-out, %
x	spatial coordinate, m
β	coefficient of thermal expansion, K^{-1}
ΔT_{lm}	logarithmic mean temperature difference, K
Δx	local grid interval length, m
λ	thermal conductivity, $\text{Wm}^{-1}\text{K}^{-1}$
ν	kinematic viscosity, m^2s^{-1}
ρ	density, kgm^{-3}
ω	specific dissipation of turbulent kinetic energy, s^{-1}

2.1   Introduction

The economic use of energy is important in the design of new types of greenhouses (Campen et al., 2003; Öztürk and Başçetinçelik, 2003). In some greenhouses, heat exchangers are used to control temperature and air humidity (Campen et al., 2003). Storage of solar energy during daytime is also gaining importance (Öztürk and Başçetinçelik, 2003). The stored energy can be used to heat the greenhouse at night.

In the Watergy project (Buchholz, 2006) these characteristics are combined. A greenhouse has been built in Spain that contains a heat exchanger connected to a closed water circuit. Excess heat in the greenhouse is transferred to the cooling-water and the warm water is stored. At night, the direction of flow can be reversed to heat the greenhouse.

To design such innovative greenhouses, simple mathematical models based on mass and energy balances are used (Bot, 1983; Roy et al., 2002), so there is a need for models that predict the performance of heat exchangers from their dimensions and the temperatures of the two flows. These models are most useful when they can be evaluated quickly.

To support the design of the Watergy heat exchanger, a prototype was built at Wageningen University, the Netherlands, and experiments were performed. The prototype was a shell-and-tube heat exchanger driven by *natural* convection as to save energy.

Many researchers have investigated natural convection in enclosures (Catton, 1978; Cruchaga and Celentano, 2003; Daloglu and Ayhan, 1999; Gaskell, 1992; Iyer and Vafai, 1997; Tanda, 1995; Xia and Qiu, 1999), and many of them summarise their results in dimensionless power-law relations. In obstructed channels, both the height and the width have a significant impact on the heat flux (Cruchaga and Celentano, 2003; Iyer and Vafai, 1997). Near obstructions, the local heat transfer coefficient has been found to increase (Cruchaga and Celentano, 2003; Daloglu and Ayhan, 1999). However, the Watergy prototype had a more complex geometry than studied in obstructed channels so far. Furthermore, the prototype did not have fixed temperatures on boundaries; the temperatures of the two streams of the heat exchanger were interconnected. For these reasons, no lumped model for the prototype is readily available from the literature.

In this article, it is investigated how the prototype can be modelled numerically. Furthermore, the objective is to find a numerical model that can be evaluated rapidly. For this reason, it is relevant to assess the importance of thermal radiation and turbulence. Finally, the usefulness of numerical models for design purposes is assessed.

2.2 Theory

2.2.1 Natural convection

For flow driven by natural convection, the volumetric buoyant force f_g in $\mathrm{Nm^{-3}}$ can be modelled using the Boussinesq approximation (Gaskell, 1992):

$$f_g = \rho g \beta (T - T_\infty) \qquad (2.1)$$

where: β is the thermal expansion coefficient in $\mathrm{K^{-1}}$; ρ is the density in $\mathrm{kg\ m^{-3}}$; g is the acceleration due to gravity $(9.8\ \mathrm{m^2 s^{-1}})$; T is the local temperature in K; and T_∞ is the ambient temperature in K. Equation (2.1) is only applicable for moderate temperature differences because the relation between pressure and temperature becomes nonlinear over large temperature ranges (Gaskell, 1992; Reizes and Leonardi, 2005).

The heat transfer coefficient U in $\mathrm{Wm^{-2}K^{-1}}$ can be modelled *via* the Nusselt number Nu:

$$Nu = U\,L/\lambda \qquad (2.2)$$

where L is a characteristic length in m and λ is the thermal conductivity of the gas in $\mathrm{Wm^{-1}K^{-1}}$. The Nusselt number is correlated with the Grashoff number Gr:

$$Gr = \frac{g\beta(T - T_\infty)L^3}{\nu^2} \qquad (2.3)$$

where ν is the kinematic viscosity. Natural convection flows are also described using the Rayleigh number $Ra = Gr\,Pr$ with Pr the Prandtl number of the fluid.

The situation of natural convection for the case of a flat plate has been solved analytically (Gaskell, 1992). Firstly, the laminar or turbulent flow regime is determined through the Rayleigh number Ra. For $Ra < 10^8$, the flow is laminar and for $Ra > 10^{10}$ the flow is turbulent (Gaskell, 1992). This criterion is also applied for other geometries (Fluent Inc., 2007). The following correlations are given (Gaskell, 1992):

$$
\begin{aligned}
Nu &= 0.59\,Ra^{1/4} && \text{(laminar flow)} && (2.4)\\
Nu &= 0.10\,Ra^{1/3} && \text{(turbulent flow)} && (2.5)
\end{aligned}
$$

2.2.2 Counterflow heat exchangers

The theory of counterflow heat exchangers starts from the local energy balance: the energy leaving the water at height x is equal to the energy received by the air at height x (Griskey, 2002). From this balance, a differential equation for the local temperature difference is derived (Griskey, 2002):

$$\frac{\mathrm{d}(T_w(x) - T_a(x))}{\mathrm{d}x} = -UD\left(\frac{1}{(\rho c)_{\text{water}}F_w} + \frac{1}{(\rho c)_{\text{air}}F_a}\right)(T_w(x) - T_a(x)) \qquad (2.6)$$

where: $T_w(x)$ is the local water temperature in K; $T_a(x)$ is the local air temperature in K; D is the total circumference of the tubes in m; c is the heat capacity in Jkg^{-1}K^{-1}; F_a is the volumetric airflow in m^{3}s^{-1}; and F_w is the volumetric waterflow in m^{3}s^{-1}.

Solving Eqn (2.6) introduces the logarithmic mean temperature difference ΔT_{lm} in K (Griskey, 2002; Sinnott, 1996):

$$Q = U A \Delta T_{lm} \tag{2.7}$$

$$\Delta T_{lm} = \frac{(T_{wo} - T_{ai}) - (T_{wi} - T_{ao})}{\ln \left[(T_{wo} - T_{ai}) / (T_{wi} - T_{ao}) \right]} \tag{2.8}$$

where: Q is the total heat flux in W; A is the area of the tubes in m^2; T_{wi} is the water inlet temperature in K; T_{wo} is the water outflow temperature in K; T_{ai} is the air inflow temperature in K; and T_{ao} is the air outflow temperature in K. In forced convection heat exchangers, U is independent of ΔT_{lm}, which explains the usefulness of Eqn (2.7).

If the waterflow or the airflow is unknown, it can be calculated from the global energy balances. As heat storage in the heat exchanger is small compared to the heat transport, the two heat fluxes can be assumed to be equal:

$$Q = (\rho c)_{\text{water}} \, F_w \, (T_{wi} - T_{wo}) = (\rho c)_{\text{air}} \, F_a \, (T_{ao} - T_{ai}) \tag{2.9}$$

2.2.3 Computational fluid dynamics

Conservation of mass, momentum and energy can be described using a set of partial differential equations: the continuity equation, the Navier-Stokes equations and the energy equation (Patankar, 1980). The CFD technique is used for numerically solving these equations. The finite volume method (Patankar, 1980) can be used to transform these partial differential equations into a finite set of algebraic equations. The unknowns are the pressure, the components of the velocity vector and the temperature at a finite number of locations in the geometry as given by the chosen mesh (Patankar, 1980). In this article, CFD modelling is performed using the commercial software packages Gambit (mesh generation) and Fluent (solving the equations for a given mesh) (Fluent Inc., 2007).

Let us now consider some aspects of CFD that are specific to this research. Turbulent flow can be modelled using the k-ω model. The k-ω turbulence model adds two spatially distributed variables: the time-averaged turbulent kinetic energy per unit mass k in m^{2}s^{-2}, and the specific dissipation of turbulent kinetic energy ω in s^{-1}. Fluent provides a correction of the k-ω model applicable for transitional flows (Fluent Inc., 2007).

For flows driven by natural convection and blackbody radiation, both mechanisms are known to have about the same importance (Gaskell, 1992). Blackbody radiation

can be modelled using the radiative transfer equation, a partial differential equation that states the conservation of radiative intensity in $\mathrm{Wm^{-2}sr^{-1}}$ (Chui and Raithby, 1993; Murthy and Mathur, 1998; Raithby and Chui, 1990). In the radiative transfer equation, not only space but also direction is an independent variable. The discrete ordinates radiation model subdivides direction into a finite number N of non-overlapping solid angles. Using the finite volume method, the radiative transfer equation can be solved at the same locations as the other partial differential equations and this yields N algebraic equations per mesh volume.

If there is a main direction of flow, the temperature at the outflow boundary of the system modelled is often unknown. (Patankar, 1980) defines the local Péclet number:

$$Pe = v\,\Delta x/a \tag{2.10}$$

where: v is the velocity perpendicular to the domain boundary in m/s; and Δx is the mesh interval length in the same direction in m/s. If $Pe \geq 10$, the local flux through the boundary can be considered to depend only on the temperature *inside* the domain. In this case, no boundary condition for the temperature is needed in the CFD model.

2.2.4 Verification and validation

To analyse the accuracy of CFD calculations, one must check that the algebraic equations of a CFD model are a good approximation of the underlying partial differential equations (verification) and one must compare the CFD results with experimental data (validation) (Oberkampf and Trucano, 2002).

For successful verification, the solution must be independent of the mesh used. This can be verified by comparing CFD models based on different meshes (Cruchaga and Celentano, 2003; Oberkampf and Trucano, 2002). For steady state calculations, the total heat and mass balances, summed over all boundaries including walls, inlets and outlets, must be zero. Furthermore, the k-ω turbulence model requires that the mesh interval length perpendicular to walls must be of the same order as the local characteristic length scale of the turbulence (Wilcox, 1998).

2.3 Materials and methods

2.3.1 The physical experiments

The prototype of the Watergy heat exchanger was located in a large experimental hall of the Wageningen University. It consisted of a vertical rectangular air channel with three rows of vertical tubes in the centre. These rows (almost) spanned the whole depth of the channel as shown in *Fig.* 2.1a. The baffles were oriented horizontally and
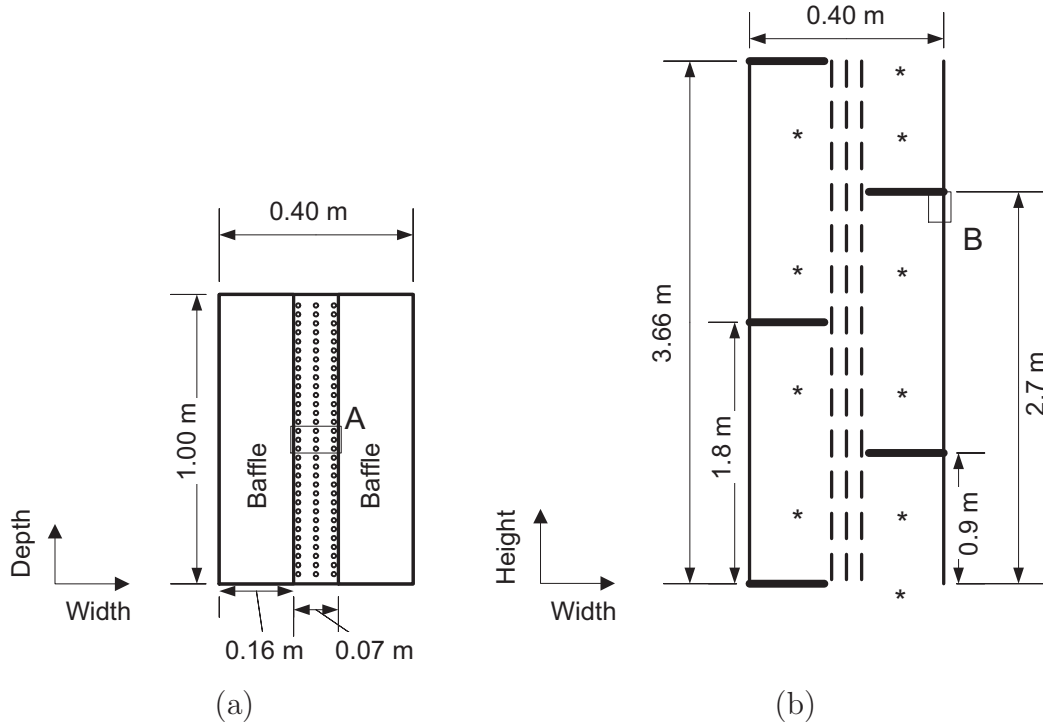
Figure 2.1: Prototype of Watergy heat exchanger (not to scale): (a) top view; with 96 × 3 tubes; (b) side view with tubes − − − and 10 air temperature sensors *; details A and B are enlarged in *Fig.* 2.2

were placed in the channel left and right from the tubes alternately as shown in *Fig.* 2.1b. The tubes were connected to a water circuit that contained a heating element. The hot water was pumped from above to realise a counter flow heat exchanger.

Dimensions not shown in *Fig.* 2.1 are the baffle thickness: 0.05 m; the tube outer diameter: 3.4 mm; and the tube wall thickness: 0.55 mm. The vertical tubes were flexible and the rows of tubes tended to bend. The depth of the rows and the distance between the baffles and the tubes could vary up to 30 mm across the vertical direction.

Temperatures in the air flow were measured by 10 temperature dependent resistances (type Pt100, accuracy about 0.1 K) (*Fig.* 2.1b) and two additional sensors were used to measure the inflow and the outflow water temperature. All sensors were connected to a Fieldpoint module (National Instruments), sampling every 10 seconds. The volumetric waterflow was measured using a liquid turbine flow meter (IR-Optflow type 3 from JLC international, accuracy about 1%). The waterflow could be controlled using a 3-way valve with a margin of less than 10%. The total maximum possible waterflow was about 800 l/h.

The experimental data were collected during two measurement series conducted in April and May 2004. During these measurements, the waterflow and the water temperature were kept constant for some time while the air temperature in the hall

remained almost constant as well. This caused a steady state situation in about a quarter of an hour. Different waterflows were applied sequentially that gave rise to 9 different steady state situations. In both series, the highest waterflows were applied before the lowest waterflows.

The experimental hall had poor climate control. The tubes, however, were part of a closed water circuit. For this reason, there was more control over the water temperature than over the air temperature during the experiments.

2.3.2 The computational fluid dynamics models

For the evaluation of blackbody radiation two different grids were used to verify the models. For this reason, the following four CFD models were compared:

1. C – the model with the coarse grid excluding radiation;

2. F – the model with the fine grid excluding radiation;

3. C_{rad} – the model with the coarse grid including radiation; and

4. F_{rad} – the model with the fine grid including radiation.

All four models included turbulence and the k-ω model was applied with a correction for transitional flows. In all four models, the Boussinesq approximation for the volumetric buoyant force was applied (Eqn 2.1). In the models C_{rad} and F_{rad}, the discrete ordinates radiation model was applied and direction was divided into a number N of 72 solid angles.

Very different length scales (*e.g.* shell width 0.40 m, tube wall thickness 0.55 mm) were present in the prototype (*Fig.* 2.1), so the geometry had to be simplified before the creation of the meshes. At first, the tubes were modelled to be rigid vertical channels. Secondly, the tubes were modelled to have a rectangular instead of a circular cross-section, but the cross-sectional area of the tubes remained unchanged. Thirdly, tubes were considered as composed only of water. Therefore the specific heat of water was corrected to obtain the total heat capacity of the real plastic tubes containing water.

Finally, two vertical symmetry planes were introduced (*Fig.* 2.2a) rendering the meshes almost two-dimensional. Only in volumes of width 10 mm around the three tube rows (depth refinement volumes), extra mesh intervals were introduced in the depth direction to allow the air to pass the tubes (*Fig.* 2.2a). The fine mesh divided the base of every depth refinement volume in 5×3 mesh areas (*Fig.* 2.2a), while the coarse mesh used 3×2 mesh areas.

The almost two-dimensional domain to be meshed resembled the side view of the prototype (*Fig.* 2.1b). The coarse mesh contained 50 mm × 10 mm cells (height
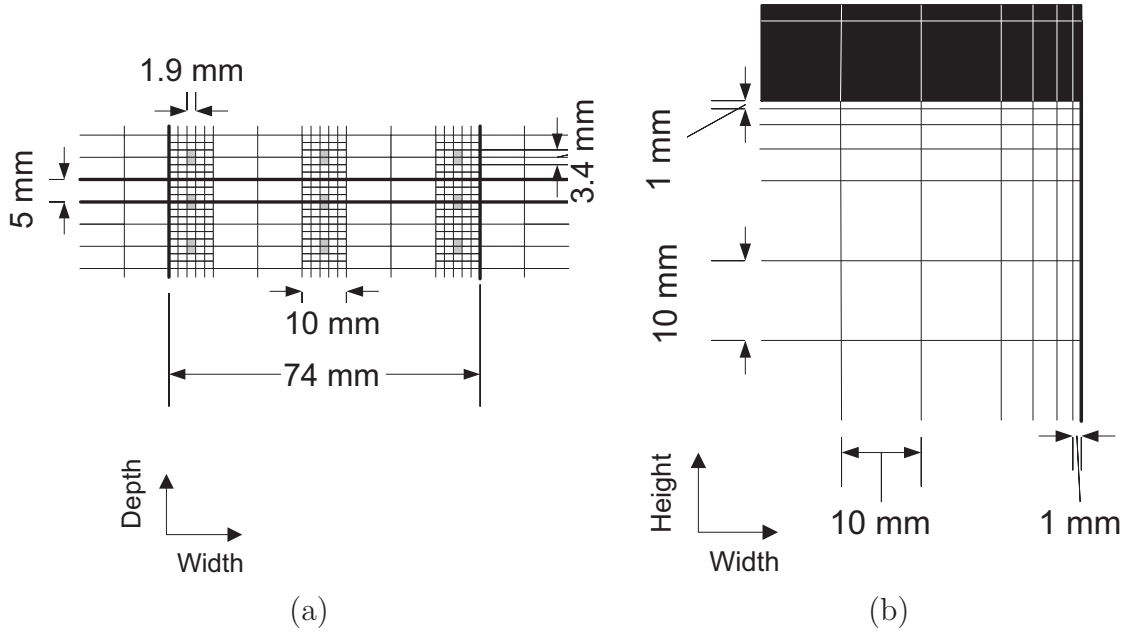
Figure 2.2: Details of 10 mm × 10 mm mesh (fine): (a) top view of three rows of water tubes (area A of *Fig.* 2.1a); symmetry planes horizontal thick lines; projections of baffles vertical thick lines; water ▢; (b) side view of corner between shell wall and baffle (area B of *Fig.* 2.1b); the baffles ■ (height 50 mm) are meshed too

× width, *Fig.* 2.1b) and the fine mesh consisted of 10 mm × 10 mm cells. Both meshes were finer near the shell walls (*Fig.* 2.2b).

Both meshes were *non-conformal*: some mesh edges contained more vertices than the end points only. This simplified the mesh generation process significantly. Different parts of the mesh were built independently and integrated afterwards.

The coarse mesh had about 6,000 mesh volumes, the fine mesh about 30,000.

Boundary conditions form an essential part of CFD models. The pressure at the bottom of the shell was modelled to be equal to the pressure at the top. The air temperature at the bottom of the shell and the ambient air temperature were fixed at T_{ai}. This implied that T_∞ in Eqn (2.1) was set to T_{ai}. Heat losses through the shell boundaries by conduction and by thermal radiation were roughly estimated via a heat transfer coefficient (Fluent Inc., 2007; Patankar, 1980). The inflow velocity of the water was assumed the same for every tube, so it was related directly to the total volumetric waterflow F_w. The inflow water temperature T_{wi} was specified also.

2.3.3 The computational fluid dynamics model calculations

To validate the CFD models, they were solved for the measured values of F_w, T_{ai} and T_{wi}. All four models were solved for the four steady states measured in April. To save calculation times, only the models C and F were solved for the five steady

states of May.

With the best model some virtual experiments were performed. As a default situation, the geometry of the experimental arrangement (*Fig.* 2.1) and the values of F_w, T_{ai} and T_{wi} corresponding to the highest measured waterflow were taken. In the experimental setup, the baffles were placed to generate a cross flow, which improves the heat transfer and impedes the flow. This made the number of baffles an important design parameter to investigate. Other relevant properties were the channel height and the channel width. A channel taller than the greenhouse requires modifications in the greenhouse design. And the channel width influences the space applicable for plants. The distance between the tubes in the width direction (*Fig.* 2.1a) was also varied. Finally, the effect of changes in the temperature range $T_{wi} - T_{ai}$ was investigated.

2.3.4 Analysis of results

To evaluate the efficiency of the water storage, the *water cool-out* w_c was defined as the temperature difference between the incoming and the outgoing water relative to its maximum:

$$w_c = \frac{T_{wi} - T_{wo}}{T_{wi} - T_{ai}} \times 100 \tag{2.11}$$

To perform model verification of local temperatures, the *verification error* between two CFD models was introduced. For every sensor of the air temperature, the difference between the modelled temperatures can be calculated. The verification error is the root-mean-square over the 10 (*Fig.* 2.1b) air temperature differences.

To compare the measurements with the literature, flow past a vertical flat plate driven by natural convection (Eqn 2.4 – 2.5) was used as a reference model. The Rayleigh number (Eqn 2.3) was formed using the vertical distance between baffles and the logarithmic mean temperature difference ΔT_{lm} in K. Note that the exact definition of characteristic length is irrelevant for turbulent flow (Eqns 2.2 – 2.3).

2.4 Results

2.4.1 The measurements

The measured waterflows range from 27 *l*/h to 767 *l*/h (Table 2.1). The air inflow temperature and the water inflow temperature are kept almost constant: the air inflow temperature remains between 24°C and 25°C, while the water inlet temperature ranges from 49°C for low waterflows to 46°C for high waterflows.

Both the heat flux and the airflow increase for increasing waterflow. This is obvious, because more waterflow means more energy supply. The water cool-out is

Table 2.1: Measured performance indicators of the prototype for the nine different waterflows

Volumetric waterflow (F_w), l/h	Total heat flux (Q), kW	Volumetric airflow (F_a), $m^3 s^{-1}$	Water cool-out (w_c), %	heat transfer coefficient (U), $Wm^{-2}K^{-1}$	Rayleigh number (Ra) $\times 10^8$
27	0.73	0.061	97.4	14.5	3.0
67	1.59	0.094	86.8	24.2	3.9
113	2.14	0.108	69.1	25.8	5.0
114	2.28	0.115	71.1	26.9	5.1
166	2.74	0.131	59.3	29.2	5.7
189	2.86	0.135	54.6	29.5	5.9
254	2.77	0.130	41.8	28.6	5.9
503	3.03	0.142	24.0	29.6	6.2
767	3.17	0.146	16.4	29.8	6.4

97% for the lowest waterflow of 27 l/h and decreases to 16% for the highest waterflow of 767 l/h (Table 2.1). The heat flux is about 3.2 kW for the highest waterflow and the resulting volumetric airflow is 0.15 m^3/s (Table 2.1). All measured steady state temperatures (*Fig.* 2.3a) show that the air becomes warmer moving upwards the channel and the air temperature changes when the air passes the tubes. There appears to be a maximum heat transfer coefficient for increasing waterflows (Table 2.1). For waterflows of 166 l/h and above, U varies between 29 Wm^{-2}K^{-1} and 30 Wm^{-2}K^{-1}. The latter value is much higher than the heat transfer coefficient from a vertical flat plate (Subsection 2.3.4). Turbulent flow past a flat plate yields a heat transfer coefficient of 2 Wm^{-2}K^{-1} and laminar flow yields 2 – 3 Wm^{-2}K^{-1} depending on the exact Rayleigh number. This demonstrates that the cross flow caused by the baffles enhances heat transfer dramatically.

Table 2.1 shows that the Rayleigh number is above 10^8. This demonstrates that the flow is not laminar, so turbulence was included into the CFD models. Furthermore, the volumetric airflow of 0.15 m^{3}s^{-1} observed for a waterflow of 767 l/h corresponds to the average air velocity being 0.62 ms^{-1}. The corresponding average Péclet number is well above 10 and this applies to the water outflow too, so no outflow temperatures need to be specified as boundary conditions (Patankar, 1980).

2.4.2 Validation and verification

For the two lowest waterflows of 27 l/h and 67 l/h, the iterative solution process for the model F does not converge. This may be explained from the *local* Péclet number (Eqn 2.10). The profile of the air velocity is not uniform at the top of the shell,
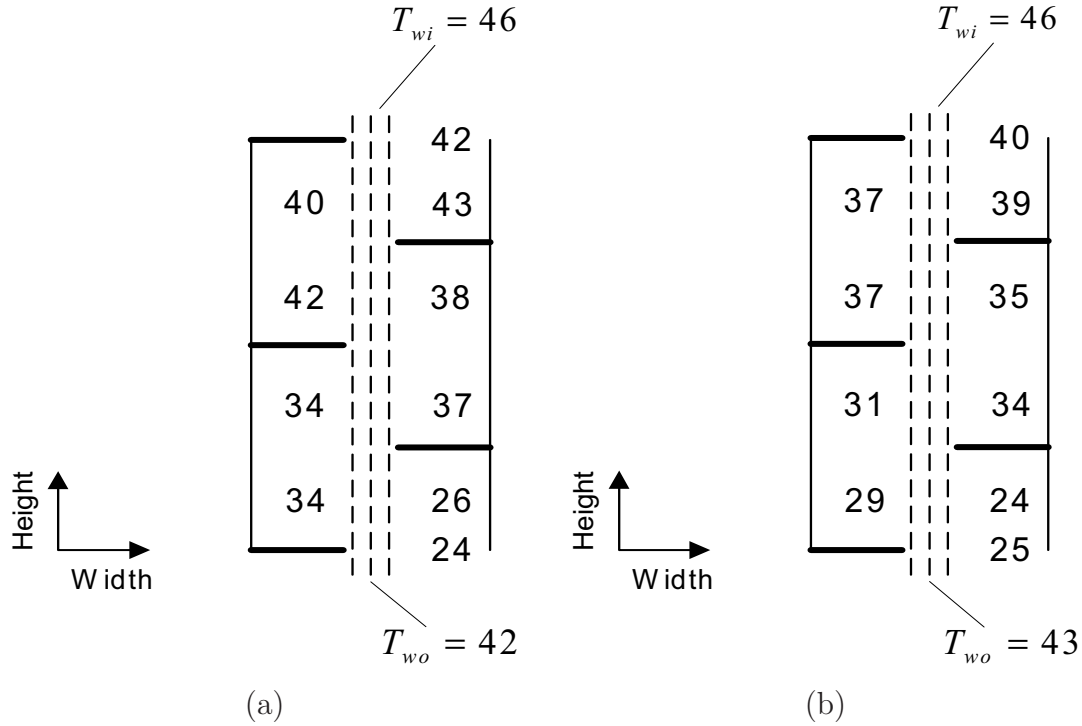
Figure 2.3: Local air temperatures in °C(10 sensors) and water temperatures (2 sensors) in °C for highest waterflow (767 *l*/h): (a) measured; (b) calculated by model F; T_{wi} and T_{wo}, water inflow and outflow temperatures, respectively

which explains that the local Péclet number can be smaller than the average Péclet number. Furthermore, the Péclet number is always less for the fine mesh than for the coarse mesh.

Table 2.2 shows the calculated heat flux relative to the measured heat flux for all waterflows and all models. The comparisons show that all CFD models have a maximum error of 30%. The model F_{rad} is the best with am maximum error of 4%; model F is second best with an error of 9%. *Figure* 2.3 compares the local temperatures according to model F with the measured local temperatures. Here larger differences occur: max 5°C for the highest waterflow of 767 *l*/h.

Table 2.2 is used for model verification also. Table 2.2 shows that the models C and F and the models C_{rad} and F_{rad} calculate about the same values for the heat flux. Furthermore, the verification error between C and F and the verification error between C_{rad} and F_{rad} are both less than 2°C (Table 2.3).

The heat flux from the tubes due to radiation according to the model F_{rad} varies between 13% and 14% of the total heat flux. The small effect of radiation can be explained from the theory of radiative exchange between surfaces (Gaskell, 1992). In *Fig.* 2.1b, it can be observed that much of the radiation emitted by a tube is intercepted through its neighbours as follows: the centre tube mainly radiates

Table 2.2: Accuracy of four models C, F, C_{rad} and F_{rad} with respect to the total heat flux, W; models with radiation were not calculated for all waterflows to save calculation time; the iterative solution process for the model F did not converge for the two lowest waterflows

Volumetric waterflow (F_w), l/h	Measured heat flux (Q), kW	Modelled heat flux relative to measured heat flux, %			
		C	F	C_{rad}	F_{rad}
27	0.73	99.3	-	-	-
67	1.59	86.7	-	-	-
113	2.14	82.0	98.6	89.4	103.5
114	2.28	79.6	96.0	-	-
166	2.74	73.7	92.3	-	-
189	2.86	72.6	91.2	-	-
254	2.77	74.4	95.0	83.4	102.9
503	3.03	70.8	92.3	80.4	101.6
767	3.17	70.2	92.6	80.1	102.0

Table 2.3: Verification errors between coarse and fine grid for models without radiation, C – F, and with radiation, C_{rad} and F_{rad}, for different waterflows; the models C_{rad} and F_{rad} were not calculated for all waterflows to save calculation time

Waterflow, (l/h)	Temp. range $(T_{wi} - T_{ai})$, K	Verification error, K	
		C – F	$C_{rad} - F_{rad}$
113	23.6	0.8	0.8
254	22.5	1.4	1.4
503	21.6	1.7	1.6
767	21.7	1.8	1.8

towards the neighbouring tubes, just like the central parts of the outer tubes. This explanation suggests that the effect of radiation would be more important for one tube row instead of three rows. Finally note that the difference between the heat fluxes calculated by model F and model F_{rad} is about 8%, which is even less than the heat flux attributed to radiation by F_{rad}. There appears to be a compensation effect.

Calculation times varied strongly: without radiation it took minutes, with radiation hours (C: 3 minutes, F: 8 minutes, C_{rad}: 3 hours and F_{rad}: 6 hours). The combination of accuracy and calculation time renders the models C and C_{rad} unsatisfactory as engineering tools. The accuracy of F is acceptable, which makes it the preferred engineering tool.

2.4.3 Virtual experiments

After the validation and verification of the CFD models, some virtual experiments can be carried out with the model with fine mesh, excluding radiation: model F. With these experiments the performance of different heat exchanger designs is evaluated. First the number of baffles is considered. For three baffles, the volumetric airflow is higher than for five baffles (Table 2.4), but the heat transfer coefficient is lower. The

Table 2.4: Influence of design parameters of heat exchanger on heat flux, volumetric air flow and heat transfer coefficient, calculated using model with fine mesh without radiation (F); default situation: geometry of *Fig.* 2.1, waterflow $F_w = 767$ l/h, air inflow temperature $T_{ai} = 24$ °C, water inflow temperature $T_{wi} = 46$ °C

Modelled variation	Default value	Total heat flux (Q), kW	Volumetric airflow (F_a), $m^3 s^{-1}$	Heat transfer coefficient (U), $Wm^{-2}K^{-1}$
Default	-	2.93	0.147	23.6
3 baffles	5 baffles	2.97	0.174	21.4
7 baffles	5 baffles	2.68	0.121	23.8
9 baffles	5 baffles	2.36	0.098	23.0
Width 80 cm	40 cm	3.43	0.197	25.0
Width 30 cm	40 cm	2.59	0.122	22.0
Height 2.0 m	3.66 m	1.68	0.088	22.8
Height 5.0 m	3.66 m	3.71	0.182	22.7
Tube distance 10 mm (width)	32 mm	2.47	0.131	18.0
Tube distance 20 mm (width)	32 mm	2.88	0.139	23.7
Air temperature T_{ai} of 42°C	46°C	2.26	0.134	23.0
Air temperature T_{ai} of 50°C	46°C	3.62	0.158	24.0

resulting heat flux is almost the same. For seven baffles, the volumetric airflow is lower than for five baffles, but heat transfer coefficient is higher. This demonstrates the expected trade-off between the resistance to the flow caused by the baffles and the increased heat transfer caused by the cross-flow.

Secondly the shell width is considered. The heat flux increases for increasing shell width (Table 2.4), but increasing the depth (*Fig.* 2.1a) has more impact on the heat flux. If the channel width is 0.30 m, the heat flux is 2.59 kW. In this calculation, the channel width is decreased with 25%, but the heat flux decreases only 12% compared to the modelled heat flux for 0.40 m (2.93 kW).

The shell height is important also. If the shell height is increased with 37% (to 5 m), the heat flux increases with 27% (to 3.71 kW) (Table 2.4). This shows, however, that adding tubes is more efficient than increasing the shell height.

The heat flux does not depend very critically on the distance between the tubes

(Table 2.4). The heat flux remains almost the same if the distance between the tubes is decreased from 32 mm to 20 mm. This demonstrates the validity of the model assumption that the tubes are rigid vertical channels (Subsection 2.3.2). For a tube distance of 10 mm, however, the heat flux decreases significantly.

Finally the efficiency of the heat exchanger slightly increases with increasing temperature difference $T_{wi} - T_{ai}$. If $T_{wi} - T_{ai}$ increases with 18% ($T_{wi} = 50°C$), the heat flux increases with 24% (Table 2.4).

The results of the virtual experiments have been summarised in a dimensionless power-law relation. The Rayleigh number explains the Nusselt number very well: the correlation coefficient of $\log Nu$ and $\log Ra$, derived from the virtual experiments, is 97%. The relation resulting from linear regression reads:

$$Nu = 1.57 Ra^{0.30} \qquad (2.12)$$

The exponent in Eqn (2.12) is close to the value 1/3 common for turbulent free-convection flow (Gaskell, 1992) that would make the heat flux independent of the baffle distance (Eqn 2.2 – 2.3). The exponent in Eqn (2.12) is almost the same as the value 0.29 found for natural convection in a long vertical enclosure (Catton, 1978); and 0.28 found for Rayleigh-Bénard convection with Rayleigh number around 10^9 (Xia and Qiu, 1999).

2.5 Conclusion

A system with a complex geometry (a shell-and tube heat exchanger) has been modelled using computational fluid dynamics models. The system was driven by natural convection and temperature differences were moderate. From the Rayleigh number it was clear that the flow was not laminar. It has been demonstrated that many features of the geometry can be simplified. A non-conformal mesh works, which simplifies the mesh generation process considerably. The Boussinesq approximation is sufficient to relate gas density to temperature. The k-ω model with a correction for transitional flows has been proved to suffice as a turbulence model.

Models including and not-including thermal radiation were compared and the accuracy of the model not-including thermal radiation was still acceptable. The reason is that the tubes were close to each other and intercepted much of the radiation from their neighbours. This is important, because thermal radiation requires about 60 times more calculation time (using the discrete ordinates radiation model).

The computational fluid dynamics models have made it possible to analyse the impact of many different changes of the geometry. The experimental heat exchanger appears to be fairly efficient. Its width (dimension perpendicular to tube rows) is 0.40 m and its height is 3.66 m. If the temperature difference between incoming water

and incoming air is 22°C, a heat flux of 2.9 kW is achieved (according to the CFD model with the fine mesh and excluding radiation). The corresponding heat transfer coefficient is 23 $\mathrm{Wm}^{-2}\mathrm{K}^{-1}$. The only way to improve the heat transfer coefficient significantly (to 25 $\mathrm{Wm}^{-2}\mathrm{K}^{-1}$) is by doubling the channel width, but adding an extra heat exchanger has much more impact on the heat flux.

The baffles are extremely important to promote heat transfer. Without the baffles, the heat transfer coefficient would only be 2 – 3 $\mathrm{Wm}^{-2}\mathrm{K}^{-1}$. The optimal number of baffles is between three and five. If three baffles are used, the volumetric airflow becomes higher than with five baffles, so using three baffles promotes ventilation.

Increasing the shell width and increasing the shell height both have a positive impact on the heat flux. Doubling the shell width yields a gain of 17% for the heat flux and increasing the shell height with 37% (to 5 m) yields a gain of 27%. The heat flux does not depend very critically on the tube distance, but the tubes must not be too close to each other.

The most efficient use of base area can be achieved by *decreasing* the width of the heat exchanger. If the shell width is reduced with 25% (to 0.30 m), the heat flux only decreases with 12%. From the two-dimensional structure of the CFD models it is clear that the heat flux is proportional to the depth of the heat exchanger (dimension parallel to tube rows), provided that extra tubes are added if the depth is increased. So decreasing the shell width can be compensated through increasing the depth.

To maximise the water flow is not a good strategy to use the heat exchanger. According to the measurements, a water flow of 166 l/h yields a heat flux of 2.74 kW. If the water flow is increased with a factor 4.6 (to 767 l/h), the heat flux only increases with 16%. Furthermore, the difference between the water outflow temperature and the water inflow temperature is dramatically decreased which reduces the usefulness of the stored water.

Finally the difference between the water inflow temperature and the ambient air temperature has a positive impact on the heat flux. If the water inflow temperature increases with 18% (to 50°C), the heat flux increases with 24%.

Chapter 3

Modelling of Natural-Convection Driven Heat Exchangers

Notation

A	horizontal open area next to a baffle, m^2
F	total buoyant force, N
H	heat exchanger height, m
N_b	number of baffles
N_t	number of tubes
Q	heat flux, W
T_a	air temperature, K
T_w	water temperature, K
$\bar{U}$	local heat transfer coefficient, W m^{-2} K^{-1}
U	average heat transfer coefficient, W m^{-2} K^{-1}
W	shell width, m
c	heat capacity, J kg^{-1} K^{-1}
c_d	drag coefficient
c_{dc}	drag coefficient per chamber
d	outer circumference of a tube, m
f_g	volumetric buoyant force, N m^{-3}
g	acceleration of gravity, m^{2}s^{-1}
v	average air velocity, ms^{-1}
x	vertical coordinate, m

Greek symbols

ΔT_{lm}	logarithmic mean temperature difference, K
ΔT_{am}	air mean temperature, K
ΔP	pressure drop, Pa
Ω	air volume, m^3
β	thermal expansion coefficient, K^{-1}
ρ	density, kg m^{-3}
ϕ_a	volumetric air flow rate, m^{3}s^{-1}
ϕ_w	volumetric water flow rate, m^{3}s^{-1}

3.1 Introduction

Indoor climate in buildings and greenhouses can be conditioned through heat exchangers (Bot, 2001; Campen et al., 2003). Heat exchangers are designed and dimensioned using physical models that predict the heat flux from the inflow

and outflow temperatures, and from the volumetric flow rates. Commonly, heat exchangers are driven by forced convection, and this type of heat exchangers can be modelled with the logarithmic mean temperature difference as driving force for heat exchange (Griskey, 2002; Sinnott, 1996). Forced convection requires energy, however, and hence energy may be saved when heat exchangers are based on *natural* convection.

Applying natural convection introduces the volumetric flow rate as an extra quantity that depends on the acting temperature differences. At the same time, the temperature differences are affected by the residence time, which depends on the volumetric flow rate. Furthermore, the phenomenon of natural convection is commonly modelled with a relation between the heat transfer coefficient and the temperature difference (Gaskell, 1992). As a consequence, the theory on heat exchangers must be adapted for heat exchangers driven by natural convection.

In a project on innovative greenhouses (Speetjens et al., 2004), application of a water-to-air shell-and-tube heat exchanger driven by natural convection was considered. A prototype of such a heat exchanger was built at Wageningen University, the Netherlands (Speetjens et al., 2004). The water flowed from the top to the bottom, and its temperature was higher than the air temperature. The air is heated, causing an upward buoyant force in the shell. This way, counter flow was realised. A numerical model based on Computational Fluid Dynamics (CFD) (Patankar, 1980) was developed, which was validated with experimental data (Dirkse et al., 2006). It was demonstrated that thermal radiation could be ignored, making natural convection the only transport mechanism in the CFD model.

Computational Fluid Dynamcs models require expensive software and long calculation times, and hence a lumped model would be a useful alternative for design purposes. This article aims for a lumped model of shell-and-tube heat exchangers driven by natural convection. It is investigated whether a lumped model can be derived analytically. After this, the relevance of the analysis for the experimental heat exchanger is examined.

3.2   Analysis

Shell-and-tube heat exchangers can be idealised in one dimension as shown in *Fig.* 3.1. The spatial coordinate is x (m), and the local water temperature and the local air temperature are $T_w(x)$ and $T_a(x)$ (K) respectively. The heat exchanger has height H (m). The heat flux from the water to the air, Q (W), can be modelled by two
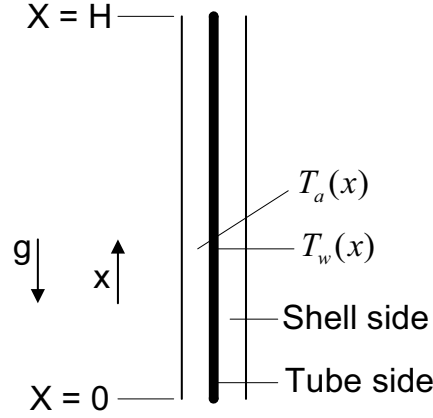
Figure 3.1: Ideal heat exchanger with spatial coordinate x (m), heat exchanger height H (m), local water temperature (tube side) $T_w(x)$ (K), local air temperature (shell side) $T_a(x)$ (K) and acceleration of gravity $g = -9.8 \text{ ms}^{-2}$

global energy balances:

$$Q = (\rho c)_a \, \phi_a \, (T_a(H) - T_a(0)) \tag{3.1}$$

$$Q = -(\rho c)_w \, \phi_w \, (T_w(H) - T_w(0)) \tag{3.2}$$

where $(\rho c)_a$ is the volumetric heat capacity of air ($\text{Jm}^{-3}\text{K}^{-1}$), $(\rho c)_w$ is the volumetric heat capacity of water, ϕ_a is the volumetric air flow rate (m^3s^{-1}) and ϕ_w is the volumetric water flow rate.

The local energy balance of the air in the shell at position x reads (Griskey, 2002):

$$(\rho c)_a \, \phi_a \, \frac{\mathrm{d}T_a(x)}{\mathrm{d}x} = \bar{U}(x) \, N_t \, d \, \Delta T(x) \tag{3.3}$$

where $\bar{U}(x)$ is the local heat transfer coefficient ($\text{W m}^{-2} \text{ K}^{-1}$), N_t is the number of tubes, d is the outer circumference of a tube (m), and $\Delta T(x)$ is the local temperature difference, $\Delta T(x) = T_w(x) - T_a(x)$. An equation similar to *Eqn.* (3.3) holds for the water temperature $T_w(x)$. These equations can be combined into a single equation for $\Delta T(x)$. When the local heat transfer coefficient is assumed to be space-independent, $\bar{U}(x) \equiv U$, a solution is found for $\Delta T(x)$ (Griskey, 2002):

$$\frac{\Delta T(x)}{\Delta T(0)} = \left(\frac{\Delta T(H)}{\Delta T(0)} \right)^{x/H} \tag{3.4}$$

Integrating the right-hand-side of *Eqn.* (3.3) while substituting *Eqn.* (3.4), results in (Sinnott, 1996):

$$Q = U \, N_t \, d \, H \, \Delta T_{lm} \tag{3.5}$$

with

$$\Delta T_{lm} = \frac{\Delta T(H) - \Delta T(0)}{\ln[\Delta T(H)/\Delta T(0)]} \qquad (3.6)$$

where $N_t\, d\, H$ is the area of all tubes and ΔT_{lm} is defined as the logarithmic mean temperature difference (K), which, according to *Eqn.* (3.5), can be considered as the driving force in the theory on forced convection heat exchangers.

When the volumetric air flow rate ϕ_a is driven by natural convection, the volumetric air flow rate ϕ_a depends on the temperature profile. At the same time, the outflow temperature $T_a(H)$ is determined by ϕ_a as can be seen in *Eqn.* (3.1). Therefore, evaluation of the logarithmic mean temperature difference (*Eqn.* 3.6), which drives the heat flux, requires a relation for ϕ_a. This relation can be developed from the momentum balance between the friction force and the buoyant force. It is investigated whether the buoyant force can be characterised by an algebraic expression of the inflow and outflow temperatures. The starting point of this analysis is the Boussinesq approximation (Gaskell, 1992), which states that the volumetric buoyant force f_g ($\mathrm{Nm^{-3}}$) is proportional to the relative air temperature:

$$f_g = \rho_a\, g\, \beta\, [T_a(x) - T_a(0)] \qquad (3.7)$$

where ρ_a is the air density ($\mathrm{kg\ m^{-3}}$), g is the acceleration of gravity ($\mathrm{ms^{-2}}$) and β is the thermal expansion coefficient in $\mathrm{K^{-1}}$. Equation (3.7) is valid for moderate temperature differences, maximally about 30 K for air (Reizes and Leonardi, 2005). The thermal expansion coefficient can be derived from the ideal gas law. Integration of *Eqn.* (3.7) shows that the total buoyant force F (N) is proportional to the relative air mean temperature ΔT_{am}:

$$F = \rho g\, \beta\, \Omega\, \Delta T_{am} \qquad (3.8)$$

where Ω is the air volume within the heat exchanger ($\mathrm{m^3}$).

An expression for ΔT_{am} can be obtained by integrating *Eqn.* (3.3). All system parameters can be eliminated using *Eqns.* (3.1), (3.2) and (3.5), resulting in:

$$
\begin{aligned}
T_a(x) - T_a(0) \;=\;& \frac{[T_a(H) - T_a(0)]\,\Delta T(0)}{\Delta T_{lm}\,\ln[\Delta T(H)/\Delta T(0)]} \times \ldots \\
& \left[\left(\frac{\Delta T(H)}{\Delta T(0)} \right)^{x/H} - 1 \right]
\end{aligned}
\qquad (3.9)
$$

Averaging *Eqn.* (3.9) results in:

$$\Delta T_{am} = [T_a(H) - T_a(0)]\frac{\Delta T_{lm} - \Delta T(0)}{\Delta T(H) - \Delta T(0)} \qquad (3.10)$$

Equation (3.10) demonstrates, that the buoyant force induced by the air temperature profile can be characterised by an algebraic relation of the inflow and outflow

temperatures. The temperature difference that drives the air flow, is the average of the inflow and the outflow air temperature multiplied with a dimensionless representation of the logarithmic mean temperature difference. The buoyant force must be related to the volumetric air flow rate to complete the lumped model for shell-and-tube heat exchangers driven by natural convection. This relation depends on the geometric features of the heat exchanger, and hence the one-dimensional idealisation *Fig.* 3.1 is not sufficient for this step. Geometry specific features of the lumped model are examined based on the experimental heat exchanger, see Section 3.3.

3.3 Materials and methods

3.3.1 Calibration and validation data

A heat exchanger driven by natural convection was built at Wageningen University (Speetjens et al., 2004). It consisted of a vertical rectangular air channel with three rows of vertical tubes in the centre. These rows spanned the whole depth of the channel as shown in *Fig.* 3.2. The baffles were oriented horizontally and were placed in the channel left and right from the tubes alternately as shown in *Fig.* 3.3. The
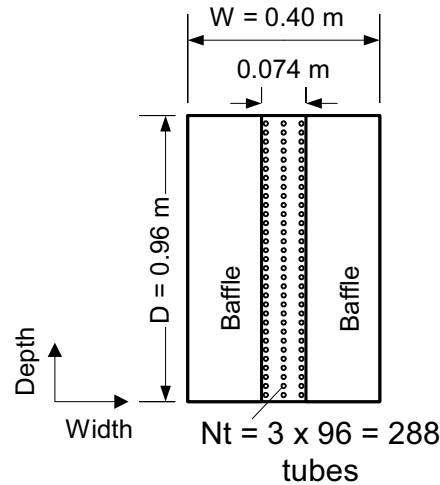

Figure 3.2: Top view of experimental heat exchanger, having $N_b = 5$ baffles; dimensions not shown: tube outer circumference $d = 10.7$ mm; tube wall thickness: 0.55 mm

tubes were connected to a water circuit that contained a heating element. The hot water was pumped from above to realise a counter flow heat exchanger. Important dimensions are the number of baffles $N_b = 5$, the shell height $H = 3.66$ m, and the shell width $W = 0.40$ m (*Fig.* 3.3). The total area of all tubes was $N_t dH = 11.3$ m^2.
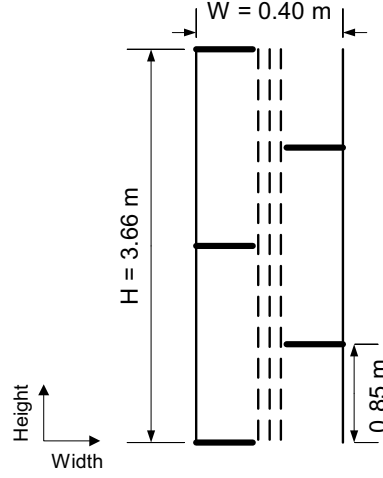
Figure 3.3: Side view of experimental heat exchanger; dimensions not shown: baffle thickness 0.05 m

Experimental results were not sufficient to calibrate a lumped model, because the dimensions of the experimental heat exchanger could not be varied. Therefore, the Computational Fluid Dynamics (CFD) model developed in our earlier publication (Dirkse et al., 2006) was used to generate calibration and validation data. The input variables of the CFD model were the water flow ϕ_w (m^{3}s^{-1})), the ambient air temperature $T_a(0)$ and the inflow water temperature $T_w(H)$. Seven different volumetric water flow rates were applied ranging from 213 ml s^{-1} to 31.5 ml s^{-1}, while $T_a(0)$ was 24°C and $T_w(H)$ was about 47°C. Additionally, two calculations were performed with $T_w(H) = 50$ °C and $T_w(H) = 42$ °C. Furthermore, the CFD model was evaluated for variations of the number of baffles N_b, for variations of the heat exchanger height H (m), and for variations of the heat exchanger width W (m) (*Fig.* 3.3). These variations were evaluated with the highest water flow of 213 ml s^{-1} as model input. The total number of CFD model calculations was 16.

3.3.2 Calibration and validation procedure

First, the key assumption in the analysis of Section 3.2 was checked, being the one dimensional approximation (*Fig.* 3.1). This assumption was checked by comparing the one-dimensional air mean temperature ΔT_{am} *Eqn.* (3.10) with the three-dimensional average as the reference, which could be calculated from the temperature field. The Boussinesq approximation could be applied, because the difference between the water temperature and the air temperature was less than 30 °C.

After this validation of the analysis, the analytic equations were extended with geometry specific parameter values and equations. Firstly, a relation between the

volumetric air flow ϕ_a and the buoyant force F was developed. The CFD simulations in (Dirkse et al., 2006) demonstrated that the flow meanders around the baffles and that the flow is turbulent. Therefore, the theory of forced-convection flow through appendages was expected to apply. The pressure drop ΔP (Pa) is defined as $\Delta P = F/A$ with A the horizontal open area next to a baffle (m^2). The average air velocity v (ms^{-1}) is defined as ϕ_a/A, and a quadratic relation between v and ΔP is generally assumed. This proportionality factor is modelled via the drag coefficient c_d defined as:

$$c_d = \frac{\Delta P}{1/2 \, \rho_a \, v^2} \tag{3.11}$$

The air volume also may be considered as a series of appendages, where the individual appendages are the areas between consecutive baffles (chambers). The drag coefficient per chamber, c_{dc}, is defined as $c_{dc} = c_d/(N_b - 1)$.

The validity of *Eqn.* (3.11) for the experimental heat exchanger was checked based on the CFD calculations about the original geometry; seven variations of the volumetric water flow rate plus two variations of the inflow water temperature makes nine cases. For fixed geometry, the pressure drop ΔP is proportional to the driving temperature difference ΔT_{am} (*Eqn.* 3.10), and the velocity v is proportional to ϕ_a. Therefore, linear regression of v^2 against ΔT_{am} can be applied.

The analysis of Section 3.2 also leaves the heat transfer coefficient U as an unknown parameter. Values for U were derived from the CFD calculations indirectly: the logarithmic mean temperature difference ΔT_{lm} was calculated with *Eqn.* (3.6) and division of Q through the total tube area and ΔT_{lm} produced U (see *Eqn.* 3.5). These values for U were examined to see whether U depends on the temperature profile or if it is constant.

The analysis of Section 3.2 extended with values for the parameters c_d and U, makes a complete lumped model. The heat flux is proportional to ΔT_{lm} and the volumetric air flow rate ϕ_a is a function of ΔT_{am} via the calibrated relation with the average air velocity v. After these substitutions, the global energy balances *Eqns.* (3.1) - (3.2) depend only on the five variables $T_a(0)$, $T_a(H)$, $T_w(0)$, $T_w(H)$ and ϕ_w, leaving only two unknowns: $T_a(H)$ and $T_w(0)$. These unknowns can be solved iteratively using Sequential Quadratic Programming (Schittowski, 1985), which is available in the software package MatLab (the Math Works, 2006). The definition of ΔT_{lm} (*Eqn.* 3.6) cannot be evaluated directly if the iterative algorithm tries temperatures such that $\Delta T(H) \approx \Delta T(0)$, because the denominator $\ln[\Delta T(H)/\Delta T(0)]$ becomes zero. However, linear approximation shows that ΔT_{lm} equals the linear average of $\Delta T(0)$ and $\Delta T(H)$ close to this singularity.

The lumped model was evaluated 16 times for the same inputs as were applied in the 16 CFD calculations, and the geometry-specific values for c_d and U were used

as the parameters. The heat flux Q and the volumetric air flow rate ϕ_a according to the lumped model were compared to the CFD data as reference. After this, the parameter values c_d and U were related to the design parameters N_b, H and W to see whether the lumped model can explain the impact of geometry changes. The values of the drag coefficient per chamber, c_{dc} were examined to see whether the shell can be considered as a series of appendages. Finally, the lumped model results were compared to the original physical measurements on the experimental heat exchanger.

3.4   Results and discussion

Computational Fluid Dynamics models were applied to generate calibration data and validation data. The CFD model for the experimental geometry and the highest water flow of 213 ml s^{-1} calculated a heat flux Q of 2.93 kW and a volumetric air flow rate ϕ_a of 0.147 m^{3}s^{-1}. These values decreased for decreasing water flow rate, because there was less energy supply. Increasing the number of baffles N_b increased the friction force, impeding the air flow and decreasing the heat flux as a consequence. Finally, increasing the channel height and the channel width increased Q and ϕ_a.

A value for the heat transfer coefficient U was derived from the CFD results by dividing Q through the total area of the tubes and through the logarithmic mean temperature difference. The resulting value was about 23, which was considerably lower than the experimental value of about 28 reported in (Speetjens et al., 2004). This difference is explained by three-dimensional features of the air temperature profile, which cause model errors in all four temperatures $T_a(0)$, $T_a(H)$, $T_w(0)$ and $T_w(H)$; these four temperatures all appear in *Eqn.* (3.6). The model error for U is also caused by the absence of black-body radiation in the CFD model. Because of the uniformity of the calculated U values and the large errors of the CFD models for U, U was included in the lumped model as a temperature-independent parameter.

The air flow was driven by the difference between the average air temperature and the inflow air temperature. Computational Fluid Dynamics models calculate the entire temperature field, allowing the driving temperature difference to be extracted directly. This value was used as a reference to check the one-dimensional approximation *Eqn.* (3.10), see *Fig.* (3.4). The difference between the 1D and the 3D average was at most one Kelvin, confirming the analysis of Section 3.2. The one-dimensional approximation of the driving temperature difference ΔT_{am} was correlated with the square of the average velocity v for the nine cases corresponding to the original geometry, and the R^2 of the regression was 99.5%. Furthermore, evaluation of c_d for the nine cases yielded values between 7.8 and 8.1, demonstrating the applicability of the drag coefficient to model ϕ_a.

The drag coefficient c_d was calculated for every geometry (Table 3.1), and the
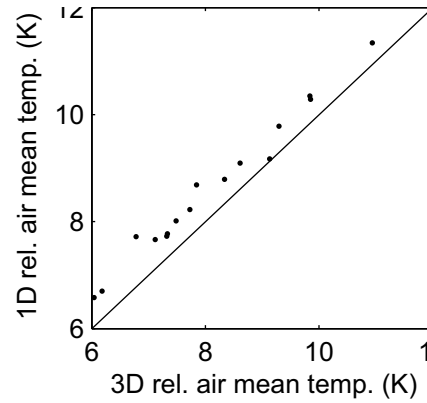
Figure 3.4: Comparison of 1D relative air mean temperature (*Eqn.* 3.10) to 3D relative air mean temperature from CFD calculations

Table 3.1: Impact of geometry changes on parameters U and c_d of lumped model, and comparison with the drag coefficient per chamber c_{dc}; N_b is number of baffles; H is heat exchanger height; W is heat exchanger width (Fig. 3.3)

Geometry change (-)	Lumped model parameters		Drag cf. per chamber c_{dc} (-)
	Heat transfer cf. U Wm^{-2}K^{-1}	Drag cf. c_d (-)	
Default	24	7.8	1.9
$N_b = 3$ (5)	21	4.4	2.2
$N_b = 7$ (5)	24	13.0	2.2
$N_b = 9$ (5)	23	21.8	2.7
$W = 0.30$ m (0.40)	22	5.2	1.3
$W = 0.80$ m (0.40)	25	20.2	5.0
$H = 2.0$ m (3.66)	23	10.5	2.6
$H = 5.0$ m (3.66)	23	7.4	1.8

lumped model can evaluate the heat flux Q and the volumetric air flow ϕ_a with 5% accuracy when the geometry-specific values for the parameters c_d and U are supplied. The drag coefficient c_d is highly dependent on the geometry. The default geometry, having a baffle count N_b of 5, a height of 5.0 m and a width of 0.40 m, has $c_d = 7.8$ (Table 3.1, row 1 column 3). Increasing the number of baffles increases the drag coefficient dramatically to 21.8 for nine baffles. Increasing the channel width also increases c_d, and increasing the channel height decreases the drag coefficient. Division of the drag coefficient through the number of chambers, which is the definition of c_{dc}, explains the impact of the baffle count. The drag coefficient per chamber only

ranges from 2.0 to 2.7 when the baffle count ranges from 3 to 9.

Increasing the shell width from 0.40 m to 0.80 m increases the drag coefficient per chamber c_{dc} from 2.0 to 5.0 (Table 3.1) , but changing the height from 3.66 m to 5.0 m only changes c_{dc} from 2.0 to 1.8 (Table 3.1). These numbers show, that c_{dc} is not proportional to the ratio of the vertical baffle distance to the shell width W. The sharpness of the bends in the flow pattern is expected to be the determining factor, but more research is needed to check this assumption.

Finally, the heat fluxes calculated by the lumped model with $U = 23$ $\text{Wm}^{-2}\text{K}^{-1}$ and $c_d = 7.8$ were compared to the experiments of (Speetjens et al., 2004) as reference. Nine water flows were applied ranging from 213 ml s^{-1} to 7.4 ml s^{-1}. For the highest water flow, the experimental heat flux is 3.2 kW, while the lumped model calculates 2.9 kW. The difference is 9%. For the other volumetric water flow rates, the error for the heat flux is below 9% as well. The water flow is calculated with 18% accuracy. It is remarkable that the lumped model works for the lowest water flow of 7.4 ml s^{-1}, because a heat transfer coefficient of only 15 $\text{Wm}^{-2}\text{K}^{-1}$ was measured for this case (Dirkse et al., 2006). The good performance of the lumped model can be explained, because the heat flux is not constrained by the heat transfer coefficient, but by the amount of heat energy available in the water (*Eqn.* 3.2).

3.5 Conclusion

A lumped model for shell-and-tube heat exchangers driven by natural convection has been developed. The heat exchanger is modelled as two adjacent vertical tubes; one tube contains upward air flow and one tube contains downward water flow. This representation implies that the driving temperature difference for the heat flux is the logarithmic mean temperature difference, which is known from the theory on forced convection. Using the Boussinesq approximation, the buoyant force can also be characterised by a driving temperature difference, being the relative average air temperature. The relative average air temperature can be expressed analytically as a function of the inflow and outflow temperatures. The theory of forced convection through appendages can be used to relate the buoyant force to the friction force. This analysis results in a lumped model with only two parameters: the heat transfer coefficient and the drag coefficient. The lumped model has non-linear equations, but these can be solved iteratively using Sequential Quadratic Programming.

During earlier research, an experimental heat exchanger was built, which was modelled successfully using Computational Fluid Dynamics. These CFD model results can be used for model calibration and validation. If the heat transfer coefficient and the drag coefficient are known, the lumped model approximates the CFD results on heat flux and volumetric air flow rate with 5% accuracy. The

heat flux is fairly insensitive to geometry changes (about 23 $\mathrm{Wm^{-2}K^{-1}}$ according to the reference CFD calculations), but the drag coefficient depends strongly on the geometry. The impact of the baffle count can be explained by considering each area between baffles (chamber) as a separate appendage. The drag coefficient per chamber varies between 2.0 and 2.7 when the baffle count is varied between 3 and 9. Finally, the lumped model approximates physical measurements of the heat flux with 9% accuracy, and physical measurements of the volumetric air flow with 18%. This result applies to all possible volumetric water flow rates even though the heat transfer coefficient drops considerably for low water flow rates. The lumped model is accurate for low volumetric water flow rates, because the heat flux is not constrained by the heat transfer coefficient, but by the amount of heat available in the water.

The one-dimensional model was validated for upward air flow and downward water flow, but the analysis suggests that arbitrary flow directions can be modelled. For downward air flow, the ambient air temperature becomes the air temperature at the top, called $T_a(H)$, instead of the air temperature at the bottom, called $T_a(0)$. Therefore, the driving temperatures difference becomes $T_{am} - T_a(0) - [T_a(H) - T_a(0)]$ (where T_{am} is the absolute average air temperature, K), allowing the expression found for $T_{am} - T_a(0)$ to be applied.

To summarise, the lumped model is applicable for shell-and-tube heat exchangers if their geometry is fundamentally one-dimensional and if the driving temperature differences are moderate (small enough to allow for the Boussinesq approximation). The analysis describes heat exchangers driven by natural convection as if they were driven by forced convection, suggesting that the analysis can easily be extended to mixed-convection heat exchangers.

Chapter 4

Extending Potential Flow Modelling

Notation

c	image of source on upper half-plane (complex number), m
d	image of sink on upper half-plane (complex number), m
i	imaginary unit
p	pressure, Pa
q	velocity magnitude, ms^{-1}
s	spatial coordinate along a streamline, m
u	one-dimensional velocity, ms^{-1}
u_{max}	velocity maximum over transversal direction, ms^{-1}
$\vec{u}$	average two-dimensional velocity vector, ms^{-1}
t	time, s
$\vec{x}$	spatial coordinate vector, m
z	complex spatial coordinate, m
$R(\psi)$	residence time of a streamline, s

Greek symbols

δ	gasket thickness, m
ζ	complex coordinate on upper half-plane
ζ_s	complex coordinate on infinite strip
η	viscosity, Pa s
ϕ	potential function, m^2s^{-1}
ϕ_0	potential function corresponding to reference location, m^2s^{-1}
ϕ_A	area flow rate, m^2s^{-1}
ϕ_V	volumetric flow rate, m^3s^{-1}
ψ	stream function, m^2s^{-1}
Ψ	cumulative residence time distribution

4.1 Introduction

The efficiency of many chemical and biological plants is determined by the residence time distribution (Levenspiel, 1972). The residence time distribution depends on the velocity field, which is determined by the system geometry (Shilton et al., 2000). Therefore, a careful design of the system geometry can improve the system efficiency (Darcovich et al., 1997; Ghidossi et al., 2006). This article focusses on membrane technology systems that have a flat-sheet geometry. The efficiency of membrane-based systems, which can be analysed based on the residence time distribution, is influenced by velocity gradients transversal to the membranes (Wiley and Fletcher,

2003; Balster et al., 2006; Ghidossi et al., 2006), but velocity gradients in the two spatial directions parallel to the membranes may also be relevant (Batchelor, 1967). These effects can be modelled based on local mass, momentum and energy balances, expressed in partial differential equations with three space dimensions (Batchelor, 1967). Computational Fluid Dynamical (CFD) modelling (Patankar, 1980) is a numerical method to solve these local balances. However, the problem is that three-dimensional CFD models generally require long calculation times. Furthermore, CFD modelling requires expert knowledge, because the geometry has to be meshed and the mesh quality determines the solution accuracy.

In order to develop a relatively simple tool, the three-dimensional problem may be reduced to two dimensions by averaging the three-dimensional local balances over the limited height (Hsu and Cheng, 1990; de Lemos and Mesquita, 2003). This way, the two-dimensional superficial velocity vector remains to be modelled. The membranes are typically very close to each other (one millimetre or less), causing the Reynolds number to be low. Therefore, the superficial velocity field may be modelled as a potential flow (Batchelor, 1967). Potential flow theory calculates the pressure and the velocity field based on a conformal map (Batchelor, 1967; Keener, 1988), which maps the physical plane onto the infinite strip. However, membrane-based systems often are not single-connected, because the inlet and the outlet of a cell (area between membranes) are not located on the boundary. The research questions are: (a) can potential flow theory be applied to bounded geometries with internal inlets and outlets; (b) can potential flow theory be extended to model the residence time distribution?

4.2 Theory

4.2.1 Modelling the velocity field

The example that motivates this research is reverse electrodialysis (Jagur-Grodzinski and Kramer, 1986; Post et al., 2007), an experimental method for electricity generation. In reverse electrodialysis stacks, spacers are applied to support the membranes. However, it is not possible to do experiments with a cell including a spacer, because there is an open volume between the spacer and the membranes. The geometry of this open area cannot be controlled, and hence its impact cannot be modelled. Therefore, an experimental setup without a spacer was investigated, see Section 4.3.

The distance between the membranes is typically one millimeter or less, which is small compared to the membrane area. Therefore, the flow can be considered to be two-dimensional, and the small membrane distance causes the Reynolds number to be

small. Low-Reynolds-number two-dimensional flows can be modelled using potential flow theory (Batchelor, 1967; Peng et al., 1999). The friction force is determined by the velocity being zero on the membrane surfaces (no-slip condition), introducing transversal velocity gradients. The impact of these gradients can be modelled based on the theory of parallel flow between flat plates, which states that (Gaskell, 1992)

$$\frac{\mathrm{d}p}{\mathrm{d}s} = -\frac{12\,\eta}{\delta^2} u \tag{4.1}$$

with $\mathrm{d}p/\mathrm{d}s$ the pressure drop in the streamwise direction (N m^{-3}) (averaged over the transversal direction), η the viscosity (Pa s), δ the distance between the plates (m), and u the average velocity (m s^{-1}). Equation (4.1) models one dimension parallel to the membranes (the s-direction), and the second parallel dimension is added by replacing the scalar velocity u with the two-dimensional average velocity vector $\vec{u}$, and by replacing $\mathrm{d}p\,/\,\mathrm{d}s$ with grad p.

The average velocity $\vec{u}$ can be modelled by defining a potential function ϕ (m^{2}s^{-1}) as:

$$\phi = -\frac{\delta^2}{12\eta}\,p \tag{4.2}$$

which transforms *Eqn.* (4.1) to grad $\phi = \vec{u}$. According to the continuity equation (Batchelor, 1967), the potential function ϕ must satisfy Laplace's equation:

$$\mathrm{div}\,\mathrm{grad}\,\phi = 0 \tag{4.3}$$

The boundary condition for *Eqn.* (4.3) comes from the requirement that there is no fluid flow through the boundary of the two-dimensional domain, which is expressed as the boundary condition that grad ϕ is parallel to the two-dimensional boundary.

Laplace's equation (*Eqn.* 4.3) can be solved using complex function theory. The two spatial coordinates x_1 and x_2 (m) are combined in a complex number $z = x_1 + ix_2$, with i the imaginary unit. Furthermore, a function ψ (the stream function, m^{2}s^{-1}) is introduced that has its gradient perpendicular to grad ϕ. Using this notation, Laplace's equation (*Eqn.* 4.3) transforms to the requirement that the complex function $z \rightarrow \phi + i\,\psi$, is differentiable (satisfies the Cauchy-Riemann equations) (Keener, 1988). The geometric meaning of the Cauchy-Riemann equations is that small area elements are not deformed, and hence differentiable complex functions are conformal maps. The boundary condition on grad ϕ transforms to the requirement that the stream function ψ is constant on the boundaries. When the volumetric flow rate is ϕ_V (m^{3}s^{-1}), the corresponding area flow rate must be $\phi_A = \phi_V/\delta$ (m^{2}s^{-1}). Therefore, flows in single-connected channels are characterized by the boundary conditions $\psi = 0$ on one wall, and $\psi = \phi_A$ on the other wall.

However, reverse electrodialysis cells are characterized by multiply-connected domains, because the inlet and the outlet are holes in the membranes. Extra

boundary conditions are required for the boundaries of the holes. This problem can be solved by modelling the inflow and outflow holes as a point source and a point sink, and by mapping the membrane area to the upper half-plane instead of the infinite strip, see *Fig.* 4.1. The source and the sink are mapped to some locations
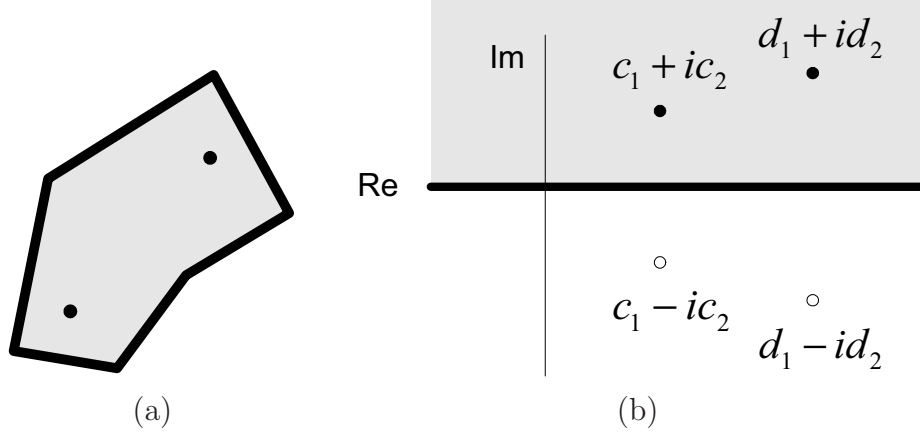

Figure 4.1: Conformal map from physical domain (a) to the upper half-plane ζ (b)

$c_1 + i\, c_2$ and $d_1 + i\, d_2$ respectively. The requirement that the area flow rate through the system is ϕ_A, transforms to the following boundary conditions: the stream function must increase with ϕ_A for each counter-clockwise rotation around $c_1 + i\, c_2$, and the stream function must increase with $-\phi_A$ for each counter-clockwise rotation around $d_1 + i\, d_2$. These conditions are satisfied by the functions $(\phi_A\,/\,2\pi)\ln(\zeta - c_1 - i\, c_2)$ and $(-\phi_A\,/\,2\pi)\ln(\zeta - d_1 - i\, d_2)$ respectively, with ζ the complex coordinate on the upper half-plane (Batchelor, 1967).

The boundary condition that the stream function ψ is constant on the outer boundary, transforms to the requirement that the stream function ψ is symmetric around the real axis. This boundary condition can be satisfied by adding a virtual source and a virtual sink as illustrated in *Fig.* 4.1. The virtual source and the virtual sink are located at $c_1 - i\, c_2$ and $d_1 - i\, d_2$, which are the complex conjugates of the real source and the real sink. The complex potential can be modelled by adding the two sources and two sinks together, resulting in:

$$\phi + i\psi = \frac{\phi_A}{2\pi} \ln \left(\frac{(\zeta - c_1)^2 + c_2^2}{(\zeta - d_1)^2 + d_2^2} \right) \tag{4.4}$$

The resulting velocity field follows from differentiating *Eqn.* (4.4), resulting in:

$$u_1 - iu_2 = \left[\frac{\phi_A}{\pi} \frac{\zeta - c_1}{(\zeta - c_1)^2 + c_2^2} - \frac{\phi_A}{\pi} \frac{\zeta - d_1}{(\zeta - d_1)^2 + d_2^2} \right] \frac{\mathrm{d}\zeta}{\mathrm{d}z} \tag{4.5}$$

Conformal maps from polygonal domains can be evaluated numerically using the Schwarz-Christoffel theorem (Batchelor, 1967; Driscoll, 1996). However, direct numerical evaluation of *Eqns.* (4.4) and (4.5) is sensitive to a numerical problem called crowding (Driscoll, 1996; Trefethen and Driscoll, 1998). This numerical problem does not occur when the membrane area is mapped to the infinite strip ζ_s instead of the upper half-plane ζ. Therefore, the problem of crowding can be eliminated with the substitution $\zeta = \exp(\pi\zeta_s)$ in *Eqn.* (4.4), resulting in the substitution $\mathrm{d}\zeta/\mathrm{d}z = \mathrm{d}\exp(\pi\zeta_s)/\mathrm{d}z = \pi\exp(\pi\zeta_s)\,\mathrm{d}\zeta_s/\mathrm{d}z$ in *Eqn.* (4.5). The calculation steps resulting from this mathematical analysis are given in Table 4.1, describing how the velocity field is evaluated. A similar calculation based on *Eqn.* (4.4) yields the complex potential.

Table 4.1: The following calculation steps must be applied to calculate the average velocity vector (u_1, u_2) in a physical location (x_1, x_2):

1. Set $z = x_1 + i\,x_2$;

2. evaluate a conformal map from the physical domain to the unit strip, resulting in a complex value ζ_s;

3. set $\zeta = \exp(\pi\zeta_s)$;

4. evaluate $\mathrm{d}\zeta_s/\mathrm{d}z$;

5. set $\mathrm{d}\zeta/\mathrm{d}z = \pi\exp(\pi\zeta_s)\,\mathrm{d}\zeta_s/\mathrm{d}z$;

6. evaluate *Eqn.* (4.5) to calculate the complex velocity;

7. the real part of this complex number is the horizontal velocity u_1, and the imaginary part is the minus of the vertical velocity, $-u_2$.

Steps 2 and 4 can be performed using a free software library programmed by Driscoll (1996).

4.2.2 Modelling the residence time distribution

The residence time distribution influences the efficiency of reverse electrodialysis stacks. It can be calculated from the convection-diffusion equation. This is a partial differential equation, and hence computational fluid dynamics modelling is required for its numerical evaluation. Therefore, a reduced model for the residence time distribution is searched by extending potential flow theory. In Peng et al. (1999), the energy equation, which resembles the convection-diffusion equation, is transformed to have the spatial coordinates replaced by the potential function ϕ and the stream function ψ. It was demonstrated that the conductive term has derivatives with respect to both ϕ and ψ, but the convective term is reduced to have only a derivative with respect to ϕ. This result suggests, that a reduced model for the residence time

distribution may be found by neglecting diffusion.

However, the transversal gradients caused by the no-slip condition induce dispersion. In parallel flows between flat plates, the velocity is maximal midway between the plates, and the maximal velocity u_{max} equals (Gaskell, 1992)

$$u_{max} = 3/2 \, u \tag{4.6}$$

The present research aims for a reduced model that predicts the impact of the two-dimensional geometry, and therefore dispersion is not included in the reduced model. It is investigated whether the reduced model is still in qualitative agreement with measurements.

When diffusion and dispersion are neglected, there is no mass transport between adjacent streamlines. Furthermore, this assumption implies that each fluid particle following a particular streamline has the same residence time. This residence time can be calculated as follows: Let s be the spatial coordinate along a streamline (m), and consider the travelling time over a small line segment ds. This travelling time dt (s) depends on the magnitude of the velocity, q (ms^{-1}), via the relation $dt = ds/q$. The spatial coordinate s can be transformed as $ds = d\phi/q$, resulting in a travelling time $dt = d\phi/q^2$. As a consequence, the residence time $R(\psi)$ (s) of a streamline becomes:

$$R(\psi) = \int_{-\infty}^{\infty} \frac{d\phi}{q(\phi, \psi)^2} \tag{4.7}$$

Numerical evaluation of $R(\psi)$ requires a method to calculate the velocity magnitude q from the complex potential $\phi + i\,\psi$ (see *Eqn.* 4.7). In particular, the complex potential $\phi + i\,\psi$ must be mapped back to the upper half-plane ζ to allow evaluation of *Eqn.* (4.5). Equation (4.4) can be used to solve ζ from $\phi + i\,\psi$, as follows: applying the exponential map to both sides of *Eqn.* (4.4) yields:

$$\exp\left(\frac{2\pi(\phi + i\psi)}{\phi_A}\right) = \frac{(\zeta - c_1)^2 + c_2^2}{(\zeta - d_1)^2 + d_2^2} \tag{4.8}$$

Multiplying *Eqn.* (4.8) with the denominator yields a square equation in ζ, allowing for an explicit solution.

To calculate the residence time distribution, consider a tracer particle that is injected at time zero. The cumulative residence time distribution $\Psi(t)$ is found by calculating the chance (dimensionless) that the particle leaves before a given time t (s). The particle leaves before time t if and only if it flows over a streamline ψ satisfying $R(\psi) < t$. Therefore, the chance equals the fraction of the streamlines that satisfies $R(\psi) < t$. This fraction can be defined formally as:

$$\Psi(t) = \frac{1}{\phi_A} \int_0^{\phi_A} 1_{\{\psi \,|\, R(\psi) < t\}} \, d\psi \tag{4.9}$$

with $1_{\{\psi \,|\, R(\psi)<t\}}$ being the indicator function of the set $\{\psi \,|\, R(\psi) < t\}$. The residence time distribution is the time derivative of the cumulative residence time distribution, and hence the residence time distribution has unit s^{-1}.

The chance $\Psi(t)$ was evaluated numerically using an iterative algorithm that solves ψ from the equation $R(\psi) = t$. The residence time distribution was evaluated by numerical differentiation of $\Psi(t)$.

4.3   Materials and methods

4.3.1   Measurements to validate the velocity field model

In Subsection 4.2.1, a numerical method was developed that approximates the velocity field and the pressure in flat-sheet geometries. The model was validated using an experimental setup that measures local pressures (*Fig.* 4.2), which was located at the Wetsus institute, Leeuwarden, the Netherlands, where Reverse Electrodialysis is being investigated. The core was a stack of a horizontal Perspex plate at the bottom, a gasket and a horizontal Perspex plate on top (*Fig.* 4.2, numbers 4 – 5), supported by a PVC plate to improve the stiffness as explained later (*Fig.* 4.2, number 6). A gasket was a sheet of transparent foil (RA Bindings, Haarlem, the Netherlands), and a shape was cut out of it to allow water flow between the plates. Local pressures could be measured through twelve holes in the Perspex, where lockable tubes were attached (*Fig.* 4.2, number 7). These tubes could be connected to a differential pressure gauge (*Fig.* 4.2, number 8) (Endress+Hauser Messtechnik GmbH+Co, type PMD70), having an error bound of 20 Pa. A hole close to the inflow tube was used as the reference, leaving eleven pressure differences to be measured.

The use of Perspex as the plate material allowed the water flow to be observed during the experiments, and it appeared that degassed water had to be used to prevent air bubbles. Therefore, a reservoir was included in the water circuit (*Fig.* 4.2, number 1), which was filled with boiled water before the start of the experiments. The experiments started when the water was cooled to the environment temperature (20 °C– 25 °C).

The experimental setup was designed to study the flow in the flat-sheet geometry between the horizontal Perspex plates, enabling variation of the Reynolds number and the two-dimensional geometry. The Reynolds number was varied by varying the water flow rate and the geometry thickness. The water flow was driven by two parallel peristaltic pumps (Masterflex L/S pumps, model 77200-60) (*Fig.* 4.2, number 2), maximum flow rate 9 ml s^{-1}. The accuracy of the flow rate was checked by a weighing procedure. Fluctuations of the water flow were damped through a locked tube filled with air, which was connected behind the pumps (*Fig.* 4.2, number 3).
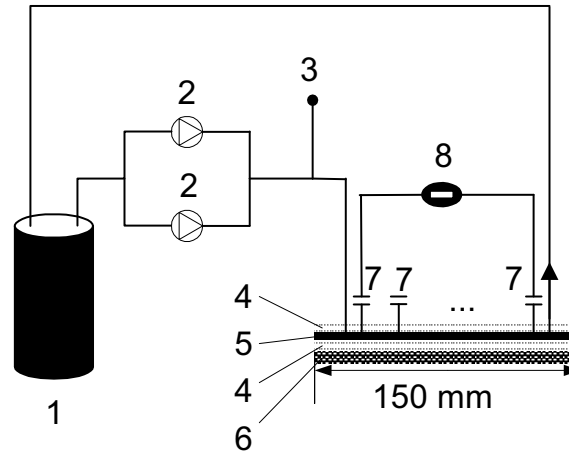
Figure 4.2: Water circuit; 1 = degassed water reservoir, 2 = peristaltic pumps; 3 = locked tube filled with air; 4 = Perspex plate; 5 = gasket with a shape cut out to allow water flow; 6 = PVC plate; 7 = lockable tube that can be connected to differential pressure gauge; 8 = differential pressure gauge

The geometry thickness was determined by the gasket thickness, and experiments were performed for gasket thicknesses 0.20 mm and 1.0 mm. However, the forces that applied the gasket between the plates deformed the Perspex. To analyse the importance of this effect, the deformation was measured using feeler gauges. At the bottom, deformation was inhibited by the PVC plate shown in *Fig.* 4.2 (number 6). The thickness of 1.0 mm corresponded to a hydraulic diameter of 2.0 mm, and in combination with the maximum flow rate of 9 ml s^{-1}, the maximum Reynolds number investigated was 600 (based on a channel width of 32 mm, see *Fig.* 4.3).

The two-dimensional geometry was determined by the shape cut out of the gasket. Four different gasket shapes were investigated as shown in *Fig.* 4.3. The default gasket applied at Wetsus, had no fins (*Fig.* 4.3a, gasket no-fin). A large variation of the residence time was expected, and it was investigated whether the residence time variation could be reduced by introducing two fins (*Fig.* 4.3b, gasket double-fin). Two gaskets with sudden expansion (*Fig.* 4.3c, gasket long-fin, and *Fig.* 4.3d, gasket short-fin) were examined for the sole purpose of model validation. The diameter of the inflow tube and the outflow tube was 8 mm, which was small compared to the gasket width of 150 mm. This feature justifies that the inflow and the outflow tubes are modelled as a point source and a point sink.

Local pressures were measured for six combinations of the gasket shape and the gasket thickness, see Table 4.3. For each geometry (shape and thickness combination), seven different water flow rates between 1 ml s^{-1} and 9 ml s^{-1} were applied. Eleven pressure differences were measured for each flow rate, resulting in
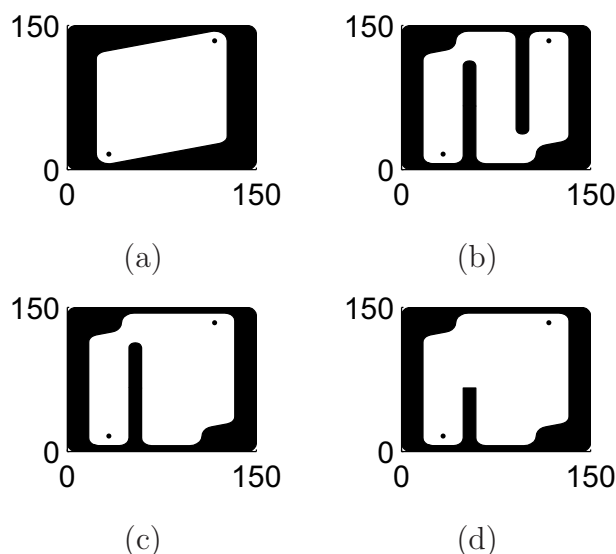
Figure 4.3: Gasket shapes no-fin (a), double-fin (b), long-fin (c) and short-fin (d); dimensions in mm

77 measured local pressure differences per geometry. This large number of local pressures could be applied to reduce the impact of measuring errors. Measured pressure differences could be normalised to potential function values ϕ (m^{2}s^{-1}) using *Eqn.* (4.2). Linear regression of the measured ϕ-values against the applied area flow rates was applied to check the linear relation between the pressure and the velocity (*Eqn.* 4.1). The slope of the regression line is an estimate for the dimensionless potential ϕ/ϕ_A, which is based on seven measured local pressures. For each geometry, there are eleven dimensionless potentials, because the differential pressure gauge allowed measurement of eleven pressure differences. Linear regression of the measured dimensionless potentials against the corresponding model predictions was applied to analyse the model accuracy for a geometry.

4.3.2 Measurements to validate the residence time distribution model

The experimental setup of *Fig.* 4.2 was also used to validate the model for the residence time. Blue ink was injected through the inflow tube, and the flow of the ink was filmed with a digital camera (type Medion MD-9090), which produced twenty-five frames per second. A clock was projected in each frame, providing a time measurement with an accuracy of 0.12 s. To have a clear view, the top Perspex plate in *Fig.* 4.2 was replaced by another one that had no connection holes, and the bottom Perspex plate was removed. To support quantitative analysis of the films, twelve locations were marked on the PVC plate. The travelling time of the ink front

to each marked location was visually recorded, allowing validation of *Eqn.* (4.7). Equation (4.7) models the travelling time from the inflow ($\phi = -\infty$) to the outflow ($\phi = \infty$), and hence a small modification is required to model the travelling time to an interior location. The underlying conformal map provides the potential function ϕ_0, and hence the correct travelling time is obtained by restricting the integration interval to $-\infty \leq \phi \leq \phi_0$. In addition to the travelling times to the twelve marked locations, the time of first arrival at the outlet was recorded. This time was compared to the minimum residence time according *Eqn.* (4.7).

4.4   Results and discussion

4.4.1   Validation of the velocity field model

The experimental setup was used to investigate the flow in flat-sheet geometries, and the velocity field was analysed indirectly using the measurement of local pressures. Figure 4.4 shows a typical measurement of the pressure field, which was measured for the long-fin gasket with a thickness of 1.0 mm, and with the water flow being 9.1 ml s^{-1}. The pressure decreases from the source to the sink, and the pressure was almost constant in the dead zone next to the fin.

The local pressures were measured for seven flow rates, and the relation between the local pressure and the flow rate was linear as expected. For the long-fin gasket with thickness 1.0 mm, the regression R^2 over seven flow rates was at least 97.1%. The slope of the regression line was transformed to the dimensionless potential (Table 4.2 column 3). The trends observed for a single flow rate, *Fig.* 4.4, also were observed from the measured dimensionless potentials: The dimensionless potential increases along the flow, and similar values are observed in the dead zone next to the fin. Comparison of different geometries revealed that the pressure was much higher for geometry thickness 0.2 mm, which was expected from the theory of flow between flat plates (*Eqn.* 4.1).

The measurements were conducted to validate the model, which was based on potential flow theory. Linearity between the pressure and the velocity was assumed, making the dimensionless potential independent of the volumetric flow rate. The model is based on a conformal map to the infinite strip, $\phi + i\psi$, shown in *Fig.* 4.5. There are more potential lines near the inflow and the outflow than in the centre, indicating that the velocity is larger in these regions because the velocity vector is the gradient of the potential. Furthermore, there are more streamlines near the diagonal than to the sides, indicating higher velocities there. The potential flow model predicts large variations of the velocity, which are shown in *Fig.* 4.6 for the long-fin gasket (*Fig.* 4.3c).
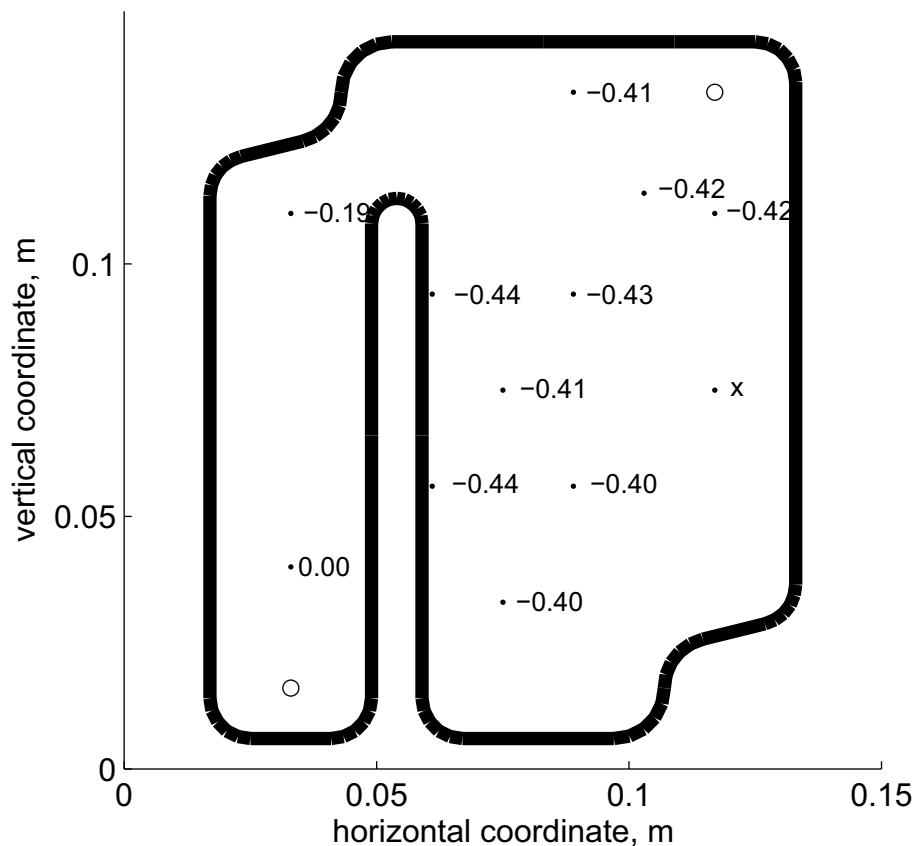
Figure 4.4: Measured pressures in kPa for the long-fin gasket with thickness 1.0 mm and water flow rate 9.1 ml s^{-1}; x = erroneous measurement

Both the measurements and the model provided values for the dimensionless potential, making it a suitable quantity for model validation. Table 4.2 shows reasonable agreement for the long-fin gasket and geometry thickness 1.0 mm. To get a quantitative measure of agreement, linear regression was applied between the measured (dependent variable) and the modelled (independent variable) dimensionless potentials. For the long-fin gasket with thickness 1.0 mm (*Fig.* 4.2), an R^2-value of 96.4% was obtained. The same regression was applied for the other measured geometries, see Table 4.3. For thickness 1.0 mm, the regression R^2 was at least 94.1%, with the exception of the measurement of the short-fin gasket. This measurement failed because water could flow over the fin. The regression slope was reasonably close to one, indicating that there were no large systematic errors. The two measurements with thickness 0.2 mm had larger systematic errors, because the Perspex deformation was relatively more important (the thickness had an error of maximally 0.1 mm). The regression R^2 is 98%, however, indicating good agreement of the model.

Table 4.2: Measured and modelled dimensionless potential for the long-fin gasket (*Fig.* 4.3c) and thickness 1.0 mm; x = erroneous measurement

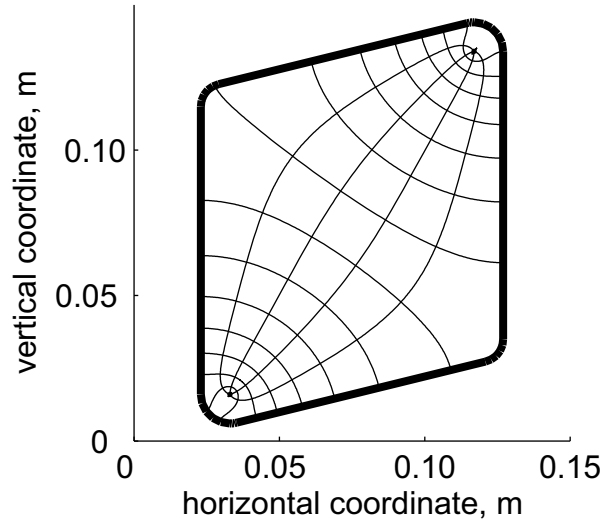| measuring location (*Fig.* 4.3)		dimensionless potential ϕ/ϕ_A	
horicontal coordinate	vertical coordinate	measured	modelled
33	40	0.0	0.0
33	110	1.9	2.2
61	56	4.2	3.8
61	94	3.9	3.7
75	33	3.4	3.9
75	75	4.0	3.8
89	56	3.9	3.9
89	94	4.2	3.8
89	134	3.8	3.9
103	114	4.1	4.0
117	75	x	3.9
117	110	4.0	4.1

Figure 4.5: Conformal mapping from the no-fin gasket (*Fig.* 4.3a) to the infinite strip, taking the source and the sink to ∞

4.4.2 Validation of the residence time distribution model

The experimental setup was also used to obtain reference data for the residence time distribution. A tracer was injected at the inflow, and the travelling time to thirteen marked locations (twelve marked locations and the outlet) were recorded. Figure 4.7
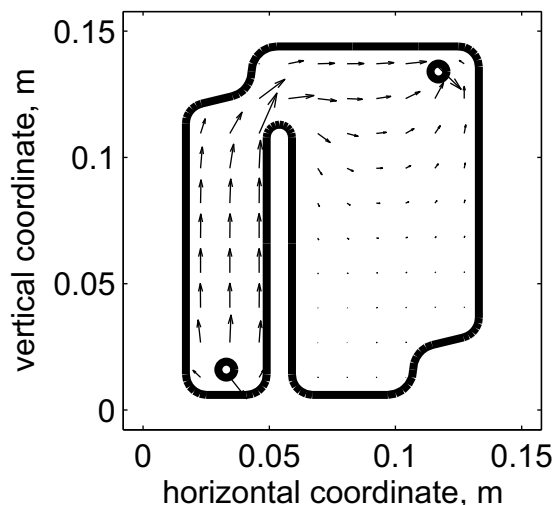
Figure 4.6: Modelled velocity field for the long-fin gasket

Table 4.3: Regressions of measured dimensionless potential against modelled dimensionless potential over the measuring locations (location of error measurement in *Fig.* 4.4 excluded)

gasket shape	gasket thickness (mm)	regression R^2, (%)	regression slope (-)
double-fin	0.2	98.1	0.83
short-fin	0.2	97.9	0.47
no-fin	1.0	94.1	1.04
double-fin	1.0	97.9	1.23
long-fin	1.0	96.4	1.03
short-fin	1.0	64.2	0.62

shows the tracer experiment performed on the long-fin gasket with thickness 1.0 mm and volumetric flow rate 0.17 ml s^{-1} (Reynolds number 10). The tracer first flows past the fin [*Fig* 4.7, (a) and (b)]. After 14 seconds, the flow reaches the top, and the flow spreads over the top region of the geometry. The outlet is reached before the tracer spreads over the dead zone next to the fin [*Fig.* 4.7c]; the sink is reached already in 28 s. Much tracer flows out in a short period, but a small residue travels to the dead zone. The corresponding streamlines have long residence times, in the order of minutes (*Fig.* 4.7d).

The tracer experiments were conducted to validate a model for the residence time distribution, see *Fig.* 4.8. For the no-fin, the double-fin and the long-fin gaskets, the residence time distributions have their maximum at the moment of tracer
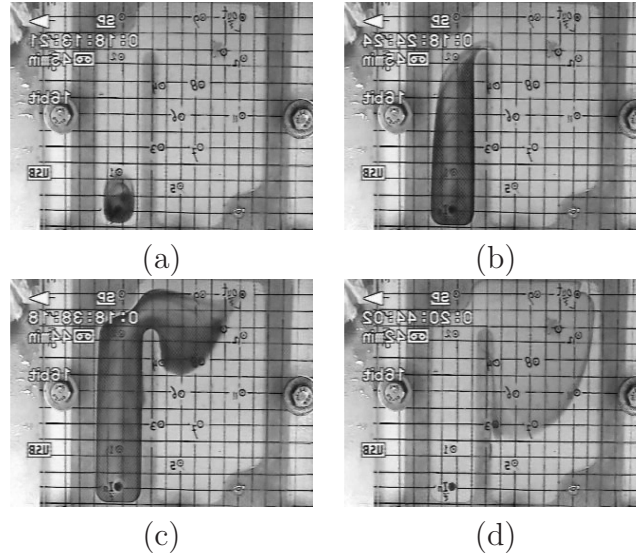
Figure 4.7: Film of tracer experiment with gasket shape long-fin, thickness 1.0 mm and volumetric flow rate 0.17 ml s^{-1}; at 2.8 s (a); at 14 s (b); at 28 s (c); and at 153 s (d)
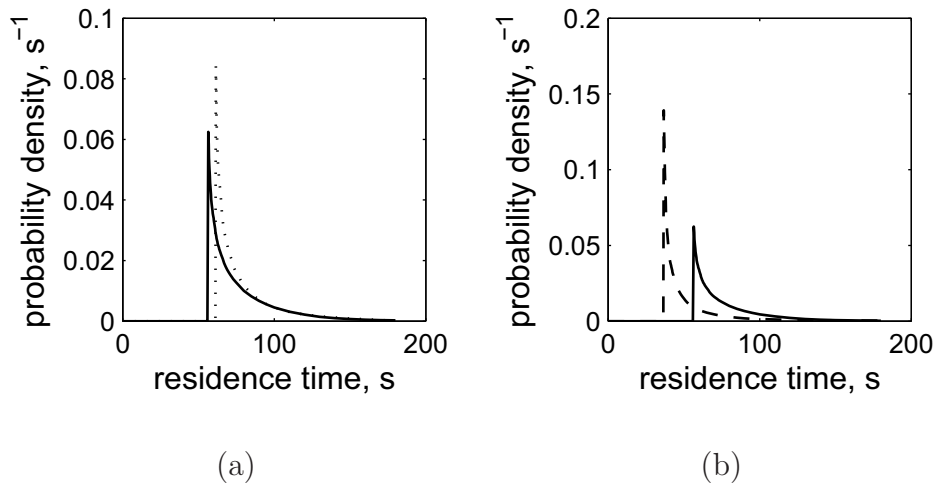

Figure 4.8: Comparison of residence time distributions for the no-fin gasket [solid line in (a) and (b)], with the double-fin gasket [dotted line in (a)] and with the long-fin gasket [dashed line in (b)]; all curves calculated for thickness 1.0 mm and volumetric flow rate 0.17 ml s^{-1}

arrival, which is not expected for the measurements. This feature is a consequence of neglecting diffusion and dispersion in the model.

In the double-fin gasket, a more concentrated residence time distribution was expected than in the no-fin gasket. In the no-fin gasket, the the width of the flow domain varies considerably going from the inlet to the outlet (*Fig.* 4.3a).

However, *Fig.* 4.8a shows that the no-fin gasket and the double-fin gasket have a similar residence time distribution, suggesting that the introduction of fins does not improve the performance of reverse electrodialysis stacks. This result can be explained, because the double-fin gasket introduces extra corners in the domain that act as stagnation points. These stagnation points cause large residence times for the corresponding streamlines.

Surprisingly, the model predicts a more concentrated residence time distribution for the long-fin gasket (*Fig.* 4.8b), which has a large area of stagnant flow. This result can also be explained, because only a small fraction of the flow passes through the stagnant zone. The residence time distribution is dominated by the flow through the left area and the top area, and their combination has less corners than the double-fin gasket.

The model was validated by calculating values for the travelling times to the marked locations, allowing for comparison with the tracer experiments. Log-log regression was applied with the measured travelling times as the dependent variable, and the modelled travelling times as the independent variable. Figure 4.9 shows the regression for the long-fin gasket, thickness 1.0 mm and volumetric flow rate 0.17 ml s^{-1}. Qualitative agreement was demonstrated; the R^2 of the regression was 99.6% (Table 4.4 row 1). There was a systematic error, because the regression line deviated from the diagonal (*Fig.* 4.9). On a short timescale, the model over-estimated the travelling time with a factor of about 3 / 2. This can be explained by the travelling time being determined by the maximal velocity instead of the average velocity (*Eqn.* 4.6). On longer timescales, this effect was reduced, because the measurements were influenced by diffusion in the transversal direction (Gaskell, 1992). The impact of diffusion is also expressed in the slope of the regression line, which is larger than 1 (Table 4.4 row 2).

Table 4.4: Regression of measured travelling times to modelled travelling times

Shape (*Fig.* 4.3)	flow rate (ml s^{-1})	regression R^2	regression slope
no-fin	0.17	99.4	1.10
long-fin	0.17	99.6	1.04
no-fin	8.0	96.6	0.91
long-fin	8.0	73.3	1.09

Table 4.4 summarises the regressions applied for all tracer experiments. Good agreement was observed for the no-fin gasket with 10 ml s^{-1} flow rate (99.4%), and the regression slope was larger than 1 due to diffusion. For higher flows, the model
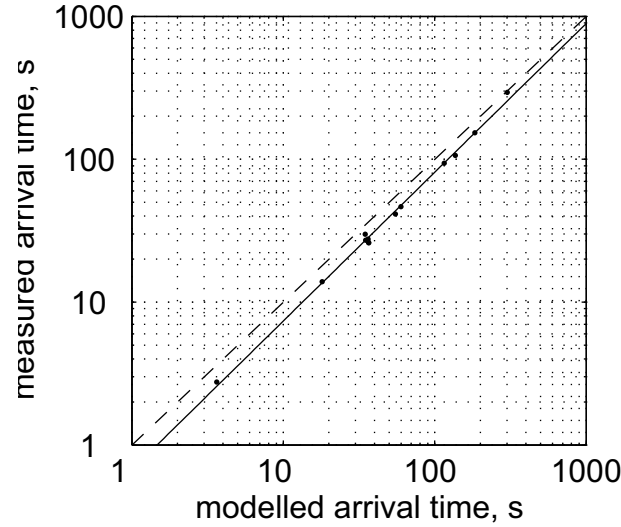
Figure 4.9: Regression of measured travelling time against modelled travelling time for the long-fin gasket with thickness 1.0 mm, and flow rate 0.17 ml s^{-1}; ● is measurement, – = regression line and - - - = diagonal

was less accurate (Table 4.4 rows 3 – 4). For the long-fin gasket, the measurement was disturbed through leakage over the fin, resulting in an R^2-value of only 73%. For the no-fin gasket, the accuracy was a bit less due to the limited accuracy of the time measurement, and because the ink was not perfectly mixed before entry between the plates. These effects were probably more important than the model error caused by neglecting the inertial force for higher Reynolds numbers (about 600 in this case).

4.5 Conclusion

A model based on potential flow theory was developed for the velocity field and the pressure field in flat-sheet geometries. The velocity was modelled to be zero on the membrane surfaces (no-slip condition), introducing transversal velocity gradients. These gradients are handled by introduction of the average velocity, reducing the flow problem to the two dimensions parallel to the membranes. It can be concluded that internal sources and sinks can be modelled by mapping the two-dimensional geometry to the upper half-plane instead of the infinite strip, and by introducing virtual sources and sinks that make the real axis bounding the upper half-plane a line of symmetry.

The model was validated using an experimental setup that measured local pressures, and the two-dimensional geometry, the geometry thickness and the flow rate were changed. The core of the experimental setup was a sheet of transparent foil

(gasket), having the shape of the flow domain cut out. The gasket was fixed between two Perspex plates, allowing the flow to be observed during the experiments. It can be concluded that for each investigated geometry, at least 94% of the variation of the observed pressures is explained by the potential flow model.

Potential flow modelling can be extended to model the residence time distribution. Dispersion and diffusion are neglected, and this assumption implies that each streamline has a fixed residence time. The model predicts the residence time distribution from the variation of the residence times over the different streamlines. The model was applied to compare a system geometry with a large variation of the channel width, to a system geometry with two fins that reduced the variation of the channel width. Surprisingly, both geometries yield similar modelled residence time distributions, which can be explained because the double-fin geometry has corners that introduce stagnation points. It can be concluded that the extended model is a useful tool to compare possible system geometries.

Extended potential flow modelling was also applied to a geometry with a large area of stagnant flow. The residence time distribution for this geometry is more concentrated than the residence time distribution for the double-fin geometry, because only a small fraction of the fluid flows through the stagnant zone. It can be concluded that stagnant zones have a limited impact on the residence time distribution. Extended potential flow modelling can also be used to calculate the travelling time of a fluid particle to a given interior location, allowing for the analysis of spatial variations for the intended chemical reactions (for example electricity production in reverse electrodialysis stacks). It can be concluded that extended potential flow modelling is a useful tool to analyse the efficiency of membrane-based systems.

Chapter 5

Understanding Heat Transfer in 2D Channel Flows Including Recirculation

Notation

B	Baffle width, m
H	Length of flat plate or vertical baffle distance, m
Nu	Nusselt number
P	Denotes a point in two-dimensional space
Pr	Prandtl number
Q	Denotes a point in two-dimensional space
R	Radius of circular vortex, m
Re	Reynolds number
V	Average inflow velocity, $\mathrm{ms^{-1}}$
$\dot{V}$	Two-dimensional volumetric flow rate, $\mathrm{m^2s^{-1}}$
W	Channel width, m
a	Real part of complex derivative of map g, $\mathrm{m^{-1}}$
b	Imaginary part of complex derivative of map g, $\mathrm{m^{-1}}$
g	Conformal map from physical space to unit disc
i	Square root of -1
k	Turbulent kinetic energy, $\mathrm{m^2s^{-2}}$
p	Parameter of regression line
r	Distance from centre in circular vortex, m
u	Horizontal velocity, $\mathrm{ms^{-1}}$
u_∞	Velocity according to irrotational flow theory, $\mathrm{ms^{-1}}$
v	Vertical velocity, $\mathrm{ms^{-1}}$
x	Horizontal coordinate, m
y	Vertical coordinate, m

Greek symbols

ΔT	Temperature difference, K
Φ	Two-dimensional heat flux, $\mathrm{Wm^{-1}}$
γ	Ellipticity
η	Vertical coordinate on unit disc
λ	Thermal conductivity of air, $\mathrm{Wm^{-1}K^{-1}}$
ν	Kinematic viscosity, $\mathrm{m^2s^{-1}}$
ξ	Horizontal coordinate on unit disc
ϕ	Potential function, $\mathrm{m^2s^{-1}}$
ψ	Stream function, $\mathrm{m^2s^{-1}}$
ω	Dissipation of turbulent kinetic energy, $\mathrm{s^{-1}}$

Superscripts

$^{(main)}$	Main flow
$^{(r)}$	Recirculation

(s)	Separation
$(wake)$	Wake

5.1   Introduction

In many engineering problems, the heat flux by convection is of key importance. Given the temperature difference, the heat flux depends on the spatial distribution of velocity and fluid properties. Before the development of digital computers, the heat flux was calculated analytically, based on the most simple approximation of the velocity field: the average velocity (Gaskell, 1992; Perry and Green, 1997). Dimensionless power-law relations are applied in many engineering models. Complicated analytical derivations based on many assumptions are needed to find lumped models (Batchelor, 1967; Gaskell, 1992; Kays and Crawford, 1993; Schlichting, 2000), so lumped models apply to specific systems only.

Two-dimensional flows can be modelled by assuming the flow to be inviscid and irrotational (Batchelor, 1967; Conroy et al., 2000; Hassenpflug, 1998; Trevelyan et al., 2000). Given these assumptions, the velocity field can be calculated using conformal maps. These conformal maps can be calculated using the Schwarz-Christoffel integral (Batchelor, 1967). The necessary calculations have been implemented in software libraries that calculate an entire velocity field within seconds (Driscoll, 1996; Trefethen and Driscoll, 1998). In an earlier publication (Dirkse et al., 2005), we have extended these models to include boundary layer separation and flow recirculation driven by turbulent diffusion. Like any model some unknown parameters have to be calibrated against observations.

Currently, engineers use computational fluid dynamics (CFD) (Patankar, 1980; Wilcox, 1998) to model the heat flux in complicated configurations. Commercial software packages that include the mathematical details are available. The scientific community has established concepts (Oberkampf and Trucano, 2002) and practices (Lacasse et al., 2004; Stern et al., 2001; Wilson et al., 2001) to support reliable modelling. Due to these developments, CFD modelling is relatively easy nowadays, especially if two-dimensional models are applied. During design, many variations of a configuration can be modelled to evaluate their performance. However, computational fluid dynamics models give much more information than required for engineering decisions. Secondly, CFD models are too slow to be used as parts of larger engineering models (Gullapalli et al., 2005); and much too slow for implementation in automatic controllers. These two aspects demonstrate a need for simple tools to analyse flow phenomena.

This article focusses on turbulent two-dimensional flows including flow recircula-

tion, with our earlier publication (Dirkse et al., 2005) on this subject as the starting point. The Schwarz-Christoffel model has unknown parameters, which are actually geometric characteristics of the velocity field. These characteristics describe the flow field as a combination of channel flow and recirculation wakes. We investigate whether this description is accurate, and whether the characteristics are useful for further model development. To do this, the Schwarz-Christoffel model is calibrated against known velocity fields. The parameters (geometric characteristics) are included in lumped models for the heat flux. It is examined (a) whether these models are accurate; (b) whether these models outperform conventional Nusselt-Reynolds correlations; and (c) whether the Schwarz-Christoffel model can be calibrated against real velocity measurements. The method is demonstrated for channel flow with baffles as an example for main flow and recirculation combination.

5.2 Theory

5.2.1 Irrotational flow

Since many technically important fluids have low viscosities (e.g. air or water), the majority of flows in practice are flows with high Reynolds number (Schlichting, 2000). For these cases, viscous forces can be neglected compared to inertial forces nearly all over the flow field (Batchelor, 1967). If the flow is also irrotational (Batchelor, 1967), it can be modelled by introducing the potential function ϕ (m^{2}s^{-1}) and the stream function ψ (m^{2}s^{-1}) (Batchelor, 1967). When u and v are the components of the 2D velocity vector (ms^{-1}), the potential function is defined to have $(u, v)'$ as its gradient; and the gradient of the stream function is defined to be $(-v, u)'$ (Batchelor, 1967). When P and Q are two arbitrary locations in two-dimensional space, the difference $\psi(P) - \psi(Q)$ is the 2D volumetric flow rate (m^{2}s^{-1}) through any curve joining P and Q (Batchelor, 1967). The assumption of inviscid and irrotational flow makes the complex potential, defined as $\phi + i\psi$, an analytic function of space (Batchelor, 1967).

The complex potential can be used to calculate the entire velocity field in bounded infinite channels. The model inputs are the channel geometry and the 2D volumetric flow rate $\dot{V}$ (m^{2}s^{-1}). By mass conservation, the stream function ψ is constant on both channel walls: $\psi = 0$ on one wall, $\psi = \dot{V}$ on the other. These conditions suffice to define a unique solution for the complex potential, which is calculated by mapping the channel onto the infinite strip. If the channel has a polygonal shape, the calculation can be performed using the Schwarz-Christoffel integral (Batchelor, 1967). Software libraries have become available that evaluate the Schwarz-Christoffel integral numerically (Driscoll, 1996; Trefethen and Driscoll, 1998). Driscoll (Driscoll, 1996) has programmed such a library for MatLab (the Math Works, 2006).

The velocity calculated by irrotational flow theory can be used to model the heat flux (Kays and Crawford, 1993). The following Nusselt-Reynolds correlation applies to turbulent flow past a flat plate if it is heated from the start, and if the velocity according to irrotational flow theory u_∞ (ms^{-1}) is constant (Ameel, 1997; Kays and Crawford, 1993):

$$Nu = \frac{\Phi}{\lambda \Delta T} = 0.0359 \, Pr^{0.6} \left(\frac{H u_\infty}{\nu} \right)^{0.8} \tag{5.1}$$

with: Φ the 2D heat flux (Wm^{-1}), λ the thermal conductivity (Wm^{-1}K^{-1}), ΔT the temperature difference (K), Pr the Prandtl number, H the length of the plate (m), and ν the kinematic viscosity m^{2}s^{-1}.

5.2.2   Recirculation flow

The velocity field as calculated by irrotational flow theory does not satisfy the no-slip boundary condition. Indeed, thin areas with high velocity gradients are formed near solid walls, called boundary layers, where viscous effects are important. In some cases, a boundary layer separates from the wall where it is formed (Abu-Mulaweh, 2005; Batchelor, 1967; Kays and Crawford, 1993; Schlichting, 2000). At the separation point, small vortices are convected into the bulk flow (Batchelor, 1967), which form a thin layer if the Reynolds number is high. This layer is called a vortex sheet (Batchelor, 1967; Saffman, 1992). If the area behind the vortex sheet is bounded, turbulent momentum transport (Schlichting, 2000) through the vortex sheet causes recirculation flow.

Many researchers have proposed models for unbounded two-dimensional vortices (Batchelor, 1967; Paterson, 1983; Saffman, 1992; Satijn et al., 2004). A common model for monopolar unbounded vortices (Satijn et al., 2004), Rankine's model, defines the velocity field via the stream function ψ (Batchelor, 1967):

$$\psi = \psi^{(r)} \left(1 - \frac{r^2}{R^2} \right) \tag{5.2}$$

where $\psi^{(r)}$ is the 2D recirculation flow rate (m^{2}s^{-1}); R is the fixed radius of the vortex (m); and r is the variable distance from the vortex centre (m). The velocity follows from differentiating *Eqn.* (5.2).

Our earlier publication (Dirkse et al., 2005) develops a model for bounded two-dimensional vortices, which is part of the Schwarz-Christoffel model. As to our knowledge, we are the first to propose this model for bounded vortices. The model is inspired by Rankine's vortex model (*Eqn.* 5.2). Using the Schwarz-Christoffel integral, the vortex is mapped to the unit disc having coordinates ξ and η. The boundary of the vortex has become a circle, which allows us to introduce an equation

for the stream function:

$$\psi = \psi^{(r)}(1 - \xi^2 - \eta^2) \tag{5.3}$$

This equation introduces the recirculation flow rate $\psi^{(r)}$ ($\mathrm{m}^2\mathrm{s}^{-1}$) as a parameter. Given the map to the unit disc, *Eqn.* (5.3) defines the stream function everywhere in the vortex; and the velocity field can be evaluated by differentiating *Eqn.* (5.3).

Now, the map from the vortex to the unit disc must be specified. We start from the following assumptions: (a) the boundary of the vortex can be approximated by a polygon; and (b) the streamlines near the vortex centre look like ellipses. Furthermore, the model is applied to elongated vortex areas. For this reason, we have assumed also that: (c) the main axis of the ellipses of the recirculation is parallel to the vertical axis y. Assumption (b) does not specify the eccentricity of the ellipses (x-axis / y-axis). This eccentricity is introduced as a second parameter, $\gamma^{(r)}$.

To map a given location to the unit disc, we first multiply the vertical coordinate with the eccentricity. According to the assumptions, this transforms the elliptical streamlines into circles. A conformal map is applied to map these circular streamlines to the unit disc. Conformal maps are analytic complex functions (Batchelor, 1967; Keener, 1988), so the required map g can be evaluated using the Schwarz-Christoffel integral (Driscoll, 1996; Trefethen and Driscoll, 1998). To define g uniquely, the coordinates of the vortex center must be introduced as parameters (Driscoll, 1996): $x^{(r)}$ and $y^{(r)}$ (m).

The above is summarised by the equation $(\xi, \eta) = g(x, \gamma^{(r)}y)$. Combining this with *Eqn.* (5.3) and differentiating yields:

$$\left(\frac{\partial \psi}{\partial x}, \frac{\partial \psi}{\partial y} \right) = (-v, u) = \psi^{(r)} \begin{pmatrix} -2\xi & -2\eta \end{pmatrix} \begin{pmatrix} a & -b \\ b & a \end{pmatrix} \begin{pmatrix} 1 & 0 \\ 0 & \gamma^{(r)} \end{pmatrix} \tag{5.4}$$

where $a + bi$ is the complex derivative of g; a and b are in m^{-1}. The model has four unknown parameters: The 2D recirculation flow rate $\psi^{(r)}$, the coordinates of the vortex centre $(x^{(r)}, y^{(r)})$, and the eccentricity $\gamma^{(r)}$. These four parameters are geometric characteristics, so four geometric characteristics can describe a monopolar vortex with a given boundary.

5.3 Materials and methods

5.3.1 Modelling the velocity field

The Schwarz-Christoffel model in general calculates the velocity field from the volumetric flow rate $\dot{V}$ and the shape of the flow domain. For this article, we considered a typical main flow and recirculation combination: Consecutive chambers
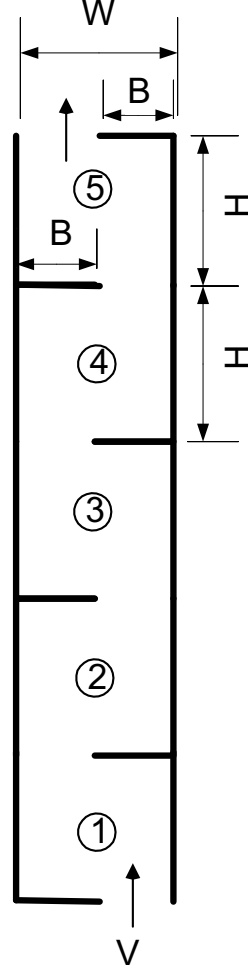
Figure 5.1: Modelled configurations with design parameters H (m), W (m) and B (m); and with average inflow velocity V (ms^{-1}); the chambers are numbered

of a vertical channel including alternating baffles (*Fig.* 5.1), with the chamber defined as the area enclosed by two baffles. The design parameters are: Vertical baffle distance H (m); channel width W (m); and baffle width B (m). All channels examined were variations of the default defined by $H = 1.00$ m, $W = 0.40$ m, $B = 0.20$ m (Table 5.1 row 1). The channels contained air flowing from the bottom to the top, and for every channel the following values for the average inflow velocity V (ms^{-1}) were examined: 1.0, 2.0, 5.0, 10.0 and 25 ms^{-1}. These design parameters were chosen to make the flow turbulent (Gaskell, 1992): The Reynolds number VH/ν (ν is kinematic viscosity of air, m^{2}s^{-1}) ranged from $6.8 \, 10^3$ to $3.4 \, 10^6$.

The Schwarz-Christoffel model had to be calibrated against given velocity fields, in this case generated by computational fluid dynamics (CFD) modelling. Six geometries (Table 5.1) and five velocities were modelled, resulting in 30 cases. The

Table 5.1: Design parameters H, W and B (*Fig.* 5.1) of the examined channels

channel design number (-)	vertical baffle distance H (m)	channel width W (m)	baffle width B (m)
1	1.00	0.400	0.200
2	1.50	0.400	0.200
3	2.00	0.400	0.200
4	1.00	0.400	0.100
5	1.00	0.400	0.150
6	0.10	0.040	0.020

CFD cases were very similar to the one used in (Dirkse et al., 2005). The velocity and the pressure were solved from the incompressible steady Navier-Stokes equations (Batchelor, 1967), and the density and the viscosity of air were assumed to be temperature independent. The velocity was assumed to be uniform at the inflow opening at the bottom. The no-slip boundary condition was applied for the walls, and an outflow boundary condition at the top. The equations were solved using the commercial code Fluent (Fluent Inc., 2007).

The CFD cases used the k-ω turbulence model (Wilcox, 1998). The boundary condition at the bottom for k and ω was expressed via the turbulence intensity (Dirkse et al., 2005; Fluent Inc., 2007; Kays and Crawford, 1993): the time-averaged magnitude of the fluctuating velocity (Wilcox, 1998) relative to the average inflow velocity V. The turbulence intensity at the bottom was set to 10%. A rectangular grid was used, which was generated using the commercial code Gambit (Fluent Inc., 2007). To resolve the boundary layers, the grid intervals perpendicular to the channel walls had to be very small: 10^{-5} m. Dynamic grid adaption was applied to resolve the vortex sheets (Lacasse et al., 2004), and multiple refinement levels were compared to verify grid convergence (Lacasse et al., 2004; Oberkampf and Trucano, 2002).

The CFD velocity fields were calculated in a channel as depicted in *Fig.* 5.1, and the chambers in a channel were examined separately. Chamber number 1 and chamber number 5 (*Fig.* 5.1) were discarded, because the boundary conditions were very crude: parallel inflow at the bottom and an outflow boundary condition at the top. Therefore, each of the 30 CFD cases produced the velocity field in 3 chambers, resulting in 90 realisations of the velocity field. A realisation can be identified by the vertical baffle distance H, the channel width W, the baffle width B, the average inflow velocity V, and the chamber number (*Fig.* 5.1).

A realisation of the velocity field constituted local velocities in tens of thousands

of mesh cells, so this data was transformed to make it useful for calibration. The velocity field was truncated using a grid of 30×30 regularly arranged locations. For every location, the mesh cell closest to the location was selected, reducing the number of velocity vectors to 900. Figure 5.1 shows that the even numbered chambers were reflected compared to the odd numbered chambers. When the realisation had an even chamber number, it was reflected by a coordinate transformation that replaced the x-coordinate with $W - x$. The result of these two transformations is called a calibration set, so there was one calibration set for each of the 90 realisations.

Since 900 local velocities cannot be measured, a virtual measurement set was derived from a calibration set. The virtual measurement set was based on 3×3 regularly arranged locations. For every location, the nearest velocity vector in the calibration set was selected. To save calculation time, virtual measurement sets were created only for the 15 (3 chamber numbers times 5 average inflow velocities) realisations corresponding to the default channel geometry (Table 5.1, number 1).

In previous research, the stream function has been calculated using CFD modelling, see *Fig.* 5.2. By definition of stream function (Subsection 5.2.1) and by
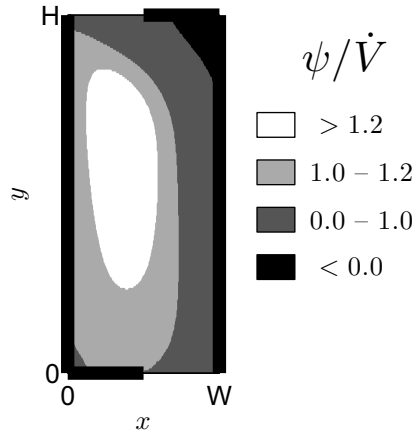

Figure 5.2: Contour plot of stream function ψ (m²s⁻¹), calculated using computational fluid dynamics modelling; $\dot{V}$ is 2D volumetric air flow rate (m²s⁻¹); copied from (Dirkse et al., 2005)

mass conservation, the stream function on the main flow area must range from 0 to $\dot{V}$. The areas with stream function values outside this range must therefore correspond to recirculation areas. These areas are located at the top right and towards the left. The lines $\psi = 0$ and $\psi = \dot{V}$ correspond to areas of high vorticity (not shown). This observation confirms that separated boundary layers give rise to vortex sheets.

The Schwarz-Christoffel model approximates the vortex sheets by straight line segments, introducing vertices in the model of which the coordinates are parameters (free separation vertices) (*Fig.* 5.3). The chamber is extended to infinity by vertical
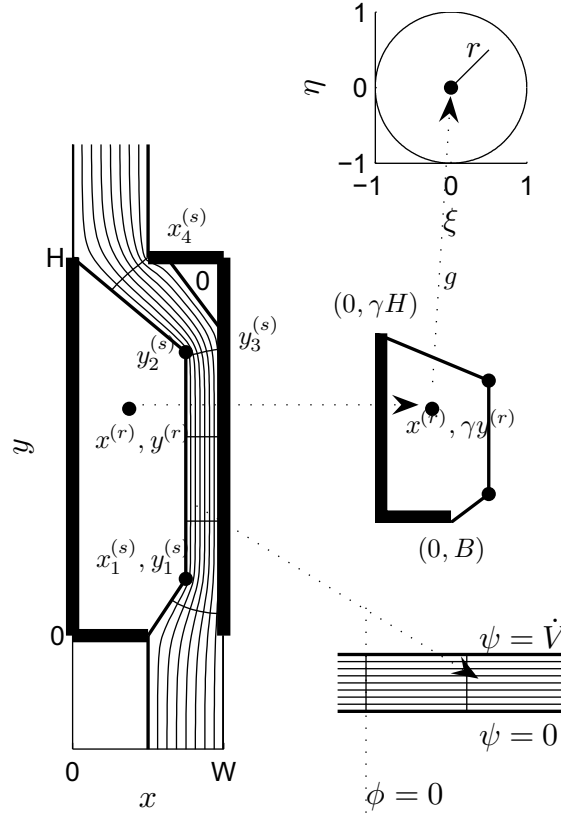

Figure 5.3: Illustration of Schwarz-Christoffel model and its parameters

line segments (*Fig.* 5.3). Irrotational flow is assumed over the area between the approximated streamlines $\psi = 0$ and $\psi = \dot{V}$, so this area is modelled by mapping it to the infinite strip (Subsection 5.2.1). The wake is modelled as a monopolar vortex using *Eqn.* (5.4), and the top-right recirculation area is modelled to have zero velocity.

Now, symbols are introduced for all parameters that characterise a velocity field (*Fig.* 5.3). The first separation vertex at the left vortex sheet is named $(x_1^{(s)}, y_1^{(s)})$. The y-coordinate of the second separation vertex to the left is named $y_2^{(s)}$ and its x-coordinate is always taken to be $x_1^{(s)}$ to minimise the number of parameters. The coordinates describing the right vortex sheet are named $y_3^{(s)}$ and $x_4^{(s)}$. The four parameters describing the wake are the coordinates of the vortex centre $(x^{(r)}, y^{(r)})$, the recirculation flow rate $\psi^{(r)}$, and the eccentricity $\gamma^{(r)}$.

The algorithm that calculates the model parameters starts from a given calibration set or virtual measurement set. Parameter values are optimised such that

minimisation of the difference between the velocity field according to the Schwarz-Christoffel model, and the velocity field in the calibration set, *i.e.* the global velocity error, is achieved. The global velocity error is the root-mean-square of the local velocity errors at the locations in the calibration set. The local velocity error is the norm of the vector that contains the error of the horizontal velocity and the error of the vertical velocity. The Schwarz-Christoffel integral has singularities at vertices having an internal angle of more than 180° [e.g. $(x_1^{(s)}, y_1^{(s)})$ in *Fig.* 5.3], so it makes no sense to observe the local velocity error there. The global velocity error is iteratively minimised by Sequential Quadratic Programming (SQP) (Schittowski, 1985). Ten different random initialisations are applied and the parameter values corresponding to the lowest velocity error are selected. The ten runs of SQP can be compared to obtain error estimates for each parameter separately.

To examine the relevance of each model parameter, calibration was performed using different subsets of the parameters. Leaving out $y_3^{(s)}$ and $x_4^{(s)}$, for example, implied that boundary layer separation at the top-right was not included in the model. All subsets were calibrated against the same calibration set, and the corresponding velocity errors were compared. Based on this comparison, we selected the parameters that were relevant to describe a velocity field. Different velocity fields generally correspond to different values of the parameters, so the relevant parameters were expected to be different for every calibration set.

The selected parameters were calculated for all realisations, resulting in 90 realisations for every parameter. Each parameter was made dimensionless and its mean and variation (root-mean-square of deviations from the mean) were calculated. A parameter was assumed constant if its variation was low compared to the accuracy of the calibration algorithm, allowing for a reduction of the number of parameters needed. The variable parameters were recalculated to test the impact of making parameters constant.

To analyse the variable parameters, the modelled realisations were divided into six groups that corresponded to the six channel geometries (Table 5.1). Each modelled geometry constituted 15 realisations, which corresponded to 15 realisations of each variable parameter. The mean of a parameter over these realisations is referred to as a geometry mean. The impact of velocity and chamber number on a parameter was assessed using its range (over 15 parameter realisations).

The variable parameters were also calibrated against the virtual measurement sets to examine whether these parameters can be measured. The virtual measurements of the parameters were analysed by relating them to the parameter realisations obtained using the large calibration sets, the calibrated values. For every variable parameter, a linear regression model was created that explained the 15 (only one modelled geometry) virtual measurements from the calibrated values. The R^2-value of the

regression, the percentage of variance explained by the regression model, was used as a measure for the agreement of the virtual measurements.

5.3.2   Lumped models for heat transfer

The main objective of this paper is modelling heat transfer, so the CFD models of Subsection 5.3.1 were extended to include heat transfer. The channel walls were modelled to have a constant temperature, which was 10 K higher than the temperature of the incoming air. Buoyancy effects could be neglected for the chosen design parameters (Batchelor, 1967), so it was only needed to solve the energy equation extra to the existing solution of the Navier-Stokes equations. The heat fluxes from the two walls of every chamber (*Fig.* 5.1) were considered separately, because *Eqn.* (5.1) is valid for the heat flux from the wall next to the main flow area ($\Phi^{(main)}$, Wm^{-1}), but not for the wall next to the wake ($\Phi^{(wake)}$).

The CFD $\Phi^{(main)}$ and $\Phi^{(wake)}$ were analysed taking into account that the air was heated in preceeding chambers, so $\Delta T^{(main)}$ was defined as the temperature difference between the chamber inflow and the walls. $\Phi^{(wake)}$ was analysed using the conditions in the wake only, so $\Delta T^{(wake)}$ was defined as the temperature difference between the wall and the vortex centre. Using these temperature differences, the following Nusselt numbers were defined:

$$Nu^{(main)} = \frac{\Phi^{(main)}}{\lambda \Delta T^{(main)}} \qquad Nu^{(wake)} = \frac{\Phi^{(wake)}}{\lambda \Delta T^{(wake)}} \qquad (5.5)$$

where λ is the thermal conductivity of air ($\mathrm{Wm}^{-1}\mathrm{K}^{-1}$).

Without information about the velocity field, a power law model for $Nu^{(main)}$ is generally assumed:

$$Nu^{(main)} \;=\; p_1 \, Re^{p_2} \qquad (5.6)$$
$$Re \;=\; V\,H/\nu \qquad (5.7)$$

where p_1 and p_2 are parameters to be determined by linear regression. The regression error could be transformed to a relative error for $Nu^{(main)}$, because $\log Nu^{(main)}$ was used to draw the regression line. The variable parameters of the Schwarz-Christoffel model were used to define modified Reynolds numbers, which were also used to model $Nu^{(main)}$. In this way, the relevance of the Schwarz-Christoffel model parameters for the heat flux could be investigated. The same procedure was applied to model $Nu^{(wake)}$: $Nu^{(wake)}$ was first modelled using Re (*Eqn.* 5.7), and modified Reynolds numbers based on the Schwarz-Christoffel model parameters were used after that.

Finally, a power law model for the total heat flux $\Phi^{(main)} + \Phi^{(wake)}$ was created for reference. The total heat flux was modelled using the total Nusselt number defined

by:

$$Nu^{(tot)} = \frac{\Phi^{(main)} + \Phi^{(wake)}}{\lambda \Delta T^{(main)}} \tag{5.8}$$

and $Nu^{(tot)}$ was related to the standard Reynolds number Re.

5.4 Results and discussion

5.4.1 Selection of parameters

A velocity field calculated with CFD, as shown in *Fig.* 5.4a, was used to calibrate the Schwarz-Christoffel model including different numbers of parameters. When no parameters were included, the Schwarz-Christoffel model mapped the entire flow domain to the strip. The velocity field was not modelled correctly in this case as demonstrated in *Fig.* 5.4b. The root-mean-square of the local errors over the 900 locations in the calibration set was 88% relative to the average inflow velocity (Table 5.2, first line).
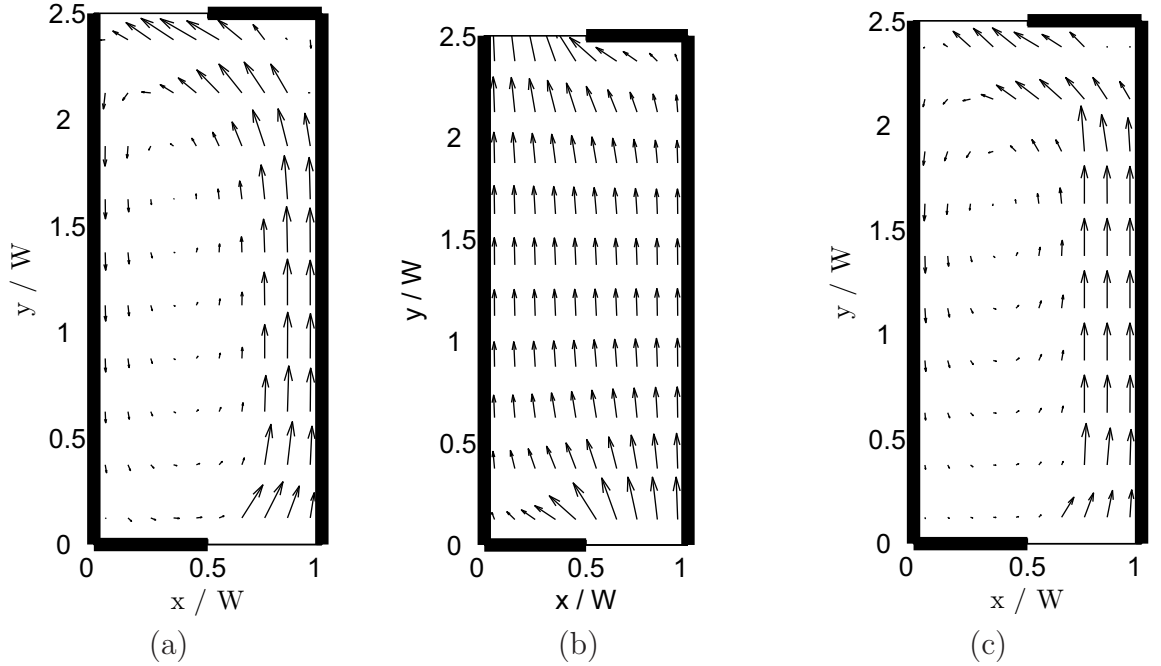
Figure 5.4: Qualitative agreement between CFD model and Schwarz-Christoffel model for $H = 1.0$ m, $W = 0.40$ m, $B = 0.20$ m, $V = 5.0$ ms^{-1} and chamber number 3; (a) CFD model; (b) Schwarz-Christoffel model without boundary layer separation (Table 5.2, first row); (c) Schwarz-Christoffel model using nine parameters (Table 5.2, last row)

With one free separation vertex and a circular wake, five parameters were used, which resulted in a large reduction of the error to 42% (Table 5.2, third line). The most efficient way to add the sixth parameter was to introduce a second separation

Table 5.2: Velocity errors resulting from different parameter selections relative to CFD model results; calibration for $H = 1.0$ m, $W = 0.40$ m, $B = 0.20$ m, $V = 5.0$ ms^{-1}, chamber number 3

left vortex sheet	right vortex sheet	left num. sep. vertices	left recirc. type	number of parameters	relative velocity error
no	no	-	-	0	88
yes	no	1	zero	2	58
yes	no	1	circular	5	42
yes	no	1	elliptic	6	40
yes	no	2	circular	6	32
yes	yes	1	circular	7	41
yes	no	2	elliptic	7	28
yes	yes	1	elliptic	8	38
yes	yes	2	elliptic	9	24

vertex (reduction to 32% error). Making the recirculation elliptic after this reduced the error by 4% to 28%, requiring seven parameters. This reduction verified the importance of the ellipticity parameter stated in (Dirkse et al., 2005). When all parameters of Subsection 5.3.1, nine parameters, were used, the error was 24%. This parameter selection made the Schwarz-Christoffel model agree with the CFD model as shown in *Fig.* 5.4c: large velocities on the right, smaller velocities on the left, recirculation behind the lower baffle and very small velocities at the lower-left corner.

The nine parameters were calibrated for a total of 90 realisations (6 channel geometries times 5 velocities times 3 chamber numbers: 2, 3 and 4, see *Fig.* 5.1). The velocity error of 24% listed in Table 5.2, was typical the velocity error calculated for all modelled realisations, because the average of these errors was 22% and their standard deviation was 4%. For each channel geometry, the velocity error increased for increasing chamber number (*Fig.* 5.1), and this effect was significant according to a t-test. This effect was related to an increase of the local velocities in the recirculation areas, making these areas more important compared to the main flow area. The velocity error was also high for low Reynolds numbers (geometry 6 of Table 5.1); up to 35% for chamber number 3 and average inflow velocity $V = 1.0$ ms^{-1} (corresponding Reynolds number $6.8\,10^3$). This large velocity error was caused by deviating vorticity fields according to the CFD models, as demonstrated in *Fig.* 5.5. For instance the vorticity field for $Re = 6.8\,10^3$ deviates considerably from the vorticity fields for higher Reynolds numbers as can be seen in *Fig.* 5.5.

Over the 90 realisations, the standard deviation of the dimensionless parameter $y_1^{(s)}/H$ (see *Fig.* 5.3 for meaning of $y_1^{(s)}$) was 0.07. The error of the calibration algorithm for $y_1^{(s)}/H$, estimated using the ten runs of Sequential Quadratic Program-

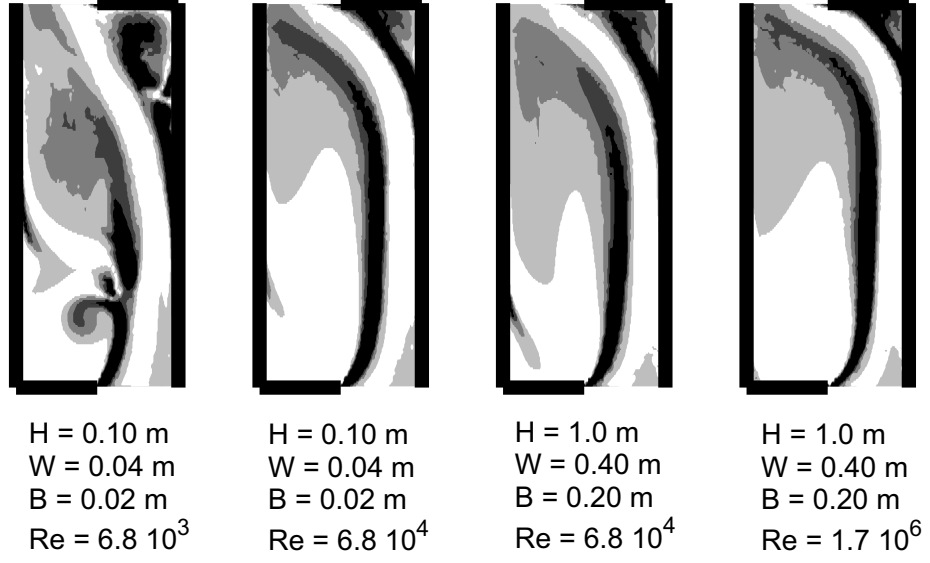| H = 0.10 m | H = 0.10 m | H = 1.0 m | H = 1.0 m |
W = 0.04 m	W = 0.04 m	W = 0.40 m	W = 0.40 m
B = 0.02 m	B = 0.02 m	B = 0.20 m	B = 0.20 m
Re = 6.8 10^3	Re = 6.8 10^4	Re = 6.8 10^4	Re = 1.7 10^6

Figure 5.5:   CFD calculated contour plots of vorticity magnitude for different Reynolds numbers

ming (Subsection 5.3.1), was 0.08. These numbers demonstrated that the variation of $y_1^{(s)}/H$ was fully explained by the error of the calibration algorithm. Therefore, $y_1^{(s)}/H$ was assumed constant, and the constant value was the mean over the 90 realisations: $y_1^{(s)}/H = 0.14$. The same applied for two other parameters, resulting in the constant values $y_3^{(s)}/H = 0.78$ and $y^{(r)}/H = 0.61$. Three additional parameters had part of their variation explained by the error of the calibration algorithm, and the following constant values were assumed: $\gamma^{(r)}H/B = 2.33$, $x_4^{(s)}/W = 0.77$ and $y_2^{(s)}/H = 0.73$. The remaining variable parameters were $x_1^{(s)}/W$, $x^{(r)}/W$ and $\psi^{(r)}/\dot{V}$. Their values were recalculated using the constant parameter values listed above, and this calculation was performed for every realisation.

Using three instead of nine parameters caused only a small increment of the relative velocity error. For the chamber of *Fig.* 5.4, the error remained 24% (Table 5.2, last row). The error increased only two percent averaged (root-mean-square) over the fifteen realisations having the default geometry (Table 5.1 number 1). The averaged error increments were below 4% for geometry numbers 2 – 5 of Table 5.1. The highest average increment, 5%, was found for low Reynolds numbers (Table 5.1 number 6), and this value is explained by deviating vorticity fields as calculated by CFD modelling (*Fig.* 5.5).

To analyse the values for the variable parameters, the 15 realisations corresponding to the default geometry are considered first. The geometry mean of $x_1^{(s)}/W$

was 0.71 (Table 5.3, first row), so the width of the wake was more than the baffle

Table 5.3:   Statistics of variable parameters over default modelled geometry (15 realisations per parameter); geometry means and parameter domains (first three rows), and agreement of virtual measurements (last row)

	relative wake width $x_1^{(s)}/W$	relative wake centre $x^{(r)}/W$	relative recirculation flow rate $\psi^{(r)}/\dot{V}$
channel mean	0.71	0.37	0.34
minimum	0.65	0.35	0.26
maximum	0.77	0.40	0.42
agreement virt. measurements (%)	95	69	81

width B ($B/W = 0.5$, see Table 5.1). This number also demonstrated that the main flow was contracted. The geometry mean of $x^{(r)}/W$ was about half the mean of $x_1^{(s)}/W$ (Table 5.3, first row), which meant that the vortex centre was located in the horizontal middle of the wake. Vertically, the vortex centre was located towards the top, because the $y^{(r)}/H = 0.61$ constant parameter was more than 0.50. The ranges of the dimensionless parameters were small compared to the geometry means (Table 5.3, second and third row).

The channel geometries numbered 2 and 3 in Table 5.1 differed from the default channel geometry only by the vertical baffle distance H. The channel geometries numbered 4 and 5 differed only by the baffle width B, and geometry number 6 was scaled to model lower Reynolds numbers. The impact of geometry on the parameter values was analysed by comparing the geometry means for the different geometries with the default geometry. It appeared that increasing the baffle width widened the wake, increasing the flow rate in the wake as well (Table 5.4, second column). Increasing the vertical baffle distance H moved the vortex centre to the right and reduced the wake width and the flow rate in the wake (Table 5.4, first column). Increasing the Reynolds number widened the wake and increased the recirculation flow rate, but had no impact on the location of the vortex centre.

To examine whether the variable parameters can be measured, the calibration algorithm was applied on reduced calibration sets, called virtual measurement sets (3 × 3 regularly arranged velocity vectors). The virtual measurements of the parameters were analysed by comparing them with the parameter realisations obtained using the large calibration sets. The parameter $x^{(r)}/W$ could be measured the least accurate, because the agreement (R^2-value of the regression) was 69%. The parameters $\psi^{(r)}/\dot{V}$ and $x_1^{(s)}/W$ could be measured satisfactory (81% resp. 95% agreement).

Table 5.4:   Influence of geometry on Schwarz-Christoffel model parameters; + = positive correlation and − = negative correlation and 0 = the difference between the relevant geometry means was not significant according to a t-test with significance level 5%

| | Design parameter | | |
dimensionless model parameter	chamber height H	baffle width B	Reynolds number
relative wake width $x_1^{(s)}/W$	−	+	+
relative wake centre $x^{(r)}/W$	+	+	0
relative recirculation flow rate $\psi^{(r)}/\dot{V}$	−	+	+

5.4.2   Use of Schwarz-Christoffel parameters to model heat transfer

The Schwarz-Christoffel model parameters were used to model heat transfer. Figure 5.6 shows a typical temperature field obtained by CFD modelling, for chamber
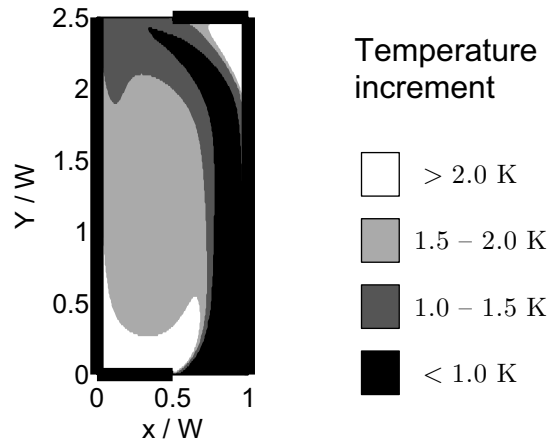

Figure 5.6:   Temperature field according to CFD model; $H = 1.0$ m, $W = 0.40$ m, $B = 0.20$ m, $V = 5.0$ ms^{-1}, chamber number 3; the channel walls are 10 K warmer than the channel inflow temperature

number 3; the walls are 10 K warmer than the channel inflow temperature. There was a temperature increment of less than 1 K at the chamber inflow opening, because the air was heated in the two preceeding chambers. The air temperature did not increase much in the main flow area, but the temperature was higher in the wake and in the recirculation area at the top-right. These higher temperature increments

were explained by the longer contact times between the air and the walls there. The temperature in the wake was rather homogeneous as well, justifying that a wake temperature was defined (Subsection 5.3.2). The 2D heat flux corresponding to *Fig.* 5.6 was 561 Wm^{-1}, which was represented by a Nusselt number of 1250. The Nusselt numbers corresponding to all realisations ranged from 44 to 7900, and they could be modelled using the standard Reynolds number (*Eqn.* 5.7) with an error of 17% (Table 5.5, number 1).

Table 5.5: Nusselt-Reynolds correlations modelling the total heat flux, the main heat flux and the wake heat flux using relevant modified Reynolds numbers; H, W and B design parameters (*Fig.* 5.1), V is average inflow velocity, $\dot{V}$ is volumetric flow rate ($\mathrm{m}^2\mathrm{s}^{-1}$), ν kinematic viscosity ($\mathrm{m}^2\mathrm{s}^{-1}$)

Seq. number	Side	Reynolds	Power-law (*Eqn.* 5.6)		Relative error
			p_1	p_2	
1	total	HV/ν	0.041	0.80	17
2	main	HV/ν	0.043	0.81	22
3	main	$H\dot{V}/\nu(W - x_1^{(s)})$	0.041	0.79	11
4	wake	BV/ν	0.201	0.79	20
5	wake	HV/ν	0.075	0.75	12
6	wake	$(x^{(r)}/B)(HV/\nu)$	0.111	0.72	17
7	wake	$(x_1^{(s)}/B)(HV/\nu)$	0.072	0.73	15
8	wake	$(\psi^{(r)}/B)H/\nu$	0.214	0.73	12
9	wake	$H\psi^{(r)}/x^{(r)}\nu$	0.151	0.75	9
10	wake	$H\psi^{(r)}/x_1^{(s)}\nu$	0.225	0.75	7

Improved relations for the main and wake heat fluxes were found by analysing them separately (Subsection 5.3.2). The main flow area is described by $x_1^{(s)}$, $y^{(1)}$, $y^{(2)}$, $y_3^{(s)}$ and $x_4^{(s)}$ (*Fig.* 5.3). From this list, only $x_1^{(s)}$ is variable and hence is relevant to be included in modified Reynolds numbers. This parameter was used to model the width of the main flow, defining a new characteristic velocity. The characteristic length in the modified Reynolds number remained the chamber height H, keeping the analogy with a flat plate. The modified Reynolds number predicted $\Phi^{(main)}$ better than the standard Reynolds number (Table 5.5 numbers 2 and 3): the error reduced from 22% to 11%.

The main heat flux was also modelled using the virtually measured values of $x_1^{(s)}$, obtained from calibration with the reduced calibration sets as reference. These parameter values were only calculated for the default modelled channel. Using only the standard geometry instead of all geometries, the relative error for the standard Reynolds number reduced from 22% (Table 5.5) to 17% (Table 5.6 row 1). The

Table 5.6: Relative errors of regression models for the main heat flux and the wake heat flux, based on virtual measurements and calibrated parameter values; regression only over default modelled geometry (15 realisations)

1	main	–	$H V/\nu$	17
2	main	calibrated	$H\dot{V}/\nu(W - x_1^{(s)})$	5.1
3	main	measured	$H\dot{V}/\nu(W - x_1^{(s)})$	5.8
4	wake	–	$V H/\nu$	9
5	wake	calibrated	$H\psi^{(r)}/x_1^{(s)}\nu$	2.9
6	wake	measured	$H\psi^{(r)}/x_1^{(s)}\nu$	5.3

modified Reynolds number, containing the wake width $x_1^{(s)}$, allowed the heat flux to be modelled much more accurately. Based on the virtual measurements, the error was only 5.8% (Table 5.6 row 3). Based on the parameter values obtained from the large calibration sets, the error was not much lower: 5.1% (Table 5.6 row 2). These results demonstrate that the main heat flux can also be calculated using parameter values obtained from a small number of measured velocities.

The wake heat flux was first modelled without model parameters. Using the baffle width B as the characteristic length yielded 20% error (Table 5.5 number 4), but using the vertical baffle distance H yielded 12% (Table 5.5 number 5). Secondly, one model parameter was included in the Reynolds number in such a way that the characteristic length remained the vertical baffle distance (Table 5.5 numbers 6 – 8). The best parameter to include appeared to be the recirculation flow rate $\psi^{(r)}$, resulting in an error of 12%. The corresponding Reynolds number was $(\psi^{(r)}/B)H/\nu$, so the area containing the recirculation flow was characterised by the baffle width. Finally, better Reynolds numbers were obtained by replacing the baffle width by the horizontal coordinate of the wake centre, or by the wake width (Table 5.5 numbers 9 – 10). The Reynolds number $(\psi^{(r)}/x_1^{(s)})H/\nu$ yielded 7% error, a dramatic improvement to the default Reynolds number $V H/\nu$.

The wake heat flux was also modelled using the virtual measurements. For reference, the standard Reynolds number was used to model the wake heat flux for only the default channel geometry, yielding 9% error (Table 5.6 number 4). The best modified Reynolds number, $(\psi^{(r)}/x_1^{(s)})H/\nu$, as calculated using normal calibration, yielded 2.9% error (Table 5.6 number 5). When the virtual measurements were used instead, the error was still only 5.3% (Table 5.6 number 6). Therefore, the wake heat flux can be calculated using parameter values obtained from a small number of measured velocities.

5.5   Conclusions

The channel-baffle geometry is a good example to demonstrate main flow and recirculation combination. Based on the Schwarz-Christoffel transformation, a new model for these flows has been presented. It assumes irrotational flow in the main flow area, and the wake is modelled as a monopolar vortex. The Schwarz-Christoffel model needs nine parameters to be estimated, which are geometric characteristics of the velocity field: two vertical coordinates and one horizontal coordinate (wake width) defining straight line segments bounding the wake; the vertical coordinate of the separation point before a baffle; the horizontal coordinate of the corresponding reattachment point; the two coordinates of the vortex centre of the wake; the two-dimensional recirculation flow rate; and the ellipticity of the recirculation in the wake.

The parameters in the model were calibrated for different baffle distances H (m), channel widths W (m), baffle widths B, average inflow velocities V and chamber sequence numbers, corresponding to Reynolds numbers ranging from $6.8\,10^3$ to $3.4\,10^6$. Six parameters appeared to be constant in dimensionless form: the two vertical coordinates defining the wake boundary ($y_1^{(s)}/H = 0.14$ and $y_2^{(s)}/H = 0.73$); the vertical coordinate of the separation point before a baffle ($y_3^{(s)}/H = 0.78$); the horizontal coordinate of the corresponding reattachment point ($x_4^{(s)}/W = 0.77$); the vertical coordinate of the centre of the recirculation in the wake ($y^{(r)}/H = 0.61$); and the ellipticity of the recirculation ($\gamma^{(r)}H/B = 2.33$). The remaining variable parameters were the dimensionless wake width $x^{(s)}/W$, the dimensionless horizontal coordinate of the vortex centre $x^{(r)}/W$, and the dimensionless recirculation flow rate $\psi^{(r)}/\dot{V}$ where $\dot{V}$ is the two-dimensional volumetric flow rate in the main flow area, in $\mathrm{m^2 s^{-1}}$. Calibrating only these three parameters, instead of nine, causes only a small increase of the velocity error. With three calibrated parameters, the velocity error becomes only about 23%. Higher velocity errors only occur for the lowest Reynolds numbers, which can be explained by the vorticity field (according to CFD modelling) being different.

According to CFD modelling results, a constant temperature on the channel walls does not cause a large temperature increase in a chamber, but the temperatures in both recirculation areas are higher than the temperature in the main flow area. The heat flux from the walls can be modelled with 17% error using a standard Nusselt-Reynolds correlation. The two walls of a chamber must be considered separately, however, because there are different flow regimes near both walls. These heat fluxes can be modelled more accurately using the three variable parameters. The heat flux into the main flow is modelled with 22% error using the standard Reynolds number, but a modified Reynolds based on the wake width, $Re^{(main)} = H\dot{V}/\nu(W -$

$x_1^{(s)}$), yields 11% error (ν is kinematic viscosity in m^{2}s^{-1}): The correlation reads $Nu^{(main)} = 0.041\,Re^{(main)0.79}$ where $Nu^{(main)}$ is a Nusselt number expressing the heat flux into the main flow. The heat flux into the wake is modelled with 12% error using the standard Reynolds number, but 7% can be achieved with a modified Reynolds number including the recirculation flow rate and the wake width, $Re^{(wake)} = H\psi^{(r)}/x_1^{(s)}\nu$: the correlation reads $Nu^{(wake)} = 0.225\,Re^{(wake)0.75}$ where $Nu^{(wake)}$ is a Nusselt number expressing the heat flux into the wake. This new power-law relation applies to bounded vortices in general, because the heat flux is modelled from only the conditions in the wake.

The parameter values can also be calculated using small calibration sets having nine velocity vectors only, which can be regarded as virtual measurements. The parameters obtained from nine virtual measurements are only slightly different from the values obtained using large calibration sets. For fixed channel geometry, the heat flux into the main flow can be modelled with 5.8% error using the wake width, to be compared with 17% error from the standard Reynolds number. The heat flux into the wake can be modelled with 5.3% error, to be compared with 9% error from the standard Reynolds number. These numbers show that the heat flux can be calculated accurately from a limited number of velocity measurements.

To summarise, the Schwarz-Christoffel model has been used successfully to model the examined channel-baffle geometry. The parameters are geometric characteristics and the velocity field corresponding to given parameter values can be evaluated quickly. In addition, the parameter values can be applied in power-law models for the heat flux. All calculations were carried out with air as the flowing medium, but the medium influences the heat flux only via the Prandtl number. The Prandtl number has a limited impact and it is known that all gasses have a Prandtl number near 1. Since the examined geometry is a typical combination of main flow and recirculation flow, we conclude that the Schwarz-Christoffel model is a useful tool to model two-dimensional turbulent flows of gasses.

Chapter 6

Including Stagnant Zones in Potential Flow Theory

Notation

B	horizontal fin placement, m
D	diffusion coefficient, m^2s^{-1}
H	geometry height, m
L	fin length, m
Re	Reynolds number
V	characteristic velocity, ms^{-1}
W	geometry width, m
p	pressure, Pa
$\vec{u}$	average velocity vector (2D), ms^{-1}
x	horizontal coordinate, m
y	vertical coordinate, m
Φ	volumetric flow rate, m^3s^{-1}
δ	geometry thickness, m
η	viscosity, Pa s
ρ	density, kg m^{-3}
ϕ	potential function, m^2s^{-1}
ψ	stream function, m^2s^{-1}

Superscripts

$^{(m)}$	maximum
$^{(r)}$	recirculation
$^{(s)}$	separation

6.1   Introduction

The efficiency of many systems is determined by the residence time distribution (RTD) (Levenspiel, 1972), which can be controlled by careful design of the system geometry. An example is a waste water stabilisation pond, which only operates efficiently if there is no short circuit from the inlet to the outlet (Shilton et al., 2000; Shilton, 2000; Ta and Brignal, 1998). The impact of short-circuiting may be reduced by the placement of a baffle (Shilton, 2000; Ta and Brignal, 1998), or by another arrangement of the inlets and outlets (Ta and Brignal, 1998). Two other examples are from membrane technology. Reverse electrodialysis (Jagur-Grodzinski and Kramer, 1986) exploits the chemical potential difference between salt water and fresh water to generate electricity. Proton exchange membrane fuel cells (Grubb and Niedrach, 1960) generate electricity from hydrogen reacting with oxygen. In

both examples, fluids are forced in between semipermeable membranes, and the local electric potential over a membrane surface element depends on the reactant concentrations at both sides. The acting concentration differences depend on the RTD's of the particles in the flow. Leakage currents parallel to the membranes have been observed in reverse electrodialysis cells (Rubinstein et al., 2001), which may be caused by salt concentration differences (Post et al., 2007). To reduce leakage currents, control of the velocity distribution by baffles has been considered (Chapter 4). Furthermore, baffles can be used to improve the efficiency of proton exchange membrane fuel cells (Liu et al., 2005). These examples have a two-dimensional nature, and the present research is aimed at designing models that predict the impact of the two-dimensional geometry on the RTD.

In Chapter 4, potential flow theory was applied to analyse the impact of the system geometry on the RTD. Potential flow theory applies to creeping flows (Reynolds number Re up to about 500, see *Fig.* 6.1). For turbulent flows ($Re > 2000$,
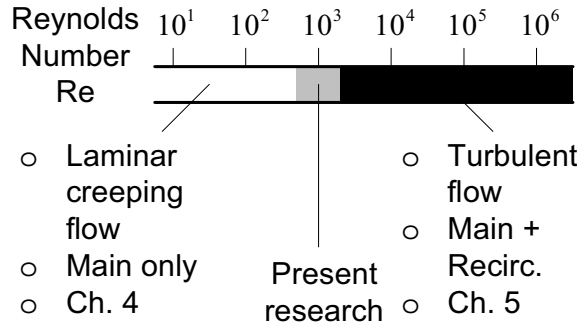

Figure 6.1:   Relation between the Reynolds number Re and the flow features

see *Fig.* 6.1), it was shown that potential flow theory can be applied if there is no boundary layer separation (Batchelor, 1967), but boundary layer separation often plays a role (Schlichting, 2000). Obstructions in the flow domain induce boundary layer separation, causing mixing layers that act as virtual boundaries. These virtual boundaries divide the flow in a main flow and adjacent recirculation wakes. In Dirkse et al. (2007b), potential flow theory was extended to model the velocity field for this type of flows. However, the validity of extended potential flow modelling for medium-Reynolds-number laminar flows ($500 < Re < 2000$, *Fig.* 6.1) remains to be investigated.

When the velocity field is known, the RTD can be obtained by neglecting diffusion and dispersion. This assumption implies that each particle flowing on a particular streamline has the same residence time. The RTD can be calculated from the differences in residence time of the different streamlines. However, in Chapter 4

this new model was validated only for creeping flows, having no recirculation wakes. Further research is required to extend the new model for the RTD to higher Reynolds numbers, which may result in both a main flow and recirculation wakes.

The present research focusses to medium-Reynolds number laminar flows ($500 < Re < 2000$, *Fig.* 6.1), and the following research questions are addressed: (a) can the velocity field of medium-Reynolds-number laminar flows be modelled by extending potential flow theory; and (b) can the new model for the RTD be applied to flows including a main flow and recirculation wakes?

6.2 Reference data based on computational fluid dynamics

The investigation of extended potential flow modelling requires a data set with reference velocity fields and reference residence time distribution graphs. This data set was required for the analysis of variations of the volumetric flow rate and the two-dimensional geometry. Physical experiments offer limited possibilities to vary the system geometry, and hence the reference data set was taken from computational fluid dynamics models (Patankar, 1980).

The reference data set was obtained by modelling variations of a two-dimensional geometry, which was chosen such that a main flow and recirculation wakes could be expected (*Fig.* 6.2). This shape has been investigated experimentally in Chapter 4. A fluid source was at the bottom-left corner, a fluid sink at the top-right corner and the flow was obstructed by a vertical baffle. The varied geometry dimensions were the width between the wall and the fin B (m), the fin length L (m), the geometry width W (m) and the geometry height H (m). The shape *Fig.* 6.2 was assumed to be a gasket, which was clamped between two flat plates; the gasket thickness δ (m) was assumed to be $\delta = 1.0$ mm. All investigated geometries were variations of a default geometry defined by $B = 32$ mm, $L = 60$ mm, $W = 116$ mm and $H = 138$ mm. The volumetric flow rate Φ (m^{3}s^{-1}) was also varied, which was transformed to the two-dimensional flow rate $\psi^{(m)} = \Phi/\delta$ ($\psi^{(m)}$ is maximum of stream function, m^{2}s^{-1}). To define the Reynolds number Re, the characteristic velocity V (ms^{-1}) was defined as $V = \psi^{(m)}/B$. The theory of flow between parallel plates defines the hydraulic diameter to be 2δ, resulting in $Re = 2\delta V \rho/\eta$ with ρ the density (kg m^{-3}) and η the dynamic viscosity (Pa s) of water. Reynolds numbers from 250 up to 2000 were examined, corresponding to characteristic velocities up to $V = 1.0$ ms^{-1}, allowing us to study extended potential flow modelling for a wide range of applications.

The CFD model considered the system as two-dimensional, and the dependent variable was the average velocity over the distance between the plates $\vec{u}$ (ms^{-1}) (Chapter 4). The drag force applied by the parallel plates was modelled as a
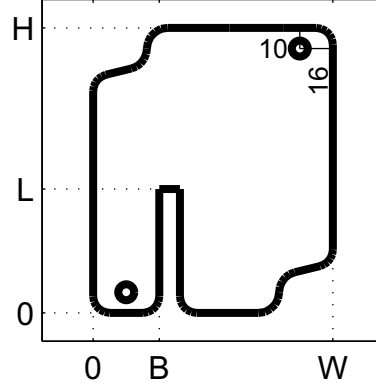
Figure 6.2:   Set of investigated two-dimensional geometries, resulting from varying the geometry dimensions B, W, L and H; shown dimensions in mm; dimensions not shown: fin width 10 mm, source location $(B/2, 10$ mm$)$

momentum sink in the Navier-Stokes equations (Hsu and Cheng, 1990), and the magnitude of the momentum sink was taken from the theory of parallel flow between flat plates (Chapter 4). The resulting momentum equation reads:

$$\rho(\vec{u} \cdot \operatorname{grad}) \, \vec{u} = -\operatorname{grad} p + \eta \operatorname{div} \operatorname{grad} \vec{u} - \frac{12\eta}{\delta^2}\vec{u} \tag{6.1}$$

with p the pressure (Pa). Turbulence was not included in the model, although Reynolds numbers up to 2000 were investigated. The reason is that the laminar or turbulent regime is determined by the transversal direction (flow between plates), and not by the parallel direction (flow around obstacles). The boundary conditions of the momentum equation were a given total pressure $(p + (1/2)\,\rho\,\|\vec{u}\|^2)$ at the inflow boundary, a no-slip condition at the boundaries of the two-dimensional plane, and an outflow boundary condition at the outflow boundary (Patankar, 1980). To calculate the velocity field for a specified Reynolds number, the total pressure at the inflow boundary was iteratively adjusted until the solution of the Navier-Stokes equations produced the required two-dimensional flow rate $\psi^{(m)}$. All CFD calculations were performed using the commercial package Fluent (Fluent Inc., 2007). A quadrilateral mesh was applied having mesh intervals of about 1 mm, resulting in about 15,000 cells.

To calculate the residence time distribution (RTD) with the CFD model, the concentration had to be included using the convection-diffusion equation. In Hsu and Cheng (1990) dispersion in porous media was modelled by increasing the diffusion

coefficient D (m^{2}s^{-1}), but this assumption is not realistic in this case because dispersion is only expected in the direction of the flow. Therefore, dispersion was ignored in the present study. The diffusion coefficient was set to $1.5 \cdot 10^{-9}$ m2s^{-1}, a very low value that in theory removes diffusion from the CFD model. Furthermore, the volume of the tracer material was ignored, making the fluid properties independent of the tracer concentration. Buoyancy effects were ignored because the geometry is oriented horizontally, and therefore the momentum equation could be solved independently from the convection-diffusion equation. The RTD was calculated by dynamically solving the convection-diffusion equation. A block signal was applied for the tracer concentration, having a short pulse length compared to the expected residence times.

6.3 Models for the residence time distribution

Computational fluid dynamics modelling is complicated and generally requires long calculation times, and therefore simpler and faster models were investigated. Many researchers have modelled the RTD already. It can often be modelled accurately with a first-order or second-order model (Young and Lees, 1993; Young et al., 2000), in some cases extended with a dead time (Stephanopoulos, 1984). These models are very useful for control purposes because the dynamics of the output concentration can be predicted from the dynamics of the input concentration. The parameters of these models can be interpreted physically as time constants that are related to virtual compartments (Kailath, 1980; Young et al., 2000). Nevertheless, the parameters depend on the system geometry, and they have to be calibrated separately for every system geometry. Therefore, an alternative modelling method was pursued.

In Chapter 4, a new model was presented that predicts the impact of the geometry on the RTD. The model is based on potential flow theory, which calculates the two-dimensional velocity field. Potential flow theory applies a conformal map from the physical domain to the infinite strip, where the two coordinates are the potential function ϕ (m^{2}s^{-1}) and the stream function ψ (m^{2}s^{-1}). The height of the strip equals the two-dimensional flow rate $\psi^{(m)}$, and therefore ψ satisfies $0 < \psi < \psi^{(m)}$. Bounded flows with an internal source and an internal sink are also found by mapping the flow domain to the infinite strip, but in this case the internal source is mapped to $-\infty$, and the internal sink is mapped to $+\infty$ (see Chapter 4). The two-dimensional average velocity $\vec{u}$ is the gradient of the potential function ϕ, and hence the velocity is found by differentiation of the conformal map.

Potential flow theory applies to flows characterized by small Reynolds numbers, but when the Reynolds number is higher, obstructions in the flow may cause boundary layer separation and turbulence (Batchelor, 1967; Roberts, 1994). In Dirkse et al.

(2007b), highly turbulent flow in an obstructed channel was modelled, and boundary layer separation induced mixing layers originating from the separation points. Behind the mixing layer, recirculating flow was found. The flow was modelled by extending potential flow theory. The mixing layers are approximated by straight line segments, defined by virtual separation vertices. The recirculation wakes behind the mixing layers are assumed to be monopolar vortices, which are characterized by the two coordinates of the vortex centre $(x^{(r)}, y^{(r)})$ and a vortex strength $\psi^{(r)}$ $(\mathrm{m^2 s^{-1}})$ (*Fig.* 6.3). The velocity field in the main flow area is modelled based on a conformal map to the infinite strip, and the velocity field in a recirculation wake is modelled based on a conformal map to the unit disc. The velocity field in a recirculation wake is calculated by considering the disc as a rigidly rotating body, see (Dirkse et al., 2007b) and Appendix A. In the present research, it is investigated whether extended potential flow modelling applies to medium-Reynolds-number flows in the geometry *Fig.* 6.2; the coordinates of the relevant separation vertices are $(x_1^{(s)}, y_1^{(s)})$, ..., $(x_4^{(s)}, y_4^{(s)})$ (*Fig.* 6.3).
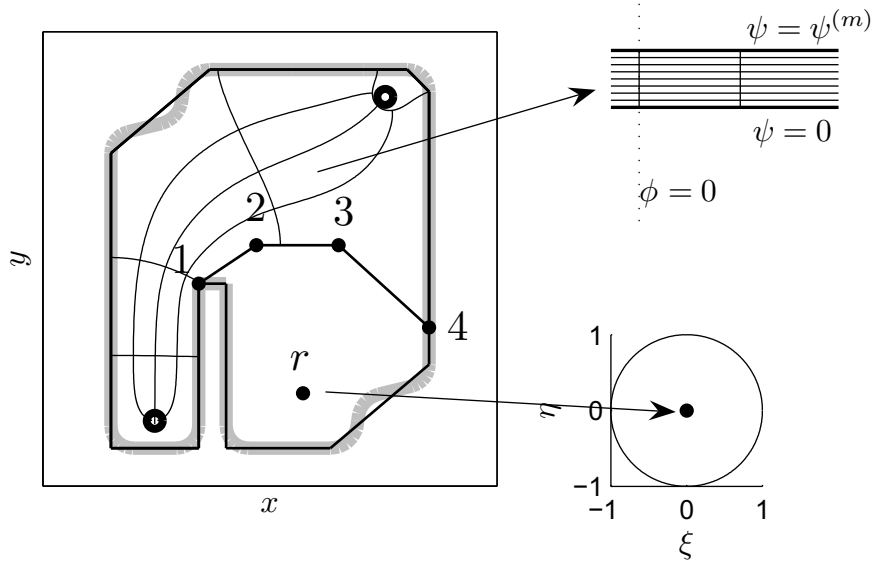

Figure 6.3: Explanation of extended potential flow modelling; calibrated characteristics are the coordinates of the points 1, 2, 3, 4 and r being $(x_1^{(s)}, y_1^{(s)})$, ..., $(x_4^{(s)}, y_4^{(s)})$ and $(x^{(r)}, y^{(r)})$, and the vortex strength $\psi^{(r)}$ (not shown)

This explanation shows that extended potential flow modelling has unknown parameters, being the geometric characteristics $x_1^{(s)}, \ldots x_4^{(s)}$, $y_1^{(s)}, \ldots, y_4^{(s)}$, $x^{(r)}, y^{(r)}$ shown in *Fig.* 6.3, and the vortex strength $\psi^{(r)}$ (eleven parameters). For given parameter values (characteristics), extended potential flow modelling produces an approximation of the velocity field. An iterative optimization algorithm based on

Sequential Quadratic Programming (Schittowski, 1985) searches parameter values to match a given velocity field (implementation details given in Appendix A). The algorithm requires many evaluations of the model, and hence fast evaluation of extended potential flow modelling is important. The model can only be evaluated for polygonal domains, and hence the round corners in *Fig.* 6.3 must be approximated with straight line segments. The calculation time depends strongly on the number of line segments, and therefore the round corners (thick boundary in *Fig.* 6.3) were approximated in extended potential flow modelling by a limited number of line segments (thin boundary in *Fig.* 6.3). The algorithm was used to calibrate extended potential flow modelling against given velocity fields (CFD modelling results).

In model identification theory, the degrees of freedom (d.o.f.) are chosen based on a trade-off between the number of fitted variables and the model error. The concept of a parsimonious model has been introduced to express the optimal choice for the fitted degrees of freedom (Burnham and Anderson, 2002). To search for a parsimonious model, the number of d.o.f. in extended potential flow modelling was varied. The number of d.o.f. is smaller than the number of calibrated parameters, because both $(x_1^{(s)}, y_1^{(s)})$ and $(x_4^{(s)}, y_4^{(s)})$ must be on the boundary of the two-dimensional domain. As a consequence, these four parameters constitute only two degrees of freedom.

There are no d.o.f. when the main flow area is modelled to be the entire flow domain, which implies that there are no recirculation wakes and no separation lines. This empty parameter selection corresponds to ordinary potential flow modelling. The number of d.o.f. is increased by introducing the separation line and the recirculation wake behind it (*Fig.* 6.3). There is no turbulent momentum transport from the main flow area to the recirculation wake, and hence the flow there is driven only by molecular diffusion. This effect may be ignored by modelling the recirculation wake to be stagnant, eliminating the parameters $(x^{(r)}, y^{(r)})$ and $\psi^{(r)}$. The minimum number of d.o.f. is obtained by fixing $(x_1^{(s)}, y_1^{(s)})$ at the first concave corner, which is the left corner of the baffle tip. One vertex $(x_3^{(s)}, y_3^{(s)})$ can be omitted, and hence the minimum number of d.o.f. implies that there is a line segment connecting $(x_2^{(s)}, y_2^{(s)})$ and $(x_4^{(s)}, y_4^{(s)})$. The parameters $x_4^{(s)}$ and $y_4^{(s)}$ are constrained by the equation of the two-dimensional boundary, and therefor they require only one degree of freedom. In the minimal parameter selection, the parameters $x_2^{(s)}, y_2^{(s)}, x_4^{(s)}, y_4^{(s)}$ remain to be calibrated, requiring three degrees of freedom. It was investigated whether the accuracy of potential flow modelling improves when more separation vertices are calibrated, and when molecular diffusion to the recirculation wake is included by calibrating $(x^{(r)}, y^{(r)})$ and $\psi^{(r)}$. The error of potential flow modelling was defined as the root-mean-square of the local velocity errors; the local velocity error at a location was the norm of the difference vector between the given vector and the modelled vector. The optimal (parsimonious) parameter selection was chosen to take

into account the trade-off between the model error and the number of degrees of freedom.

The new model for the RTD (Chapter 4) can be combined with extended potential flow theory. The RTD is calculated by neglecting mass diffusion and dispersion. This assumption implies that the residence time of each streamline is fixed. The residence time of a streamline is evaluated as the path integral of the reciprocal of the velocity magnitude (integrating sm^{-1} over a path yields a time in s). The residence time distribution follows from the differences in residence time of the different streamlines. Although leaving out diffusion and dispersion caused considerable model errors compared to tracer experiments, it was demonstrated in Chapter 4 that the model is a useful tool to analyse the impact of the geometry on the RTD (see Chapter 4 and Appendix A for implementation details). However, in Chapter 4 no recirculation wakes were present due to the Reynolds number being low (< 500). For flows including a main flow and recirculation wakes, the RTD is modelled by assuming that there is no diffusion into the recirculation wakes. The RTD is modelled as in Chapter 4, but for calculating the RTD the flow domain is taken to be the main flow area only.

6.4   Results and discussion

First, it was verified that ordinary potential flow modelling agrees with the reference data (CFD results) for creeping flows. Figure 6.4a shows a reference velocity field for Reynolds number 250. The velocities are large to the left of the fin and to the top, and lower velocities are observed to the right of the fin. The same flow pattern is obtained by potential flow modelling (*Fig.* 6.4b), which results in a relative velocity error of 18%.

The situation is different when the Reynolds number is increased, see *Fig.* 6.5a for $Re = 1750$. The velocity is relatively lower to the right of the fin, resulting in an increased error of ordinary potential flow modelling: 40% (Table 6.1 row 1). It was investigated whether this error can be reduced by introducing a separation line from the fin tip at $(x_1^{(s)}, y_1^{(s)}) = (32, 60)$ (in mm), which continues to $(x_2^{(s)}, y_2^{(s)}) = (40, 80)$ and reattaches at $(x_4^{(s)}, y_4^{(s)}) = (116, 80)$. Applying potential flow theory on the area bounded by the virtual boundary and modelling stagnant flow in the remainder of the domain, results in only 21% error (Table 6.1, row 2). The corresponding velocity field is shown in *Fig.* 6.5b, and it closely resembles the reference from CFD modelling *Fig.* 6.5a.

The coordinates of the three separation vertices were found by fixing $(x_1^{(s)}, y_1^{(s)})$ and calibrating the coordinates $x_2^{(s)}, y_2^{(s)}, x_4^{(s)}, y_4^{(s)}$, corresponding to three degrees of freedom (d.o.f.) because $x_4^{(s)}$ and $y_4^{(s)}$ were coupled by the equation for the two-
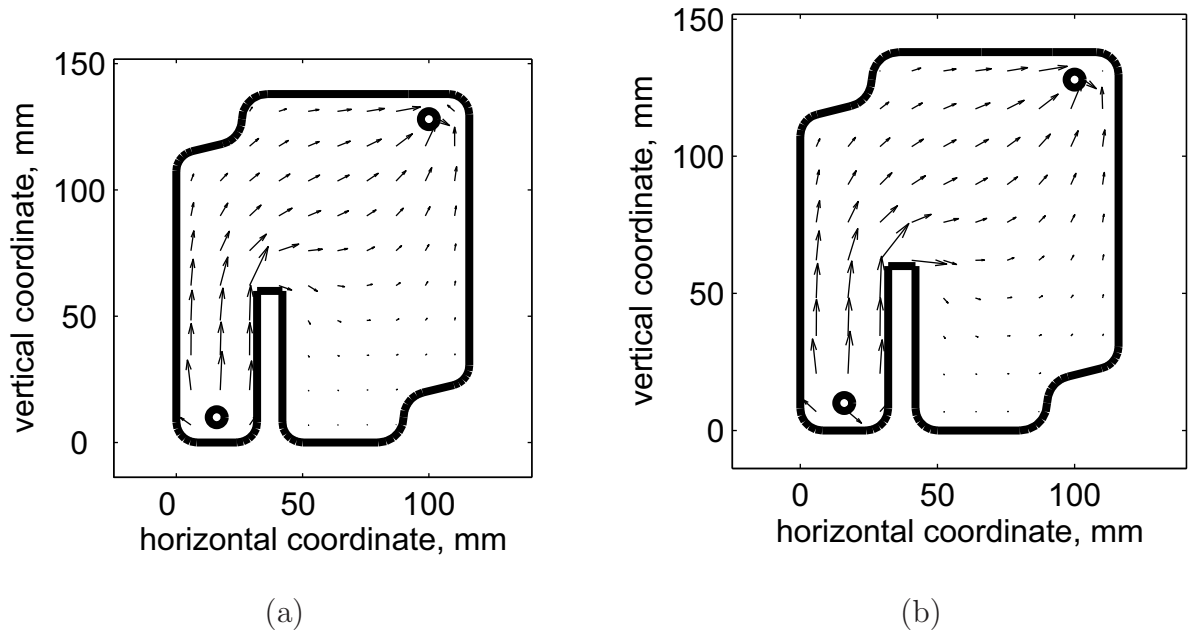
Figure 6.4: Velocity fields for default geometry and Re = 250; reference from CFD modelling (a) ordinary potential flow modelling (b)

Table 6.1: Relative velocity errors obtained from calibrating different parameter selections; calibration set H = 138 mm, W = 116 mm, B = 32 mm, L = 60 mm, and Re = 1750; x = calibration algorithm did not converge

calibrated d.o.f.			relative
separation	recirculation		velocity
line	area	total	error, %
0	0	0	40
3	0	3	21
4	0	4	27
5	0	5	21
6	0	6	x
3	3	6	20

dimensional boundary. It was investigated whether the error could be reduced by fitting more parameters. First, the separation point $(x_1^{(s)}, y_1^{(s)})$ was added to the calibrated characteristics, requiring one extra d.o.f. (Table 6.1, row 3). This parameter selection caused the relative velocity error to increase, demonstrating that the assumed location $(32, 60)$ for the separation point was correct. The location of the separation point was fixed to $(32, 60)$ again, but the extra separation vertex $(x_3^{(s)}, y_3^{(s)})$ was added. There were five d.o.f. in this case, but the relative velocity
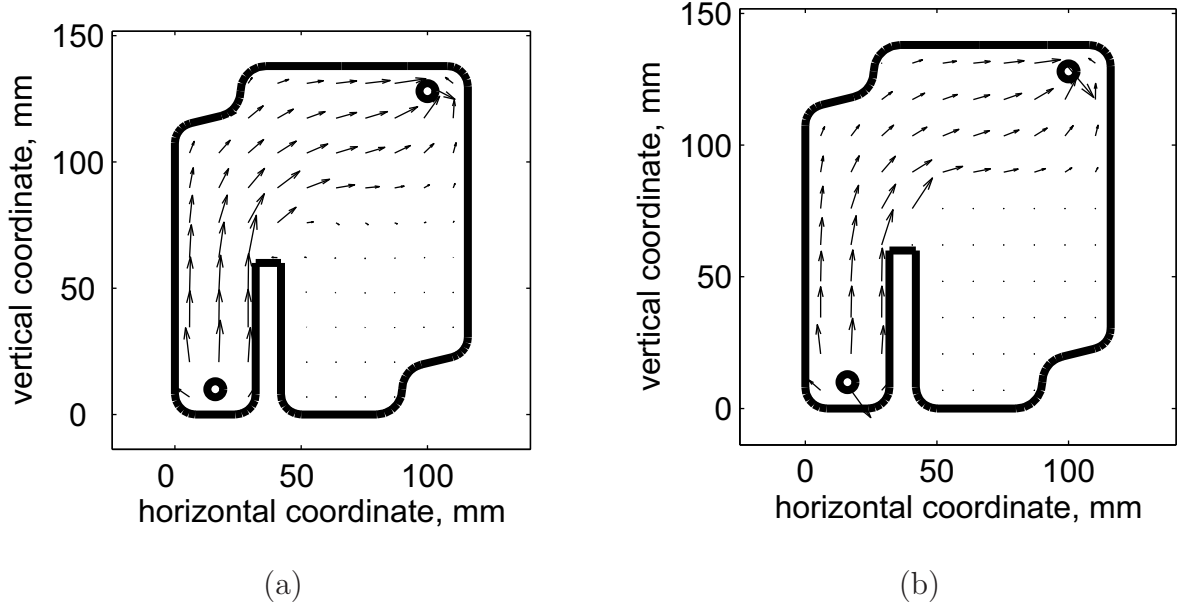
(a) (b)

Figure 6.5: Velocity fields for default geometry and Re = 1750; reference from CFD modelling (a) and extended potential flow modelling with three calibrated degrees of freedom (b)

error was the same as obtained with three d.o.f. (Table 6.1, row 2 and row 4). When a sixth d.o.f. was added by calibrating all four separation vertices in *Fig.* 6.3, the algorithm did not converge.

Finally, the separation line was modelled with three d.o.f., but $x^{(r)}, y^{(r)}$ and $\psi^{(r)}$ were added to model a non-stagnant flow to the right of the fin, resulting in six d.o.f. in total (Table 6.1, last row). Again, there was no improvement compared to using three d.o.f. (Table 6.1, row 2). This result can be explained from the velocities being very low to the right of the fin, making zero a good approximation. It can be concluded that fitting three d.o.f. is the optimal choice.

Having established that the parameter selection $x_2^{(s)}, y_2^{(s)}, x_4^{(s)}, y_4^{(s)}$ (three d.o.f.) is parsimonious, the model was calibrated for different Reynolds numbers. The location of the second separation vertex was almost constant, and it was close to the baffle tip; it varied between $(40, 80)$ and $(60, 80)$. However, the Reynolds number had a large impact. The recirculation area increased with increasing Reynolds number, because the vertical coordinate of the reattachment point, $y_4^{(s)}$, moved upward from 40 mm for $Re = 1250$, to 90 mm for $Re = 2000$. At constant Reynolds number $Re = 2000$, the fin length L and the geometry height H were varied (*Fig.* 6.3). The second separation vertex varied in accordance with the fin length L, with almost no sensitivity to the geometry height H (Table 6.2, column 3); the coordinate $x_2^{(s)}$ varied between 40 mm and 50 mm. Increasing the fin length L caused higher reattachment (Table 6.2, row

Table 6.2: Impact of varying the height H and the fin height L on the separation line

geometry variation		separation	
geometry height	fin height	vertex coordinate (*Fig.* 6.3), mm
H, mm	L, mm	$y_2^{(s)}$	$y_4^{(s)}$
138	60	80	90
138	102	110	120
216	60	80	120
294	60	90	120

Table 6.3: Impact of varying the width W and the fin location B on the separation line, x = the algorithm produced solutions dependent on the initialization

geometry variation		reattachment	
geometry width	fin placement	coordinate, (mm)
W (mm)	B (mm)	$x_4^{(s)}$	$y_4^{(s)}$
116	32	116	90
116	48	116	100
116	60	116	100
190	32	x	x
264	32	100	0

2); reattachment occurred above the fin tip in all investigated variations. Increasing the geometry height H also caused higher reattachment, but the change of the reattachment location was small compared to the change of the height H (Table 6.2, rows 1, 3 and 4). Finally, the fin location B and the geometry width W were varied (Table 6.3). The second separation vertex remained close to the baffle tip. Variations of B had no impact on the reattachment location, but varying W had a large impact. When W was changed from 116 to 190 mm, the produced solution depended on the initialization of the calibration algorithm. For $W = 264$ mm, reattachment occurred at the bottom ($y_4^{(s)} = 0$) and before the bottom-right corner (Table 6.3, last row). The impact of geometry variations can be summarized roughly as follows: The separation line starts from the fin tip and turns clockwise to end at the right boundary or the bottom boundary (*Fig.* 6.3), and the turning angle increases with increasing distance between the fin tip and the right boundary. For all investigated variations of the Reynolds number and the geometry, the error of extended potential flow modelling varied from 13% to 35%, showing reasonable agreement with the CFD modelling

results.

Having established that extended potential flow modelling provides a reasonable approximation of the velocity field, it can be applied as a building block of the new model for the RTD. The reference was a virtual tracer experiment calculated using CFD modelling (*Fig.* 6.6). The tracer flowed past the fin, and than via the

(a)   (b)
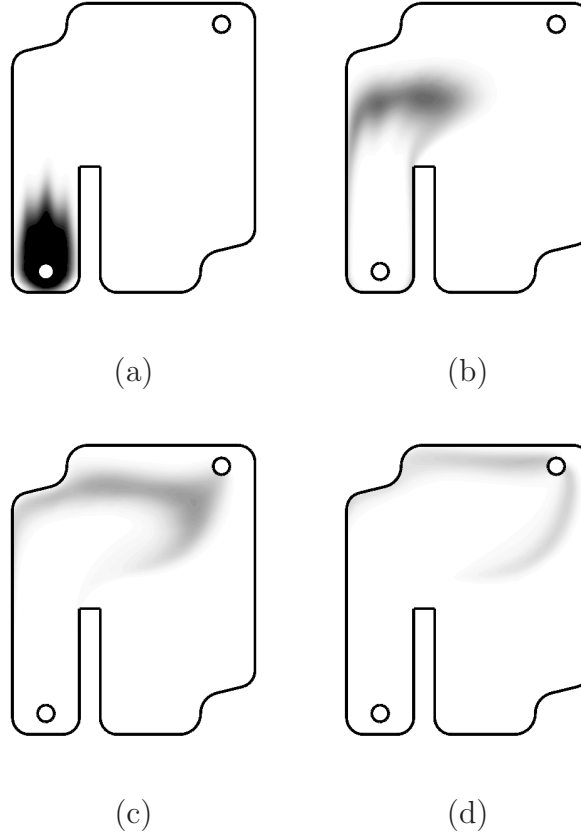

(c)   (d)

Figure 6.6:   Computational fluid dynamics simulation of tracer concentration for geometry height $H = 138$ mm, geometry width $W = 116$ mm, fin length $L = 60$ mm and fin location $B = 32$ mm (see *Fig.* 6.3); (a) at end of injection at 0.032 s; (b) at 0.108 s; (c) at 0.184 s; (d) at 0.259 s

top area to the sink (*Fig.* 6.6, b and c). Some tracer was retarded near the left boundary and near the separation line, but most tracer flowed quickly to the sink (*Fig.* 6.6, b – d). The dynamic CFD calculation produced a reference residence time distribution, which resembled a first-order process with dead time (*Fig.* 6.7, solid line). The dead time was about 0.2 s, and this dead time was predicted correctly by the new model for the RTD including a stagnant zone (*Fig.* 6.7, dashed line). The peak outflow concentration was not modelled correctly. However, the new model including a stagnant zone outperformed the new model with only main flow (the
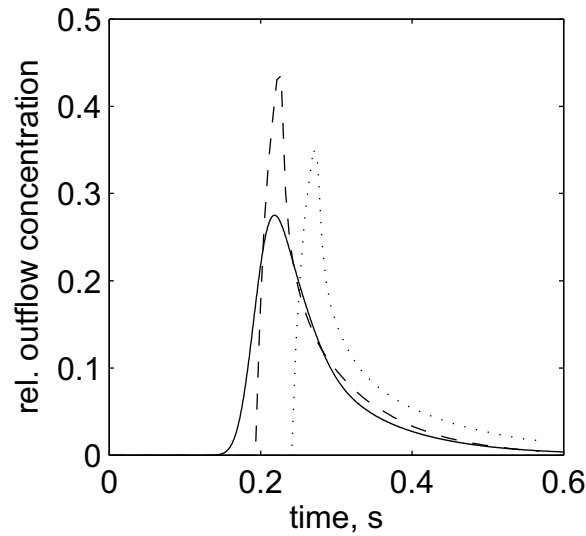
Figure 6.7: Residence time distributions corresponding to *Fig.* 6.6 and calculated by CFD modelling (solid), by the new model with main flow only (dotted), and by the new model including a stagnant zone (dashed)

model of Chapter 4). With only main flow, the dead time was over-predicted (*Fig.* 6.7, dotted line), because ordinary potential flow theory under-predicted the velocity magnitude to the top. This trend was also observed for the other geometry variations. The dead time is predicted correctly including a stagnant zone, and over-predicted with main flow only.

To investigate the cause of error for the peak outflow concentration, the accuracy of the reference CFD calculation was investigated by refining the mesh. Refining the mesh had only a small effect on the velocity field (the difference could not be seen by visually comparing velocity vector plots). However, refining the mesh caused an increment of the peak outflow concentration, reducing the difference with the new model for the RTD (*Fig.* 6.8). It follows that the observed 'error' of the new model is partly due to inaccuracy of the reference.

To test the relevance of the new model for design purposes, residence time distribution graphs were calculated for different geometry variations (*Fig.* 6.9). Increasing the fin length L reduces the dead time and increments the peak outflow concentration. This can be explained, because the width of the main flow area is reduced, causing an increment of the velocity magnitude. Furthermore, the width variation of the main flow area is reduced, reducing geometry-induced variations of the residence time. Increasing the geometry height H increments the path length from the source to the sink, and introduces more variation of the main flow area width. Therefore, it can be explained that the dead time increases, and also that the
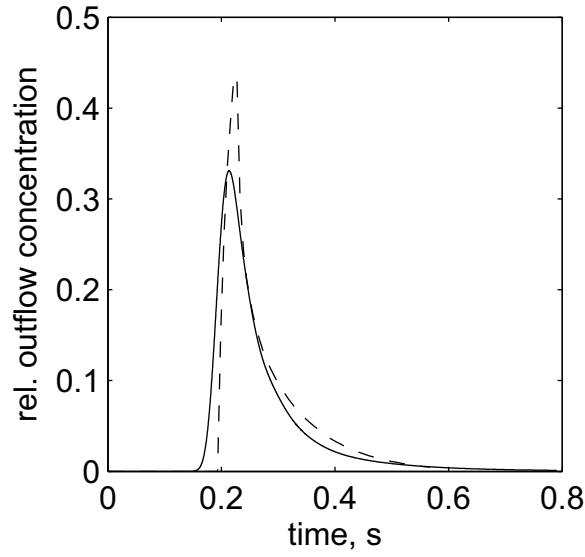
Figure 6.8: Residence time distributions corresponding to *Fig.* 6.6, and calculated by CFD modelling based on a finer mesh (solid), and by the new model for the RTD including stagnant zone (dashed)
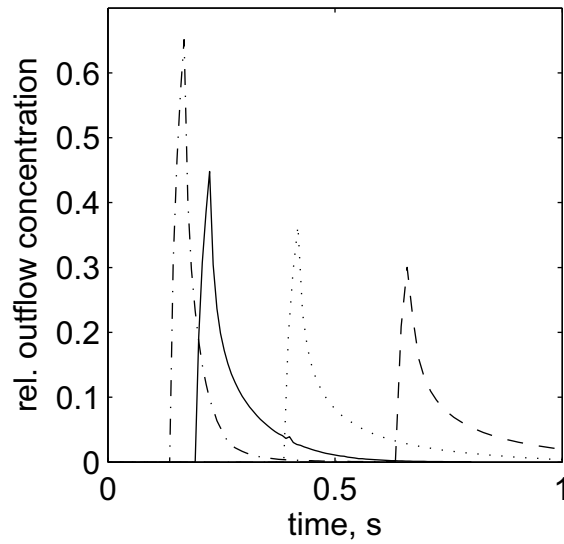

Figure 6.9: Comparison for different geometries of residence time distribution calculated by the new model including a stagnant zone; all had Reynolds number 2000 and injection duration 0.032 s; default geometry (solid); longer fin, $L = 102$ mm (slash-dot); increased height, $H = 216$ mm (dotted); and much increased height, height $H = 294$ mm (dashed)

peak outflow concentration decreases.

6.5   Conclusion

The residence time distribution (RTD) is generally modelled by dividing the flow domain in perfectly mixed compartments (CSTRs), and parameters of these models can be interpreted physically as time constants. In existing compartment models, it is difficult to relate these parameters to the system geometry, and therefore a geometric design model is developed. The present research models the RTD based on a reduced model for the velocity field, and focusses to two-dimensional medium-Reynolds-number flow ($1250 < Re < 2000$). It can be concluded that the velocity field of medium-Reynolds-number laminar flows can be modelled by extended potential flow modelling, which divides the system geometry in a main flow and adjacent recirculation wakes. The velocity field in the main flow area is modelled using a conformal map from the main flow area to the infinite strip. The flow in the recirculation wakes is driven by molecular diffusion only, causing very low velocities there. Therefore, the recirculation wakes in medium-Reynolds-number flows can be modelled as stagnant zones. Furthermore, a separation line between the main flow and a recirculation wake can be approximated with a small number of straight line segments.

The coordinates of the separation vertices are parameters of extended potential flow modelling, and these geometric characteristics were calibrated against reference velocity fields obtained from computational fluid dynamics models. Calibration was performed using an iterative optimization algorithm that can be evaluated for different numbers of unknown separation vertices, allowing variation of the number of degrees of freedom (d.o.f.). Therefore, the number of d.o.f. can be optimized to get a parsimonious model, which means that the trade-off between the number of calibrated variables and the model accuracy is taken into account. Extended potential flow modelling was calibrated with three degrees of freedom for variations of an obstructed geometry, and both the Reynolds number and the geometry were varied. Clear relations were found between the Reynolds number and the key geometry features on the one hand, and the characteristics of the velocity field (the fitted parameters) on the other hand.

It can be concluded that new model for the residence time distribution can be applied to flows including a main flow and recirculation wakes. The RTD is modelled by ignoring diffusion and dispersion, and therefore each streamline from the source to the sink has a fixed residence time. The RTD can be calculated from the differences in residence time of these streamlines. The streamlines from the source to the sink cover the main flow area by definition. Diffusion from the main flow to the recirculation

wakes is ignored, and therefore only the geometry of the main flow area and the area flow rate determine the RTD. A reference data set for the RTD was obtained using dynamic CFD calculations. The dynamic behaviour of the concentration field was calculated, resulting in reference graphs for the RTD. The RTD resembled a first-order process with dead time. The dead time was correctly predicted by the new model including a stagnant zone. The recirculation wake in the model was essential, because the dead time was over-predicted by the new model with only main flow (which is the model of Chapter 4). The accuracy of the new model for the RTD is reasonable (*Fig.* 6.7). The RTD was modelled for different geometries, and it can be concluded that the new model is a useful tool to predict the impact of the geometry on the residence time distribution.

Both the reference CFD model and the new model for the RTD ignored diffusion and dispersion. Therefore, more research is recommended to model the impact of these phenomena on the RTD. The new model is promising, because the analysis behind it ensures that false diffusion is eliminated, in contrast to CFD models.

Chapter 7

Conclusions and Recommendations

7.1   Conclusions

Heat and mass transfer in environmental and agricultural systems have been analysed with three modelling methods, namely lumped modelling, computational fluid dynamics modelling, and potential flow modelling. Based on the results, general answers can be given to the research questions formulated in Section 1.5.

It was investigated to which extend lumped engineering models can be applied to design spatially distributed environmental and agricultural systems. As an example, a heat exchanger driven by natural convection was considered in Chapter 3. It consists of a vertical channel with vertical water-filled tube rows in the centre. Forced convection heat exchangers are commonly modelled based on the logarithmic mean temperature difference. This lumped model was extended by an equation for the air flow rate to include natural convection. The air flow rate was related to the buoyant force, which was assumed to be proportional to the relative average air temperature. Although the baffles induce recirculation wakes, the air flow and the water flow could be modelled as one-dimensional channel flows, resulting in two coupled ordinary differential equations. The solution resulted in an algebraic relation that expressed the air flow rate as a function of the inflow and outflow temperatures of the air and water flows. In combination with existing theory, this new equation allows the heat flux to be calculated within 9% error bounds, and the air flow rate to be calculated within 18% error bounds (compared to experimental data on a specific geometry). The model for the heat exchanger has two unknown parameters, being the heat transfer coefficient and a modified drag coefficient. These parameters were calibrated separately for variations of the geometry. The heat transfer coefficient was almost the same for each geometry, but the modified drag coefficient differed at most 35% from the average drag coefficient over all investigated geometries. Geometric effects may be ignored by using average parameter values, but the model becomes more accurate when geometry-specific parameter values are applied.

In Chapter 5, forced convection through a baffled channel was investigated. The Reynolds number was varied from $6.8 \cdot 10^3$ to $3.4 \cdot 10^6$, and therefore the flow was turbulent. Although the baffles induced recirculation wakes, the heat flux from the walls could be modelled with an average error of 17% using a Nusselt-Reynolds correlation, effectively modelling the flow as parallel flow past a flat plate. To obtain a more accurate model, a spatially distributed model including the vertical coordinate is required that takes the channel geometry into account.

These two examples demonstrate that combinations of a main flow and recirculation wakes can be modelled reasonably accurate as one-dimensional channel flows, provided that the heat sources are planes parallel to the flow. In some cases, the one-dimensional approximation can be solved analytically, resulting in a lumped model.

Lumped models do not predict the impact of geometry variations, and hence it can be concluded that the impact of geometry variations on the system performance is limited. Lumped models can be used early in the design process to decide on the general system architecture, or they can be applied to analyse a specific geometry based on parameter values that are calibrated for the specific geometry.

The impact of the detailed geometric design on the system performance can be analysed using computational fluid dynamics (CFD) modelling. Calculation times are generally long, and therefore it was examined how CFD models can be used efficiently to design spatially distributed environmental and agricultural systems. Three cases were modelled, being (a) the shell-and-tube heat exchanger driven by natural convection (Chapter 2), (b) two-dimensional turbulent flow through a channel with baffles (Chapter 5), and (c) two-dimensional laminar flow in a bounded domain with an internal fluid source and an internal fluid sink (Chapter 6). All three cases were analysed using the commercial software package Fluent, which ran on a personal computer with 2 GB of RAM and a CPU clock frequency of 3 GHz.

The heat exchanger was a three-dimensional object, but symmetry lines were applied to reduce the heat exchanger to an almost two-dimensional problem. The shape of the tubes was also simplified, resulting in a relatively small mesh (about 30,000 cells). It had to be investigated whether black-body radiation is significant, because ignoring black-body radiation strongly reduced the required calculation time. Black-body radiation could be ignored, because there were three tube rows that intercepted each other's radiation. Turbulence had to be included, because the Rayleigh number was more than 10^8, and the k-ω turbulence model was applied (Section 1.2). The model without radiation could be evaluated in about eight minutes. The model was validated experimentally, and the accuracy was reasonable (max. 9% error for the heat flux). The model predicts the impact of geometry variations on the heat flux, the volumetric air flow rate and the outflow temperature of the water. Based on these model results, design recommendations could be presented for the heat exchanger driven by natural convection.

In the second case, two-dimensional turbulent flow through a channel, boundary layer separation was expected, resulting in thin mixing layers between a main flow and recirculation wakes. To handle the large velocity gradients without using many mesh cells, dynamic grid adaptation was used: the mesh was refined during the iterative solution of the CFD model. The calculation time was in the order of one hour, which is considerably longer than the calculation time for the first case.

Finally, two-dimensional laminar flows could be evaluated surprisingly fast with computational fluid dynamics modelling, because thin mixing layers were not expected. The velocity field could be calculated in roughly half a minute, and

the dynamics of the tracer concentration could be calculated in about a quarter of an hour. The velocity field was modelled correctly, because the result remained unchanged after grid refinement. However, grid refinement resulted in a small change of the residence time distribution. This can be explained, because the diffusion coefficient ($1.5 \cdot 10^{-9}$ m^{2}s^{-1}) was much smaller than the kinematic viscosity ($1.0 \cdot 10^{-6}$ m^{2}s^{-1}). To remove false diffusion, more mesh cells are required, making the calculation more lengthy. It can be concluded that CFD requires very careful mesh design together with long calculation times for buoyant flow and in avoiding false diffusion.

To obtain faster evaluation methods for convective transport, potential flow theory (Section 1.4) was revisited and extended. For creeping flows, it is known that two-dimensional velocity fields can be evaluated using a conformal map to the unit strip, which can be evaluated using the Schwarz-Christoffel theorem. However, potential flow theory is not sufficient to model medium-Reynolds-number laminar flows and turbulent flows; these flows are combinations of a main flow and recirculation wakes. Potential flow theory can be extended to model general flow problems including a main flow and recirculation wakes. Extended potential flow theory models the main flow using a conformal map to the infinite strip. For medium-Reynolds-number laminar flows, momentum transport from the main flow to the recirculation wakes can be neglected. In this case, the recirculation wakes can be modelled as stagnant zones. For turbulent flows, extended potential flow theory models a recirculation wake using a conformal map to the unit disc. The recirculating flow in a recirculation wake is defined by considering the unit disc as a rigidly rotating body. Extended potential flow theory approximates local velocity vectors with an average error of 20% – 30% for a wide range of Reynolds numbers.

Extended potential flow theory approximates the separation line(s) with a small number of straight line segments, and the coordinates of the separation vertices are model parameters. Each recirculation wake can introduce four additional parameters, being the two coordinates of the vortex centre (m), the vortex strength (m^{2}s^{-1}) and the eccentricity. Using a nonlinear optimization algorithm, the parameters can be calculated such that the corresponding velocity field matches given velocity vectors. This way, extended potential flow theory is used as a tool to identify geometric characteristics of a given velocity field. There is a trade-off between the number of parameters, and the error of extended potential flow modelling, and the number of parameters can be varied to take this trade-off into account (resulting in a parsimonious model). In some cases, a limited number of given velocity vectors that are homogeneously distributed over the domain (only ten) suffices as reference data for parameter estimation. Therefore, velocity fields may be characterized also

from (physical) measurements. It can be concluded that the model parameters are physically meaningful, improving the applicability of extended potential flow theory.

Extended potential flow modelling can be used to analyse the impact of the system design on heat and mass transfer phenomena. A new model for the residence time distribution is obtained by neglecting diffusion and dispersion, which implies that every streamline has a fixed residence time. The new model predicts low velocities near convex corners of the main flow area (internal angle less than 180°), and high velocities near concave corners. The geometry of the boundary affects different streamlines in a different way, explaining that the residence time can be different for different streamlines. The residence time distribution can be calculated from the variation of the residence times. This model for the residence time distribution agrees with tracer experiments, and hence it can be used to model the impact of the system geometry on the residence time distribution. Furthermore, the model can calculate the travelling time from the inlet to each location in the system, which may be useful to analyse the spatial distribution of chemical reactions. Finally, the extended potential flow modelling can be applied to model the combination of convection and conduction. To do this, the geometric meaning of the model parameters is exploited by including them in a modified Reynolds number, effectively including the geometry of the velocity field. Nusselt – Reynolds correlations based on a modified Reynolds number outperform conventional Nu – Re correlations, demonstrating that the geometric characteristics are relevant for design purposes. From these applications, it can be concluded that extended potential flow modelling is useful for design purposes.

7.2   Recommendations

Firstly, software development is recommended to develop an interactive toolbox that allows application of extended potential flow modelling. This toolbox must allow the geometry to be designed interactively, including the placement of inlets, outlets and virtual boundaries. The toolbox will be able to show the velocity field, the potential lines, or the streamlines. The analysis of spatially-distributed chemical reactions will be supported by including contour plots showing the travelling time to each location, and by including the calculation of residence time distribution graphs. The applicability of the model can be enhanced by extending potential flow modelling to multiple sources and sinks, which is only a small modification of the theory developed in Chapter 4. Finally, the evaluation of power-law relations including the geometric characteristics will be supported, allowing analysis of the combination of convection and conduction.

In the present thesis, numerical evaluation of conformal maps is based on the

Schwarz-Christoffel theorem. The Schwarz-Christoffel theorem maps the polygonal regions to simple domains. However, round corners are important in reverse electrodialysis stacks, because gaskets with round corners are produced more easily than gaskets with sharp corners. To use the Schwarz-Christoffel theorem, round corners must be approximated with straight line segments. The calculation time increases with the number of line segments, and hence the number of line segments used to approximate round corners was limited, reducing the robustness of the model. Research is recommended about the impact of the number of line segments on the model accuracy. Alternatively, it can be investigated how round corners can be included in the model. This research may be based on the generalized Schwarz-Christoffel theorem (Floryan and Zemach, 1987).

Thirdly, the parameter estimation algorithm for the geometric characteristics is based on Sequential Quadratic Programming, which iteratively searches parameter values based on the gradient of the objective function. However, the derivative of the objective function is not supplied to the algorithm, and hence numerical differentiation is applied. As a consequence, many evaluations of extended potential flow modelling are required, causing long calculation times. Research is recommended to calculate the derivative of the objective function, because the number of model evaluations may be reduced. This research may result in a dramatic reduction of the calculation time needed for calibration of the geometric characteristics.

Fourthly, research is recommended to find additional equations for extended potential flow modelling that describe boundary layers and mixing layers. Modern models of boundary layers can already predict the separation point (Schlichting, 2000; Wilcox, 1998), and reduced models are already available for turbulent mixing layers (Wilcox, 1998). These models may be extended to predict the turning angle of a separation line. These enhancements may result in extra equations, reducing the number of unknown parameters. If the number of parameters is reduced, the number of model evaluations required during calibration is also reduced. This way, the calibration time can be reduced. In the future, a reduced model for the velocity field may be obtained without unknown parameters.

Fifthly, application of extended potential flow modelling in ongoing research on automatic monitoring and automatic control is recommended. In Speetjens et al. (2006), for example, a greenhouse is modelled. In that model, the parameters have a physical interpretation, and their values are found by online estimation. Dynamic changes of the parameters can be related to system changes, suggesting that online estimation of parameters can be used for automatic monitoring. Using extended potential flow modelling, on-line estimation of geometric characteristics of the velocity field may be possible. These characteristics are closely related to the system geometry, allowing automatic monitoring of changes of the system geometry; these changes

may for example indicate fouling in membrane-based systems. Automatic control of spatially distributed systems is also relevant for environmental systems (van Mourik et al., 2007). Currently, controllers are being designed based on local balances, which are expressed mathematically in partial differential equations. Extended potential flow modelling describes the velocity field based on ordinary differential equations, and provides geometric characteristics. These features may be used to find simpler methods for controller design.

Sixthly, research is recommended to extend geometric identification of velocity fields to three dimensions. Geometric identification applies conformal maps to transform regions of the flow domain to simplified domains. Two-dimensional regions of channel flow are mapped to the infinite strip, and monopolar vortices are mapped to the unit disc. Currently, fast algorithms are available to evaluate conformal maps of three-dimensional regions (Haker et al., 2000). These algorithms may be applied to identify three-dimensional flow patterns.

Finally, the parameters of lumped engineering models were calibrated with computational fluid dynamics results. In the present thesis, the aim was to investigate the lumped models. Further research on this modelling approach is recommended with the aim to simplify computational fluid dynamics modelling. For example, it is difficult to model a shell-and-tube heat exchanger driven by natural convection with CFD, because the flow is driven by buoyancy. The CFD model can be simplified by replacing the buoyant force in the model by a given pressure difference, allowing the drag coefficient and the heat transfer coefficient to be calculated more easily. Buoyancy effects may be modelled by substituting the parameter values in the lumped model.

Bibliography

Abu-Mulaweh, H. I., 2005. Turbulent mixed convection flow over a forward-facing step – the effect of step heights. International Journal of Thermal Sciences 44, 155–162.

Ameel, T. A., 1997. Average effects of forced convection over a flat plate with an unheated starting length. International Communications in Heat and Mass Transfer 24 (8), 1113–1120.

Awbi, H. B., 1998. Calculation of convective heat transfer coefficients of room surfaces for natural convection. Energy and Buildings 28, 219–227.

Balster, J., Pünt, I., Stamatialis, D. F., Wessling, M., 2006. Multi-layer spacer geometries with improved mass transport. Journal of Membrane Science 282 (1-2), 351–361.

Batchelor, G. K., 1967. An Introduction to Fluid Dynamics. Cambridge University Press.

Bosch, G., Rodi, W., 1998. Simulation of vortex shedding past a square cylinder with different turbulence models. International Journal for Numerical Methods in Fluids 28, 601–616.

Bot, G. P. A., 1983. Greenhouse Climate: From Physical Processes to a Dynamic Model. Ph.D. thesis, Wageningen University, Wageningen, the Netherlands.

Bot, G. P. A., 2001. Developments in indoor sustainable plant production with emphasis on energy saving. Computers and Electronics in Agriculture 30, 151–165.

Buchholz, M., 2006. Watergy, a system for water treatment, building climate control and food production. `www.watergy.info`.

Burnham, K. P., Anderson, D. R., 2002. Model Selection and Multimodel Inference. A Practical Information-Theoretic Approach, 2nd Edition. Springer.

Campen, J. B., Bot, G. P. A., de Zwart, H. F., 2003. Dehumidification of greenhouses at Northern latitudes. Biosystems Engineering 86 (4), 487–493.

Campen, J. C., Bot, G. P. A., 2003. Determination of greenhouse-specific aspects of ventilation using three-dimensional computational fluid dynamics. Biosystems Engineering 84 (1), 69–77.

Catton, I., 1978. Natural convection in enclosures. In: Proceedings of the 6th International Heat Transfer Conference, Toronto, Canada. Hemisphere Publishing, Washington D. C., pp. 13–31.

Chui, E. H., Raithby, G. D., 1993. Computation of radiant heat transfer on a non-orthogonal mesh using the finite-volume method. Numerical Heat Transfer, Part B 23, 269–288.

Conroy, L. M., Trevelyan, P. M. J., Ingham, D. B., 2000. An analytical, numerical, and experimental comparison of the fluid velocity in the vicinity of an open tank with one and two lateral exhaust slot hoods and a uniform crossdraft. Annals of Occupational Hygiene 44 (6), 407–419.

Cruchaga, M., Celentano, D., 2003. Modelling natural and mixed convection in obstructed channels. International Journal of Numerical Methods for Heat & Fluid Flow 13 (1), 57–85.

Daloglu, A., Ayhan, T., 1999. Natural convection in a periodically finned vertical channel. International Communications in Heat and Mass Transfer 26 (8), 1175–1182.

Darcovich, K., Dal-Cin, M. M., Ballèvre, S., Wavelet, J.-P., 1997. CFD-assisted thin channel membrane characterization module design. Journal of Membrane Science 124, 181–193.

de Graaf, S. C., 2006. Low Nitrate Lettuce Cultivations in Greenhouses – Optimal Control in the Presence of Measurable Disturbances. Ph.D. thesis, Wageningen University, Wageningen, the Netherlands.

de Lemos, M. J. S., Mesquita, M. S., 2003. Turbulent mass transport in saturated rigid porous media. International Communications in Heat and Mass Transfer 30 (1), 105–113.

Dirkse, M. H., van Loon, W. K. P., Stigter, J. D., Bot, G. P. A., 2005. A simple model for obstructed two-dimensional turbulent channel flow. In: Nowak, A. J., Bialecki, R. A., Węcel, G. (Eds.), Numerical Heat Transfer. Vol. 82. Institute of Thermal Technology, Silesian University of Technology, Gliwice, Poland, pp. 983–992.

Dirkse, M. H., van Loon, W. K. P., Stigter, J. D., Bot, G. P. A., 2007a. Modelling of natural-convection driven heat exchangers. In: Agricontrol 2007, 2nd IFAC International Conference on Modeling and Design of Control Systems in Agriculture. International Federation of Automatic Control, Osijek, Croatia, pp. 47–52.

Dirkse, M. H., van Loon, W. K. P., Stigter, J. D., Bot, G. P. A., 2007b. Understanding heat transfer in 2d channel flows including recirculation. International Journal of Thermal Sciences 46 (7), 682–691.

Dirkse, M. H., van Loon, W. K. P., van der Walle, T., Speetjens, S. L., Bot, G. P. A., 2006. A computational fluid dynamics model for designing heat exchangers based on natural convection. Biosystems Engineering 94 (3), 443–452.

Doeswijk, T. G., 2007. Reducing Prediction Uncertainty of Weather Controlled Systems. Ph.D. thesis, Wageningen University, Wageningen, the Netherlands.

Driscoll, T. A., 1996. Algorithm 756: A MATLAB toolbox for Schwarz-Christoffel mapping. ACM Transactions on Mathematical Software 22 (2), 168–186.

Driscoll, T. A., Toh, K.-C., Trefethen, L. N., 1998. From potential theory to matrix iterations in six steps. SIAM Review 40 (3), 547–578.

Floryan, J. M., Zemach, C., 1987. Schwarz-Christoffel mappings: A general approach. Journal of Computational Physics 72, 347–371.

Fluent Inc., 2007. `www.fluent.com`.

Gaskell, D. R., 1992. An Introduction to Transport Phenomena in Materials Engineering. Macmillan Publishing Company, New York, USA.

Ghidossi, R., Veyret, D., Moulin, P., 2006. Computational fluid dynamics applied to membranes: State of the art and opportunities. Chemical Engineering and Processing 45, 437–454.

Gigler, J., 2000. Drying of Willow Biomass in Supply Chains. Ph.D. thesis, Wageningen University, Wageningen, the Netherlands.

Golubitsky, M., Stewart, I., 2003. The Symmetry Perspective. Birkhäuser Verlag, Basel, Switzerland.

Griskey, R. G., 2002. Transport Phenomena and Unit Operations. John Wiley and Sons, New York.

Grubb, W. T., Niedrach, L. W., 1960. Batteries with solid ion-exchange membrane electrolytes .2. low-temperature hydrogen-oxygen fuel cells. Journal of the Electrochemical Society 107 (2), 131–135.

Gullapalli, V. S., Strömer, F., Pelletier, O., 2005. Component based performance analysis of compact brazed plate heat exchangers. In: Nowak, A. J., Bialecki, R. A., Węcel, G. (Eds.), Numerical Heat Transfer. Vol. 82. Institute of Thermal Technology, Silesian University of Technology, Gliwice, Poland, pp. 1015–1022.

Haker, S., Angenent, S., Tannenbaum, A., Kikinis, R., Sapiro, G., Halle, M., 2000. Conformal surface parametrization for texture mapping. IEEE Transactions on Visualization and Computer Graphics 6 (2), 181–189.

Hassenpflug, W. C., 1998. Branched channel free-streamlines. Computer Methods in Applied Mechanics and Engineering 159, 329–354.

Heron, S. F., Ridd, P. V., 2001. The use of computational fluid dynamics in predicting the tidal flushing of animal burrows. Estuarine, Coastal and Shelf Science 52, 411–421.

Hosseini, A. A. M., 2005. Quality, Energy Requirement and Costs of Drying Tarragon (Artemisia Dracunculus L.). Ph.D. thesis, Wageningen University, Wageningen, the Netherlands.

Hsu, C. T., Cheng, P., 1990. Thermal dispersion in a porous medium. International Journal of Heat and Mass Transfer 33 (8), 1587–1597.

Iyer, S. V., Vafai, K., 1997. Effects of a geometric perturbation on buoyancy induced flow and heat transfer in a cylindrical annulus. International Journal of Heat and Mass Transfer 40 (12), 2901–2911.

Jagur-Grodzinski, J., Kramer, R., 1986. Novel process for direct conversion of free energy of mixing into electric power. Industrial and Engineering Chemistry Process Design and Development 25, 443–449.

Kailath, T., 1980. Linear Systems. Prentice-Hall Information and System Sciences Series. Prentice-Hall, Inc.

Kays, W. M., Crawford, M. E., 1993. Convective Heat and Mass Transfer. McGraw-Hill Series in Mechanical Engineering. McGraw-Hill, New York.

Keener, J. P., 1988. Principles of Applied Mathematics: Transformation and Approximation. Addison-Wesley Publishing Company.

Kortram, R. A., 1989. De Theorie van Complexe Functies. Epsilon Uitgaven, Utrecht, the Netherlands.

Lacasse, D., Turgeon, É., Pelletier, D., 2004. On the judicious use of the k-ϵ model, wall functions and adaptivity. International Journal of Thermal Sciences 43, 925–938.

Levenspiel, O., 1972. Chemical Reaction Engineering, 2nd Edition. John Wiley and Sons, London, United Kingdom.

Liu, H.-C., Yan, W.-M., Soong, C.-Y., Chen, F., 2005. Effects of baffle-blocked flow channel on reactant transport and cell performance of a proton exchange membrane fuel cell. Journal of Power Sources 142, 125–133.

Murthy, J. Y., Mathur, S. R., 1998. A finite volume method for radiative heat transfer using unstructured meshes. Journal of Thermophysics and Heat Transfer 12 (3), 313–321.

Oberkampf, W. L., Trucano, T. G., 2002. Verification and validation in computational fluid dynamics. Progress in Aerospace Sciences 38, 209–272.

Olver, P. J., 1986. Applications of Lie Groups to Differential Equations, 2nd Edition. Graduate Texts in Mathematics. Springer-Verlag.

Öztürk, H. H., Başçetinçelik, A., 2003. Energy and exergy efficiency of a packed-bed heat storage unit for greenhouse heating. Biosystems Engineering 86 (2), 231–245.

Patankar, S. V., 1980. Numerical Heat Transfer and Fluid Flow. Series in Computational Methods in Mechanics and Thermal Sciences. Taylor & Francis, USA.

Paterson, A. R., 1983. A First Course in Fluid Dynamics. Cambridge University Press.

Peng, W., Smith, E. A., de Ville, A., 1999. Airflow and temperature distribution in two-dimensional drying bins. Journal of Engineering Mathematics 36, 241–254.

Perry, R. H., Green, D. W., 1997. Perry's Chemical Engineering Handbook, 7th Edition. McGraw-Hill Book Co-Singapore.

Post, J. W., Veerman, J., Hamelers, H. V. M., Euverink, G. J. W., Metz, S. J., K., N., Buisman, C. J. N., 2007. Salinity-gradient power: Evaluation of pressure-retarded osmosis and reverse electrodialysis. Journal of Membrane Science 288 (1-2), 218–230.

Quirijns, E. J., 2006. Modelling and Dynamic Optimisation of Quality Indicator Profiles During Drying. Ph.D. thesis, Wageningen University, Wageningen, the Netherlands.

Raithby, G. D., Chui, E. H., 1990. A finite-volume method for predicting a radiant heat transfer in enclosures with participating media. Journal of Heat Transfer 112, 415–423.

Reizes, J. A., Leonardi, E., 2005. Numerical and experimental investigations of laminar natural convective flows. In: Nowak, A. J., Bialecki, R. A., Węcel, G. (Eds.), Numerical Heat Transfer. Vol. 82. Institute of Thermal Technology, Silesian University of Technology, Gliwice, Poland, pp. 21–46.

Roberts, E. P. L., 1994. A numerical and experimental-study of transition processes in an obstructed channel flow. Journal of Fluid Mechanics 260, 185–209.

Roy, J. C., Boulard, T., Kittas, C., Wang, S., 2002. Convective and ventilation transfers in greenhouses, part 1: The greenhouse considered as a perfectly stirred tank. Biosystems Engineering 83 (1), 1–20.

Rubinstein, I., Pretz, J., Staude, E., 2001. Open circuit voltage in a reverse electrodialysis cell. Physical Chemistry Chemical Physics 3 (9), 1666–1667.

Saffman, P. G., 1992. Vortex Dynamics. Cambridge Monographs on Mechanics and Applied Mathematics. University of Cambridge.

Satijn, M. P., van Buren, M. G., Clercx, H. J. H., van Heijst, G. J. F., 2004. Vortex models based on similarity solutions of the two-dimensional diffusion equation. Physics of Fluids 16 (11), 3997–4011.

Schittowski, K., 1985. NLQPL: A FORTRAN-subroutine solving constrained nonlinear programming problems. Annals of Operations Research 5, 485–500.

Schlichting, H., 2000. Boundary Layer Theory. Springer-Verlag, Berlin Heidelberg, Germany.

Shilton, A., 2000. Potential application of computational fluid dynamics to pond design. Water Science and Technology 42 (10-11), 327–334.

Shilton, A., Wilks, T., Smyth, J., Bickers, P., 2000. Tracer studies on a New Zeeland waste stabilisation pond and analysis of treatment efficiency. Water Science and Technology 42 (10-11), 343–348.

Sinnott, R. K., 1996. Coulson & Richardson's Chemical Engineering. Vol. 6. Butterworth Heinemann, Oxford, United Kingdom.

Speetjens, S. L., van der Walle, T., van Straten, G., Janssen, H. J. J., Gieling, T. H., Stigter, J. D., 2004. Watergy, towards a closed greenhouse in semi-arid regions – experiment with a heat exchanger. In: van Straten, G., Bot, G. P. A., van Meurs, W. T. M., Marcelis, L. M. F. (Eds.), Proceedings of the International Conference on Sustainable Greenhouse Systems. International Society for Horticultural Science, Leuven, Belgium, pp. 845–852.

Speetjens, S. L., van Straten, G., Stigter, J. D., 2006. Adaptive model for greenhouse control. Computers and Electronics in Agriculture(Submitted).

Stephanopoulos, G., 1984. Chemical Process Control, an Introduction to Theory and Practice. Prentice-Hall, Inc., Englewood Cliffs, New Jersey, United States.

Stern, F., Wilson, R. V., Coleman, H. W., Paterson, E. G., 2001. Comprehensive approach to verification and validation of CFD simulations – part 1: Methodology and procedures. Journal of Fluids Engineering-Transactions of the ASME 123 (4), 793–802.

Ta, C. T., Brignal, W. J., 1998. Application of computational fluid dynamics technique to storage reservoir studies. Water Science and Technology 37 (2), 219–226.

Tanda, G., 1995. Experiments on natural-convection from 2 staggered vertical plates. International Journal of Heat and Mass Transfer 38 (3), 533–543.

Tap, F., 2000. Economics-Based Optimal Control of Greenhouse Tomato Crop Production. Ph.D. thesis, Wageningen University, Wageningen, the Netherlands.

the COMSOL Group, 2007. `www.comsol.com`.

the Math Works, 2006. `http://www.mathworks.com/`.

Trefethen, L. N., Driscoll, T. A., 1998. Schwarz-Christoffel mapping in the computer era. Documenta Mathematica Extra Volume ICM III, 533–542.

Trevelyan, P. M. J., Elliott, L., Ingham, D. B., 2000. Potential flow in a semi-infinite channel with multiple sub-channels using the Schwarz-Christoffel transformation. Computer Methods in Applied Mechanics and Engineering 189, 341–359.

van Henten, E. J., 1994. Greenhouse Climate Management: An Optimal Control Approach. Ph.D. thesis, Wageningen University, Wageningen, the Netherlands.

van Mourik, S., Zwart, H., Keesman, K. J., 2007. Switching control for post-harvest food storage. In: Agricontrol 2007, 2nd IFAC International Conference on Modeling and Design of Control Systems in Agriculture. International Federation of Automatic Control, Osijek, Croatia, pp. 189–194.

van Ooteghem, R. J. C., 2007. Optimal Control Design for a Solar Greenhouse. Ph.D. thesis, Wageningen University, Wageningen, the Netherlands.

VDI, 1988. VDI-Wärmeatlas: Berechnungsblätter Für Den Wärmeübergang, Fünfte, Erweiterte Auflage. Verlag des Vereins Deutscher Ingenieure.

Vincent, A., Meneguzzi, M., 1991. The spatial structure and statistical properties of homogeneous turbulence. Journal of Fluid Mechanics 225, 1–20.

Wilcox, D. C., 1998. Turbulence Modeling for CFD. DCW Industries, Inc, La Canada, California.

Wiley, D. E., Fletcher, D. F., 2003. Techniques for computational fluid dynamics modelling of flow in membrane channels. Journal of Membrane Science 211, 127–137.

Wilson, R. V., Stern, F., Coleman, H. W., Paterson, E. G., 2001. Comprehensive approach to verification and validation of CFD simulations – part 2: Application for RANS simulation of a cargo/container ship. Journal of Fluids Engineering-Transactions of the ASME 123 (4), 803–810.

Xia, K.-Q., Qiu, X.-L., 1999. Turbulent convection with "disconnected" top and bottom boundary layers. Europhysics Letters 46 (2), 171–176.

Young, P., Price, L., Berckmans, D., Janssens, K., 2000. Recent developments in the modelling of imperfectly mixed airspaces. Computers and Electronics in Agriculture 26, 239–254.

Young, P. C., Lees, M., 1993. The active mixing volume: A new concept in modelling environmental systems. In: Barnett, V., Turkman, K. F. (Eds.), Statistics for the Environment 2: Water Related Issues. John Wiley & Sons Ltd., Chichester, United Kingdom, Ch. 1, pp. 3–46.

Appendix A

Implementation issues on extended potential flow modelling

Notation

N	number of given velocity vectors in one reference velocity field
E	error of velocity field, ms^{-1}
$\vec{L}$	Lower bound for Sequential Quadratic Programming parameters
R	Residence time, s
$\vec{U}$	Upper bound for Sequential Quadratic Programming parameters
$a + i\,b$	complex derivative of projection of recirculation area to the disc, m^{-1}
$\vec{c}$	projection of source on upper half-plane
$\vec{d}$	projection of sink on upper half-plane
i	imaginary unit
k	summation variable
m	number of fitted degrees of freedom
n	number of separation vertices
q	velocity magnitude, ms^{-1}
$\vec{u}$	average velocity vector (2D), ms^{-1}
$\vec{v}$	vector of Sequential Quadratic Programming parameters
$\vec{x}$	extended potential flow modelling parameter that is a location, m
$\vec{y}$	coordinate vector in unified space
t	time, s
z	complex spatial coordinate, m
γ	contraction factor
ζ	complex coordinate of projection of main flow area
ξ	complex coordinate of projection of recirculation area
ϕ	potential function, $\mathrm{m}^2\mathrm{s}^{-1}$
ψ	stream function, $\mathrm{m}^2\mathrm{s}^{-1}$

Subscripts

$_D$	disc
$_{inj}$	injection
$_s$	strip

Superscripts

$^{(m)}$	maximum
$^{(r)}$	recirculation
$^{(s)}$	separation

A.1   Introduction

In Chapter 4 – Chapter 6, potential flow modelling is revisited and extended to calculate the velocity field. Extended potential flow modelling has geometric characteristics of the velocity field as its parameters. These parameters define a virtual boundary (separation line) that separates the circuit from the source to the sink (main flow area) from a recirculation area. The velocity field in the main flow area is modelled using potential flow theory. Four additional parameters characterise the velocity field in the recirculation area, and this velocity field is defined by an analytic expression (Chapter 5). Based on the parameter values, the velocity field can be evaluated. The parameters are iteratively adjusted to minimise the difference between the modelled velocity field, and a reference velocity field. This parameter estimation algorithm characterises given velocity fields with a limited number of geometric characteristics. Finally, extended potential flow modelling is used as a building block to calculate the residence time distribution.

The present Appendix focusses on the mathematical and numerical methods that are required for model evaluation and parameter estimation. Extended potential flow modelling was first applied in Chapter 5, and it was further developed during the research of Chapter 6. Therefore, the implementation of Chapter 6 is described. We do not claim that this implementation is optimal, so further research is recommended as stated in Chapter 7.

Extended potential flow modelling is based on conformal maps from polygonal domains to simple calculation domains (the infinite strip, the upper half-plane or the unit disc). The calculation is based on the Schwarz-Christoffel theorem, but the implementation of the calculation is complicated by the numerical problem of crowding (Driscoll, 1996; Trefethen and Driscoll, 1998). A robust implementation is presented to evaluate the velocity field. Parameter estimation is based on Sequential Quadratic Programming (Schittowski, 1985). The result of Sequential Quadratic Programming can depend on the initialisation of the algorithm. Furthermore, the geometric nature of the parameters causes the search space to be complicated. Implementation details are presented that addresses these issues. Finally, implementation details are given for the residence time distribution. Firstly, a modification of the analysis is explained that includes the impact of the injection time. Secondly, a numerical enhancement is outlined to reduce the calculation time.

A.2   Evaluation details of the velocity field

When the parameter values of extended potential flow modelling are given, the velocity in every location inside the geometry can be evaluated. The parameters

divide the calculation domain in two areas, being the main flow area and the recirculation area. Different equations are applied on these areas to calculate the velocity field. The velocity in the main flow area is calculated by potential flow theory, introducing a potential function ϕ and a stream function ψ (both m²s⁻¹) on the main flow area. The complex potential $\phi + i\,\psi$, with i the imaginary unit, is calculated as a conformal map from the main flow area to the infinite strip. The velocity vector (u_1, u_2) (ms⁻¹) on the main flow area is calculated using complex-valued differentiation:

$$u_1 - i\,u_2 = \frac{\mathrm{d}(\phi + i\,\psi)}{\mathrm{d}z} \tag{A.1}$$

with z the complex spatial coordinate (ms⁻¹).

There are two different cases for calculating the complex potential $\phi + i\,\psi$. If there are no internal sources and sinks, the function $\phi + i\,\psi$ is defined by two boundary conditions: $\psi = 0$ on the right channel boundary, and $\psi = \psi^{(m)}$ on the left channel wall with $\psi^{(m)}$ the area flow rate (m²s⁻¹). This conformal map is evaluated using a variation of the Schwarz-Christoffel theorem (Driscoll, 1996). If there are internal sources and sinks, the complex potential on the main flow area is evaluated using a conformal map to the upper half-plane ζ. In this case, the following formula (Chapter 4) can be used:

$$\phi + i\psi = \frac{\psi^{(m)}}{2\pi} \ln\left(\frac{(\zeta - c_1)^2 + c_2^2}{(\zeta - d_1)^2 + d_2^2}\right) \tag{A.2}$$

with $c_1 + i\,c_2$ the image of the source on the upper half-plane, and $d_1 + i\,d_2$ the image of the sink on the upper half-plane.

The velocity field in the recirculation area is based on a conformal map to the unit disc. The velocity field is modelled as a monopolar vortex, and extended potential flow modelling has four parameters that characterise this vortex. These parameters are the coordinates of the vortex centre $(x_1^{(r)}, x_2^{(r)})$, the vortex strength $\psi^{(r)}$, and the eccentricity $\gamma^{(r)}$. The velocity is evaluated as follows (Chapter 5):

$$(-u_2, u_1) = \psi^{(r)} \begin{pmatrix} -2\xi_1 & -2\xi_2 \end{pmatrix} \begin{pmatrix} a & -b \\ b & a \end{pmatrix} \begin{pmatrix} 1 & 0 \\ 0 & \gamma^{(r)} \end{pmatrix} \tag{A.3}$$

with ξ being a conformal map from the contracted recirculation area (vertical coordinate multiplied with $\gamma^{(r)}$) to the unit disc, and $a + i\,b$ (m⁻¹) being the complex derivative of the conformal map (Chapter 5).

The conformal maps included in *Eqns* (A.1) – (A.3), and the required derivatives of these maps, can be evaluated using the Schwarz-Christoffel toolbox programmed by Driscoll (1996). The toolbox can evaluate conformal maps to the unit strip, to the upper half-plane, and to the unit disk. However, mapping elongated regions to the upper half-plane is complicated by the numerical problem of crowding (Driscoll, 1996; Trefethen and Driscoll, 1998), especially if the mapped region has many vertices.

Therefore, direct evaluation of *Eqn.* (A.2) was not feasible for the calculations of Chapter 4 and Chapter 6.

Two solutions for this problem were applied. The first solution was mentioned already in Chapter 4. The main flow area is mapped to the unit strip ζ_s, and the velocity field *Eqn.* (A.1) is evaluated using the substitutions:

$$\zeta = \exp(\pi\,\zeta_s) \tag{A.4}$$

$$\frac{\mathrm{d}\zeta}{\mathrm{d}z} = \frac{\mathrm{d}\zeta}{\mathrm{d}\zeta_s}\frac{\mathrm{d}\zeta_s}{\mathrm{d}z} = \pi\,\exp(\pi\,\zeta_s)\,\frac{\mathrm{d}\zeta_s}{\mathrm{d}z} \tag{A.5}$$

The second solution is to apply Cross-Ratio Delaunay Triangulation (CRDT) (Driscoll, 1996; Trefethen and Driscoll, 1998), which also is implemented in the Schwarz-Christoffel toolbox. This method is only available for conformal maps to the unit disc. Therefore, a conformal map based on CRDT from a polygonal domain to the upper half-plane, requires a conformal map from the unit disc ζ_D to the upper half-plane. This mapping is a Möbius transformation (Kortram, 1989), resulting in the substitutions:

$$\zeta = -i\frac{\zeta_D - 1}{\zeta_D + 1} \tag{A.6}$$

$$\frac{\mathrm{d}\zeta}{\mathrm{d}z} = \frac{\mathrm{d}\zeta}{\mathrm{d}\zeta_D}\frac{\mathrm{d}\zeta_D}{\mathrm{d}z} = \frac{-2i}{(\zeta_D + 1)^2}\frac{\mathrm{d}\zeta_D}{\mathrm{d}z} \tag{A.7}$$

The equation (A.6) and (A.7) are evaluated correctly only if $\mathrm{d}\zeta_D/\mathrm{d}z$ is insensitive to numerical errors. Fortunately, a mapping from the main flow area to a disk is not defined uniquely. The location in the main flow area that is mapped to the centre of the disk ζ_D can be chosen freely. Furthermore, *Eqns.* (A.6) and (A.7) are valid for every choice of the mapping $z \rightarrow \zeta_D$. Numerical problems were avoided by evaluating different regions of the main flow area with different choices for the mapping $z \rightarrow \zeta_D$.

A.3   Implementation details of parameter estimation

The parameters of extended potential flow modelling are estimated using Sequential Quadratic Programming. The separation line is approximated with straight line segments, which are defined by a number n of separation vertices $\vec{x}^{(s,1)} \dots \vec{x}^{(s,n)}$. The other model parameters are the four characteristics of the recirculation area, being $x_1^{(r)}, x_2^{(r)}, \psi^{(r)}$ and $\gamma^{(r)}$. These parameters are calibrated against N given velocity vectors $(\tilde{u}_1^{(1)}, \tilde{u}_2^{(1)}) \dots (\tilde{u}_1^{(N)}, \tilde{u}_2^{(N)})$, which apply to the locations $z^{(1)}, \dots z^{(n)}$. Let $(u_1^{(1)}, u_2^{(1)}) \dots (u_1^{(N)}, u_2^{(N)})$ be the (parameter dependent) modelled velocity vectors evaluated in the same locations $z^{(1)} \dots z^{(n)}$ (using *Eqns.* A.1 and A.3). The model

error E is defined to be:

$$E\left(\vec{x}^{(s,1)} \ldots \vec{x}^{(s,n)} x_1^{(r)}, x_2^{(r)}, \psi^{(r)}, \gamma^{(r)}\right) = \sqrt{\sum_{k=1}^{N} \sum_{j=1}^{2} \left(u_j^{(k)} - \tilde{u}_j^{(k)}\right)^2} \qquad (A.8)$$

In some locations, the velocity cannot be calculated due to numerical problems, and large error values are obtained near singularities. The corresponding terms in *Eqn.* (A.8) are truncated.

The parameter estimation problem is to find the parameter values (geometric characteristics) that minimise the error E (*Eqn.* A.8). However, the velocity field is only defined if the separation vertices $\vec{x}^{(s,1)} \ldots \vec{x}^{(s,n)}$ divide the calculation domain in a main flow area and a recirculation area. This requirement implies that $\vec{x}^{(s,1)}$ and $\vec{x}^{(s,n)}$ are located on the domain boundary. Furthermore, the separation line may not cross itself, and it may not cross the boundaries of the calculation domain. The velocity field in the recirculation area is only defined if the vortex centre $(x_1^{(r)}, x_2^{(r)})$ is indeed located within the recirculation area. These requirements constitute complicated constraints for the parameter estimation algorithm. The programming language MatLab (the Math Works, 2006) supports Sequential Quadratic Programming, and a dedicated subroutine is available to minimise a sum-of-squares expression like *Eqn.* (A.8). This method only supports box constraints for the function arguments.

Parameter estimation based on Sequential Quadratic Programming is implemented as follows. The error E (*Eqn.* A.8) is written as a function of m variables $v_1 \ldots v_m$ with m the degrees of freedom to be fitted. Furthermore, some boundary conditions $L_k \leq v_k \leq U_k$, with $k = 1 \ldots m$, are established. The parameter estimation algorithm can transform each selection $v_1 \ldots v_m$ to valid parameters of extended potential flow modelling, being a set of separation vertices $\vec{x}^{(s,1)} \ldots \vec{x}^{(s,n)}$ and the vortex characteristics $x_1^{(r)}, x_2^{(r)}, \psi^{(r)}$ and $\gamma^{(r)}$. The parameter estimation algorithm calls the SQP-subroutine to iteratively choose $v_1 \ldots v_m$. Each choice corresponds to parameter values of extended potential flow modelling, and this allows the parameter estimation algorithm to produce a model error E (*Eqn.* A.8).

Three methods are applied to transform the SQP parameters $v_1 \ldots v_m$. Firstly, the geometry of the calculation domain is simplified by mapping it to the infinite strip (unified space), transforming the separation vertices $\vec{x}^{(s,1)} \ldots \vec{x}^{(s,n)}$ to some vectors $\vec{y}^{(s,1)} \ldots \vec{y}^{(s,n)}$. The requirement that $\vec{x}^{(s,1)}$ and $\vec{x}^{(s,n)}$ must be on the domain boundary, reduces to the constraints $y_2^{(s,1)} = 0$ and $y_2^{(s,n)} = 0$ (if the recirculation area is to the right, as is the case in Chapter 6; recirculation areas to the left give constraints $y_2^{(s,1)} = 1$ and $y_2^{(s,n)} = 1$). The requirement that the separation line may not cross itself, can be implemented by requiring $y_1^{(s,1)} < \ldots < y_1^{(s,n)}$.

The second transformation takes the first n SQP variables $v_1 \ldots v_n$ to a set of

ordered $y_1^{(s,1)} \dots y_1^{(s,n)}$ as:

$$y_1^{(s,k)} = y_1^{(s,k-1)} + v_k \left(y_1^{(s,n+1)} - y_1^{(s,k-1)} \right) \qquad k = 1 \dots n \qquad \text{(A.9)}$$

which requires boundaries $y_1^{(s,0)}$ and $y_1^{(s,n+1)}$ to be established beforehand.

The last transformation transforms v_{m-1} and v_m to a valid location for the recirculation centre. The coordinates are defined in unified space (the y-plane), where the coordinates are $(y_1^{(r)}, y_2^{(r)})$. A coordinate system is established on the recirculation area by transforming it to the unit disc. The SQP-variables v_{m-1} and v_m are interpreted as the polar coordinates on the unit disc. Therefore $y_1^{(r)}$ and $y_2^{(r)}$ are evaluated from a conformal map from the unit disc to the projection of the recirculation area in unified space.

These three transformations allow for proper boundary conditions for Sequential Quadratic Programming, but the solution still depends on the initialisation. Therefore, the algorithm was run for ten random initialisations, and the best solution was chosen.

A.4 Implementation details on the residence time distribution

Extended potential flow modelling can be used as a building block to calculate the residence time distribution. The model neglects diffusion and dispersion, and hence every streamline ψ has a fixed residence time $R(\psi)$. The residence time can be evaluated with a quadrature (Chapter 4):

$$R(\psi) = \int_{-\infty}^{\infty} \frac{\mathrm{d}\phi}{q(\phi, \psi)^2} \qquad \text{(A.10)}$$

with q the velocity magnitude (ms^{-1}). Equation (A.10) can be evaluated quickly, because there is an analytic expression for q (Chapter 4). The residence time distribution is calculated by analysing the residence time for different streamlines. For an impulse input signal, the residence time distribution is obtained by differentiating the cumulative residence time distribution, but in Chapter 6 there was reference data that was based on block input, requiring a small modification of the model.

When there is a block input signal, the relative inflow concentration is 1 during an injection period t_{inj} (s) and zero after that period. In this case, the residence time distribution can be analysed by considering the outflow concentration for a particular streamline. The relative outflow concentration can only be zero or one, because the concentration is only governed by convection along the streamline. The outflow concentration on a streamline ψ is one only when the particles inserted during the injection period are arriving. These particles arrive in the period between $R(\psi)$

and $R(\psi) + t_{inj}$, and therefore the relative outflow concentration of the streamline ψ equals the indicator function $1_{\{(t,\psi)|R(\psi)\leq t\leq R(\psi)+t_{inj}\}}$. The outflow concentration at a time t is found by averaging this indicator function over the different streamlines ψ.

Evaluating the residence time distribution requires the stream function ψ to be solved from the equation $R(\psi) = t$. This equation was solved by an iterative algorithm that requires multiple evaluates $R(\psi)$. This algorithm must be run for many values of t, and hence calculating the residence time distribution requires many evaluations of $R(\psi)$. Therefore, a fast algorithm is required to evaluate $R(\psi)$. In Chapter 4, a lookup table with about 100 entries was created, and $R(\psi)$ could be approximated accurately using a spline interpolation based on this table. The calculation time of this interpolation was significantly smaller than the evaluation time of the quadrature *Eqn.* (A.10).

Most residence time distributions of this thesis were calculated using lookup tables, but the exceptions are the residence time distributions presented in *Fig.* 6.9. For some geometries, our implementation of the creation of lookup tables failed due to numerical problems, which could be avoided by returning to the evaluation of quadratures. We believe that these numerical problems can be solved by a small programming effort.

Summary

In many environmental and agricultural systems, processes of heat and mass transfer play an important role. To design these systems, models are required that predict the impact of design decisions. Typically, these models are found by identifying subsystems. Lumped model equations for the interactions between the subsystems can be developed based on the literature, where models of many archetypical systems are described. Lumped models have short calculation times and they are relatively easy to develop, but there are drawbacks. First, new designs in environmental and agricultural engineering may not be covered by existing lumped equations. Second, lumped models are based on strong geometry simplification, and hence lumped models are not the appropriate tool to examine the impact of the geometry. Computational fluid dynamics (CFD) modelling is a modelling method for spatially distributed systems that addresses these drawbacks. Computational fluid dynamics modelling is based on local heat, mass and momentum balances. Using a mesh, the local balances are approximated by a large set of algebraic equations. These algebraic relations are solved numerically by an iterative algorithm. Computational fluid dynamics modelling generally requires long calculation times and expert knowledge is required to get accurate results. A third modelling method, potential flow theory, is a promising alternative that directly relates the system geometry to the velocity field. However, potential flow geometry assumes that the streamlines from the inlet to the outlet fill the entire system. In general, a two-dimensional flow is a combination of a main flow and adjacent recirculation wakes.

The following research questions are investigated:

1. To which extent can lumped engineering models be applied to design spatially distributed environmental and agricultural systems?

2. How can computational fluid dynamics models be applied efficiently to design spatially distributed environmental and agricultural systems?

3. Can potential flow theory be adapted to analyse general flow problems including a main flow and recirculation wakes?

4. How can this method be utilized for environmental and agricultural

engineering?

As an example system for CFD modelling, a model was created for the design of a heat exchanger driven by natural convection, which was intended to be used in an experimental greenhouse. It was a shell-and-tube heat exchanger with baffles (Chapter 2). The flow regime proved to be turbulent and this was modelled using the k-ω turbulence model. The features of the complex geometry were simplified considerably resulting in an almost two-dimensional mesh with only 30,000 mesh cells. The effect of black body radiation was investigated. The modelling results were validated experimentally and a model neglecting the effect of radiation turned out to be sufficiently accurate, reducing calculation times with a factor 60 to about eight minutes. Different meshes were used to check if the solution did not depend on the mesh chosen.

The measurements and the model indicated that the cross-flow caused by the baffles improved the heat flux dramatically. Based on model calculations on possible design alternatives, some additional design recommendations could be formulated. The heat transfer coefficient is insensitive to changes of the system geometry, and hence base area can be used more efficiently by reducing the shell width compared to the experimental system. Secondly, the water flow rate must not be too high, because a high water flow requires more pumping pressure and the impact on the heat flux is limited. Furthermore, a high water flow rate reduces the difference between the inflow and outflow water temperatures, reducing the possibility to reuse the outflow water.

In Chapter 3, a new lumped model was developed for the same heat exchanger, which is a spatially distributed system. The heat flux from the tube-side to the shell-side is proportional to the logarithmic mean temperature difference, but this model is not sufficient because the air flow in the shell is also driven by the temperature distribution. A lumped equation was developed by approximating the system as a one-dimensional channel flow. This approximation models the local air and water temperatures with two coupled ordinary differential equations, allowing for an analytic solution of the average air temperature, which is expressed as a function of the inflow and outflow temperatures of the air and water flows. The average air temperature determines the buoyant force, and a steady state is obtained when the buoyant force equals the friction force. The friction force is determined by the air flow rate, and therefore the analysis extends the existing theory on heat exchangers with a relation between the air flow rate and the inflow and outflow temperatures of the air and water flows. For given inflow temperatures and a given water flow, the heat flux can be predicted within 9% error bounds and the air flow rate within 18% error bounds relative to experimental data. The model has only two parameters,

being the heat transfer coefficient and the drag coefficient.

The lumped model was calibrated and validated using the CFD model results of Chapter 2 and experimental data. The heat transfer coefficient was the same for all investigated geometries, but the drag coefficient was different for different geometries. It was demonstrated that the drag coefficient per chamber (area between baffles) has less variation than the drag coefficient: the drag coefficient per chamber deviated at most 35% from the average over all examined geometry variations. Therefore, the model can give a rough estimate of the heat flux and the volumetric air flow regardless of the geometry.

Potential flow theory was worked out first for main flow only. In Chapter 4, a simplified reverse electrodialysis cell (no spacer) was investigated. It was modelled using potential flow theory, which calculates the velocity field based on a conformal map to the infinite strip. A new formula was required for this conformal map, because there were internal sources and sinks (the inlet and the outlet were not located on the boundary). The model was validated against experimental measurements of the local pressure. The Reynolds number was maximally 500, and hence further research was required to extend the model to higher Reynolds numbers. For medium-Reynolds-number flow ($500 < \mathrm{Re} < 2000$), the flow is still laminar, and it was modelled in Chapter 6 by dividing the flow in a main flow and adjacent recirculation wakes. The separation line was approximated with a small number of straight line segments. The main flow was modelled based on a conformal map to the infinite strip, but the recirculation wake was modelled as a stagnant zone (velocity zero). This extension of potential flow modelling was validated by comparison with CFD modelling results as the reference. Computational fluid dynamics modelling results instead of physical experiments were used as the reference, because CFD modelling allows more geometry variations to be investigated. The CFD models were two-dimensional, and therefore dispersion was not included in the reference data.

Extended potential flow modelling was also investigated for highly turbulent flow based on the example of flow through an obstructed channel (Chapter 5). In this case, the flow in a recirculation wake is driven by turbulent momentum transport, and therefore the velocity magnitude is not negligible there. The velocity field in a recirculation wake was modelled based on a conformal map from the recirculation wake to the unit disc, which was considered as a rigidly rotating body. Rigid rotation of the unit disc implies that the stream function is a square expression of the radial coordinate, and the velocity field follows from differentiating the stream function using the chain rule. Extended potential flow modelling for highly turbulent flow was also validated by comparison with CFD modelling results. Many mesh cells were required near the separation lines, because large velocity gradients were expected there. The number of mesh cells was reduced by applying dynamic grid adaptation,

which means that the grid was refined during the iterative calculation.

Extended potential flow modelling has unknown parameters. The line segments of the separation line are determined by the end points (separation vertices), and their coordinates are unknown parameters. For turbulent flows, the velocity field in each recirculation wake is determined by four additional parameters, being the two coordinates of the vortex centre, the vortex strength and the eccentricity. Both for medium-Reynolds-number laminar flow (Chapter 6) and turbulent flow (Chapter 5), the parameters were calibrated for variations of the geometry and the Reynolds number. In both cases, the reference velocity fields obtained from CFD modelling were reduced to approximately 1000 velocity vectors to reduce the computation time required for calibration. The number of parameters was varied to examine the trade-off between the number of parameters and the model error, and this way the optimal number of parameters could be determined.

In the example of turbulent flow, the optimal number of parameters was nine, but only three parameters appeared to be sensitive to the examined system variations. These three parameters were the width of the recirculation area behind the obstacle, the horizontal coordinate of the vortex centre (the channel was oriented vertically), and the vortex strength. These three parameters were recalculated while average values were assumed for the other six parameters. The three parameters could also be calculated using only ten given velocity vectors, suggesting that the parameters can be calibrated from physical measurements.

Two methods were examined to utilize potential flow theory for design purposes. Firstly, extended potential flow modelling was used as a building block for a reduced model for the residence time distribution (RTD). This reduced model neglects diffusion and dispersion, and hence every streamline has a fixed residence time. The RTD follows from the variation of the residence time over different streamlines. When there is a combination of main flow and recirculation wakes, only the main flow area is relevant for the RTD because diffusion to the recirculation wakes is neglected. For creeping flows (Re < 500), the model was validated with tracer experiments. For medium-Reynolds-number flow (Reynolds number between 500 and 2000), the model was validated with dynamic CFD calculations as the reference. The model can be used to analyse the impact of the two-dimensional geometry on the RTD, but the model can also calculate the travelling time from the inlet to each location in the system. This way, the model can be used to analyse the spatial distribution of chemical reactions.

Secondly, the parameters of extended potential modelling are physically meaningful. The heat flux from the two walls of the obstructed channel was modelled with modified Nusselt-Reynolds correlations. These correlations were developed separately for the wall next to the main flow and the wall next to a recirculation wake, because

there are different flow patterns in the main flow area and in the recirculation wake. Reference data for these models was obtained by including heat transfer to the reference CFD model. This way, a new model was found for the heat flux from a wall bounding a vortex, which has an error of 7%. It was also demonstrated that the modified Nusselt-Reynolds correlations outperform a conventional Nusselt-Reynolds correlation, demonstrating the relevance of the parameters of extended potential flow modelling for design.

It has been concluded that new lumped engineering models for spatially distributed systems can be developed by approximating the flow pattern as flow through a straight channel, even when the flow is in reality a combination of a main flow and recirculation wakes. Lumped models can be used to analyse a specific system geometry, or they give a rough approximation that is valid regardless the geometric details. However, lumped models are not the appropriate tool to analyse the impact of the detailed geometric design, because there are unknown parameters that must be calibrated separately for every geometry. The impact of the geometric design can be analysed by CFD models, and careful mesh design allows for surprisingly fast CFD models. However, expert knowledge is required to design the mesh such that the numerical algorithm converges for a buoyancy-driven flow. Furthermore, expert knowledge is required to avoid false diffusion.

It has been concluded that extended potential flow modelling is a fast method to evaluate velocity fields including a main flow and recirculation wakes. The method approximates local velocity vectors with an average error of 20% – 30% for a wide range of Reynolds numbers. Two ways to utilize extended potential flow modelling were developed. First, extended potential flow modelling can be used as a building block of a reduced model for the residence time distribution. Second, the parameters of extended potential flow modelling are physically meaningful, and hence potential flow theory can be applied as a model identification tool.

Samenvatting

Warmte- en stofoverdracht spelen een belangrijke rol in de milieukunde en agrotechniek. Om deze systemen te ontwerpen, zijn modellen nodig die de consequenties van ontwerpbeslissingen voorspellen. Deze modellen bestaan vaak uit deelsystemen, die beschreven zijn in de literatuur. Simpele modelvergelijkingen kunnen worden gevonden door de beschikbare kennis over de deelsystemen te combineren. Deze eenvoudige modellen kunnen in het algemeen snel worden doorgerekend en zijn relatief makkelijk te ontwikkelen, maar ze hebben ook nadelen. Het kan zijn dat nieuwe ontwerpen deelsystemen bevatten die nog niet eerder zijn onderzocht. Verder berusten deze modellen op een sterke versimpeling van de geometrie van het systeem. Daarom zijn deze modellen niet geschikt om de invloed van geometrische details te onderzoeken. Computational Fluid Dynamics (CFD) is een modelleringsmethode die deze twee nadelen ondervangt. De methode is gebaseerd op locale warmte-, massa- en impulsbalansen, die door middel van een rooster benaderd worden met een groot stelsel van algebrasche vergelijkingen. Het stelsel wordt numeriek opgelost met een iteratief algoritme. Daarom hebben CFD modellen veel rekentijd nodig, en er is veel kennis nodig om accurate resultaten te verkrijgen. De derde methode die in dit proefschrift is onderzocht is potentiaaltheorie, een interessant alternatief dat het snelheidsveld direct relateert aan de geometrie en rekenkundig veel efficiënter is. Potentiaaltheorie gaat ervan uit dat de stroomlijnen van de instroomopening naar de uitstroomopening het hele systeem bedekken. Vaker zijn tweedimensionale stromingen een combinatie van een hoofdstroom en recirculatiegebieden en dit wordt niet volledig door de theorie beschreven.

De volgende onderzoeksvragen zijn in dit proefschrift onderzocht:

1. In hoeverre kunnen simpele modellen gebruikt worden om ruimtelijk verdeelde, inhomogene systemen te ontwerpen?

2. Hoe kan CFD modellering efficiënt worden gebruikt bij het ontwerpen van ruimtelijk inhomogene systemen?

3. Kan potentiaaltheorie worden aangepast om algemene tweedimensionale stromingen met een hoofdstroom en recirculatiegebieden te onderzoeken?

4. Hoe kan zo'n methode worden benut voor milieukundige en agrotechnische toepassingen?

Als voorbeeld is een CFD model gemaakt van een warmtewisselaar met alleen vrije convectie. Deze warmtewisselaar was bedoeld voor gebruik in een experimentele kas. Het betrof een buizenwarmtewisselaar met dwarsschotten in de mantel (zie hoofdstuk 2). De stroming was turbulent, en daarom is het k-ω turbulentiemodel toegepast. De geometrie is aanzienlijk versimpeld, zodat een bijna tweedimensionaal rooster van ongeveer 30 000 cellen gebruikt kon worden. Het effect van warmtestraling is onderzocht door modellen met en zonder warmtestraling erin te vergelijken. De modelresultaten zijn gevalideerd met experimentele resultaten, en een model zonder warmtestraling bleek voldoende accuraat te zijn. Door warmtestraling uit het model te laten kon de rekentijd met een factor 60 worden gereduceerd tot ongeveer acht minuten. Er zijn verschillende roosters geprobeerd om te verifiëren dat de uitkomst van het model rooster onafhankelijk is.

Het model laat zien dat de schotten een dwarsstroming veroorzaken, die zorgt voor een drastisch verhoogde warmteflux. Toepassing van het model op mogelijke alternatieven voor de experimentele opstelling heeft verdere aanbevelingen opgeleverd. De warmteoverdrachtscoëfficiënt wordt nauwelijks benvloed door wijzigingen in de geometrie, en daarom kan het beschikbare grondoppervlak in een kas efficiënter worden benut door de warmtewisselaar minder breed te maken. Verder is het beter om het debiet van de waterstroming door de buisjes niet te hoog in te stellen, omdat dit weinig bijdraagt aan de warmteflux en meer pompdruk vereist. Verder vermindert een hoog waterdebiet het temperatuurverschil tussen het instromende en het uitstromende water, zodat het afgekoelde water minder goed hergebruikt kan worden.

De warmtewisselaar is ruimtelijk niet homogeen, maar in hoofdstuk 3 is toch een simpel model voor de warmtewisselaar ontwikkeld. De warmteflux is evenredig met het logaritmisch gemiddeld temperatuurverschil. Dit gegeven is niet voldoende voor een compleet model omdat de luchtsnelheid in de mantel ook door het temperatuurveld wordt bepaald. Een extra vergelijking is gevonden door de buizen en de mantel beide voor te stellen als een recht kanaal. Deze versimpeling maakt het mogelijk om de lucht- en waterstromingen met twee gekoppelde gewone differentiaalvergelijkingen te modelleren. In dit proefschrift is een analytische oplossing voor de gemiddelde luchttemperatuur gevonden, die wordt gerelateerd aan de in- en uitstroom temperaturen van de lucht en het water. De gemiddelde luchttemperatuur bepaalt de opwaartse kracht. De luchtstroming is stationair als de opwaartse kracht precies tegengesteld is aan de wrijvingskracht. Deze laatste is weer afhankelijk van de luchtsnelheid. Deze analyse breidt de bestaande theorie over

warmtewisselaars dus uit met een relatie tussen de luchtsnelheid enerzijds en de in- en uitstroomtemperaturen anderzijds. Voor gegeven instroomtemperaturen van de lucht en het water en voor een gegeven debiet van de waterstroming kan de warmteflux met 9% fout en de luchtsnelheid met 18% fout worden berekend in vergelijking met experimentele data. Het simpele model heeft maar twee parameters, namelijk de warmteoverdrachtscoëfficiënt en de wrijvingscoëfficiënt.

Het simpele model voor de warmtewisselaar is gekalibreerd en gevalideerd met de CFD modelresultaten uit hoofdstuk 2 en met experimentele data. De warmteoverdrachtscoëfficiënt was gelijk voor alle onderzochte geometrie variaties, maar de wrijvingscoëfficiënt is verschillend voor verschillende geometrien. De wrijvingscoëfficiënt per kamer (gebied tussen twee schotten) week maximaal 35% af van het gemiddelde over alle onderzochte geometrieën. Het model kan daarom een ruwe schatting berekenen van de warmteflux en de luchtsnelheid, onafhankelijk van geometrische details.

De belangrijkste methode die in het proefschrift wordt uitgewerkt is de toepassing en uitbreiding van potentiaaltheorie. De theorie is eerst uitgewerkt voor de klassieke situatie met alleen een hoofdstroomgebied. In hoofdstuk 4 is een gesimplificeerde omgekeerde elektrodialyse cel (geen spacer) onderzocht. Met behulp van potentiaaltheorie is het snelheidsveld berekend op basis van een conforme afbeelding op de oneindige strip. Voor deze transformatie moest een nieuwe formule worden afgeleid, omdat er interne bronnen en putten waren (de instroomopening en de uitstroomopening waren niet aan de rand). Het model is gevalideerd met experimentele metingen van de lokale druk. Het Reynolds getal was maximaal 500, zodat er verder onderzoek nodig was om het model uit te breiden naar hogere Reynolds getallen. De reeds bestaande beschrijving van een hoofdstroom werd uitgebreid met een model voor recirculatiegebieden.

Voor stromingen met gemiddeld Reynolds getal ($500 < \mathrm{Re} < 2000$) is de stroming laminair. In hoofdstuk 6 zijn deze stromingen gemodelleerd door het systeem virtueel te verdelen in een hoofdstroom en recirculatiegebieden. De grenslijn is benaderd met een klein aantal rechte lijnstukken. De hoofdstroom is berekend door het hoofdstroomgebied conform af te beelden op de oneindige strip, maar het recirculatiegebied is gemodelleerd door de snelheid te verwaarlozen. Deze uitbreiding van potentiaaltheorie is gevalideerd met CFD modelresultaten als referentie. De keuze voor CFD resultaten als referentie in plaats van experimenten is gemaakt omdat met CFD modellering meer geometrie variaties onderzocht kunnen worden. Deze methode wordt verder de Uitgebreide Potentiaaltheorie genoemd.

Voor hoog turbulente stroming is de Uitgebreide Potentiaaltheorie onderzocht voor een kanaal met obstakels (hoofdstuk 5). In dit geval wordt de stroming in recirculatiegebieden veroorzaakt door turbulente impulsoverdracht. De snelheid in

recirculatiegebieden is daarom niet verwaarloosbaar. Dit snelheidsveld is gemodelleerd op basis van een conforme afbeelding van een recirculatiegebied naar de eenheidsschijf. De eenheidsschijf is gemodelleerd als een roterend vast lichaam, wat inhoudt dat de stroomfunctie een kwadratische functie van de radiale coördinaat is. Het snelheidsveld wordt uitgerekend door de formule voor de stroomfunctie met de kettingregel te differentiëren. Uitgebreide Potentiaaltheorie voor hoog turbulente stroming is ook gevalideerd met CFD resultaten. Er was een rooster nodig met veel cellen omdat er hoge snelheidsgradiënten verwacht werden in de buurt van de scheidingslijn. Het aantal cellen kon wel verminderd worden door het rooster tijdens het rekenproces aan te passen (dynamic grid adaption).

De Uitgebreide Potentiaaltheorie heeft een klein aantal onbekende parameters. Deze parameters hebben allemaal een fysische betekenis. De lijnsegmenten van de scheidingslijn worden bepaald door hun eindpunten (scheidingspunten), en de coördinaten van deze scheidingspunten zijn onbekende parameters. Voor turbulente stroming wordt het snelheidsveld in een recirculatiegebied bepaald door vier extra parameters, namelijk de twee coördinaten van het centrum van de wervel, de wervelsterkte en de excentriciteit van de wervel. Zowel voor stromingen met gemiddeld Reynolds getal (hoofdstuk 6) als voor hoog turbulente stroming (hoofdstuk 5) zijn de parameters gekalibreerd voor geometrievariaties en voor variaties van het Reynolds getal. In beide gevallen zijn de snelheidsvelden die als referentie gebruikt zijn, gereduceerd tot ongeveer 1000 snelheidsvectoren. Op deze manier kon de rekentijd van het kalibreren worden verminderd. Het aantal modelparameters dat gekalibreerd werd is gevarieerd om het verband te onderzoeken tussen het aantal parameters in het model en de fout in de modelvoorspelling. Op deze manier kon een optimale keuze voor de te gebruiken parameters worden gemaakt.

In het geval van turbulente stroming was het optimale aantal parameters negen. Er waren echter maar drie parameters die gevoelig waren voor de onderzochte systeemvariaties. Deze drie parameters waren de breedte van het recirculatiegebied achter een obstakel, de horizontale coördinaat van het centrum van de wervel (het kanaal was verticaal georiënteerd), en de wervelsterkte. Deze drie parameters zijn opnieuw gekalibreerd waarbij de andere zes parameters werden vastgezet op hun gemiddelde waarde. Omdat de drie variabele parameters ook gekalibreerd konden worden tegen slechts tien gegeven snelheidsvectoren, is kalibratie met een gering aantal experimentele data mogelijk.

Vervolgens zijn er twee manieren onderzocht om potentiaaltheorie toe te passen. Ten eerste is potentiaaltheorie als bouwsteen gebruikt van een gereduceerd model voor de verblijftijdspreiding. Dit model verwaarloost diffusie en dispersie, zodat elke stroomlijn een vaste verblijftijd heeft. De verblijftijdspreiding volgt uit de variatie van de verblijftijden van de verschillende stroomlijnen. Voor combinaties

van een hoofdstroom en recirculatiegebieden wordt alleen het hoofdstroomgebied meegenomen in de berekening van de verblijftijdspreiding, omdat diffusie naar de recirculatiegebieden kan worden verwaarloosd. Voor kruipstroming (Re < 500) is het model gevalideerd met tracer-experimenten. Voor stromingen met gemiddeld Reynolds getal (500 < Re < 2000) is het model gevalideerd tegen dynamische CFD berekeningen. Het model kan worden gebruikt om de invloed van de tweedimensionale geometrie op de verblijftijdspreiding te analyseren, maar het model kan ook de reistijd van de instroomopening naar iedere plaats in het systeem berekenen. Op deze manier kan het model gebruikt worden om ruimtelijk verdeelde chemische reacties te analyseren.

Een belangrijk voordeel van de gebruikte methode is dat de parameters van de Uitgebreide Potentiaaltheorie een fysische betekenis hebben. De warmteflux van de twee wanden van een kanaal met obstakels is gemodelleerd met verbeterde Nusselt – Reynolds correlaties. Deze relaties zijn apart ontwikkeld voor de wand naast het hoofdstroomgebied en de wand naast een recirculatiegebied, omdat het stromingspatroon in het hoofdstroomgebied en in recirculatiegebieden niet hetzelfde is. De aangepaste Nusselt – Reynolds correlaties zijn vergeleken met de uitkomsten van de CFD modellen met warmtetransport erin. Op deze manier is een simpel model gevonden voor de warmteflux van een wand naast een wervel, dat een fout van slechts 7% heeft. Het is ook aangetoond dat de aangepaste Nusselt – Reynolds correlaties beter werken dan conventionele Nusselt – Reynolds correlaties. Hieruit blijkt de relevantie van de parameters van de Uitgebreide Potentiaaltheorie.

Uit het onderzoek in dit proefschrift kan worden geconcludeerd dat nieuwe simpele modellen voor ruimtelijk inhomogene milieukundige en agrotechnische systemen ontwikkeld kunnen worden door het stromingspatroon te modelleren als stroming door een recht kanaal, zelfs als de stroming in werkelijkheid ook recirculatiegebieden bevat. Simpele modellen kunnen gebruikt worden om een specifieke systeemgeometrie te onderzoeken, of ze leveren ruwe benaderingen op die onafhankelijk zijn van geometrische details. Simpele modellen zijn niet de aangewezen methode om de invloed van geometrische details te onderzoeken, omdat deze modellen parameters hebben die voor elke geometrie variatie apart gekalibreerd moeten worden. De invloed van geometrie details kan worden onderzocht met CFD modellering. Met behulp van een goed doordacht rooster kan een verrassend efficiënt CFD model worden verkregen, maar er is veel kennis nodig om een rooster te maken voor stromingen die worden veroorzaakt door natuurlijke convectie, waarvoor de oplossing ook daadwerkelijk convergeert. Verder is veel kennis nodig om zogenaamde valse diffusie in het algoritme tegen te gaan.

Uit dit proefschrift kan ook worden geconcludeerd dat Uitgebreide Potentiaaltheorie een snelle methode is om algemene stromingen met een hoofdstroom en

recirculatiegebieden door te rekenen. De methode benadert locale snelheidsvectoren met een gemiddelde fout van 20% - 30% voor een groot bereik van het Reynolds getal. Er zijn twee methodes ontwikkeld om de Uitgebreide Potentiaaltheorie te benutten. Te eerste kan Uitgebreide Potentiaaltheorie als een bouwsteen worden gebruikt om de verblijftijdspreiding te modelleren. Ten tweede hebben de parameters van een model gebaseerd op Uitgebreide Potentiaaltheorie een fysische betekenis, zodat Uitgebreide Potentiaaltheorie veel gemakkelijker kan worden gebruikt door de toegepaste ingenieur die belang hecht aan een fysische interpretatie van de model parameters. Dit in tegenstelling tot andere modelreductie methoden waarin de model parameters vaak niet kunnen worden geinterpreteerd in kenbare fysische begrippen.

Dankwoord

Allereerst wil ik graag mijn co-promotor, Wilko van Loon, bedanken. Wilko, je hebt me geleerd om resultaatgericht te werken door te focussen op de kern van mijn project. Verder heb je me geleerd om met stress om te gaan. Door je begeleiding is mijn promotie niet alleen technisch een succes geworden, maar ook in persoonlijk opzicht een leerervaring.

Graag bedank ik ook mijn co-promotor Hans Stigter voor zijn adviezen over systeemtheorie en modelreductie, en voor zijn commentaar op mijn teksten. Hans, ik vond onze gesprekken, die over allerlei onderwerpen gingen, erg waardevol en ik bedank je voor je oprechte belangstelling voor mijn wereldbeeld. Verder bedank ik mijn promotor Prof. Gerard Bot voor zijn overzicht over mijn project. Het is eigenlijk ook jouw project, omdat jij het onderzoeksvoorstel hebt geschreven dat mij de kans gaf dit project te doen.

Verder bedank ik mijn paranimf Bas Speetjens en Tom van der Walle, die gezorgd hebben voor de experimentele data die in hoofdstuk 2 worden gepresenteerd. Ik dank ook Jan Post en Joost Veerman, die de experimenten hebben verzorgd die essentieel waren voor hoofdstuk 4. Ook bedank ik Pieter van Norel en Rade Matic, die met eindeloos geduld waterdrukken hebben gemeten. David Lentink, zonder jou was hoofdstuk 5 geen succes geworden. Je hebt me behoorlijk laten schrikken met je scherpe kritiek op mijn Computational Fluid Dynamics berekeningen, maar je kritiek was terecht en van grote waarde.

Ook ben ik mijn collega's van Meet-, Regel- en Systeemtechniek, in het bijzonder Bas Speetjens en Marja Portengen, erg dankbaar voor de gezelligheid in onze groep en voor hun steun. Bas, bedankt voor je hulp bij het practicum Process Engineering EA. Marja, ik bedank je voor je hulp met mijn administratie.

Een goed proefschrift vraagt inhoudelijke kennis op een breder terrein dan het onderzoeksonderwerp. Daarom bedank ik Hady Hadiyanto, Mohammed Djaeni, Dirk Vries, Jouke Campen, Jan Swarts, Julita Manski, Edwin Habeych, Esther Bloem, Johan van Leeuwen en Ruud van Damme voor hun kennis over Computational Fluid Dynamics. Verder bedank ik Hans Swarts, Karel Keesman, Paul Torfs, Ton Hoitink en Hardy Temmink voor hun kennis over modelreductie, en Pepijn van Oort, Geerten Hengeveld en Tammo Bult voor hun kennis over data analyse. Ook de leden van de

leescommissie, Eldert van Henten, Bert Hamelers, Cees Buisman, Jaap Molenaar en mijnheer van der Meer ben ik dank verschuldigd voor het zitting nemen in de leescommissie.

Verder wil ik Petra Stolk bedanken voor het grondig doorlezen van twee hoofdstukken van mijn proefschrift. Je hebt er veel tijd aan besteed en had goed commentaar. Ook bedank ik mijn paranimf Coco van der Wolk en Rays Jiang voor hun interesse en steun. Ook bedank ik Mark Huibrechts voor het oplossen van een lastige computerstoring thuis, waardoor thuiswerken een stuk aangenamer werd.

Tenslotte bedank ik mijn ouders, Liesbeth en David Dirkse, voor hun praktische steun. Jullie hebben veel tijd besteed aan mijn verhuizing naar Wageningen, en jullie hebben mij gastvrijheid in het ouderlijk huis geboden waardoor ik mijn reistijd naar mijn nieuwe werkplek binnen de perken kon houden.

Curriculum Vitae

Martijn Halbo Dirkse werd te Zwolle, Overijssel geboren op 18 juni 1973. In de periode 1986 - 1992 deed hij VWO aan het Alkwin Kollege te Uithoorn, Noord Holland. Hij vervolgde zijn opleiding aan de Vrije Universiteit Amsterdam, waar hij wiskunde studeerde in de periode 1992 - 1997. Hij volgde een breed vakkenpakket waarin naast wiskunde ruimte was voor informatica en natuurkunde. Het zwaartepunt lag bij de wiskundige analyse en hij studeerde met lof af op een intern afstudeerproject.

Na zijn studie koos Martijn voor de ICT. Hij was in de periode 1997 - 2002 programmeur, achtereenvolgens bij Paralax te Maarssen, IBM te Amsterdam-Zuidoost en Wellance te Diemen. In 2003 begon hij bij Wageningen Universiteit aan het promotieonderzoek dat tot dit proefschrift heeft geleid. Hij vervolgt zijn loopbaan bij het bedrijf Ars Traffic & Transport Technology, dat werkt aan intelligente transportsystemen (ITS).

Naast zijn opleiding en werk maakt Martijn muziek, in zijn jeugd op de cello en tegenwoordig als zanger. Hij ontplooide ook maatschappelijke activiteiten, onder anderen in de faculteitsvereniging bij de VU, bij de Partij van de Arbeid en bij de bewonerscommissie van zijn flat in Wageningen.

SENSE Education

SENSE PhD courses:

- Environmental Research in Context

- Research Context Activity: "Research essay on: Spatial Model Reduction for Environmental Policy Makers"

- Physical Modelling

Other Phd and MSc courses:

- System and Control Theory of Nonlinear Systems

- Systems Theory self study

- Transport Phenomena self study

- Control Engineering & Process Control

- PhD Scientific Writing

- Project and Time Management

- Oral Presentation in English

- Organisation of discussion group on Computational Fluid Dynamics modelling

- PE & RC Discussion group Mathematics and Statistics

Oral Presentations:

- Environmental Change: Prevent or Adapt, Applying spatial model reduction to Blue Energy, 23 June 2006, VU Amsterdam, Amsterdam, The Netherlands

- Modelling of Natural-Convection Driven Heat Exchangers, Agricontrol 2007, 3 September 2007, Osijek, Croatia

- A Simple Model for Obstructed Two-Dimensional Turbulent Channel Flow, Eurotherm Seminar 82 – Numerical Heat Transfer 2005, 16 September 2005, Cracow, Poland